

1N-05
209759
93P

Experimental Investigation of Advanced Hub and Pylon Fairing Configurations to Reduce Helicopter Drag

D. M. Martin, R. W. Mort, L. A. Young, and P. K. Squires

SEPTEMBER 1993

NASA
National Aeronautics and
Space Administration

(NASA-TM-4540) EXPERIMENTAL
INVESTIGATION OF ADVANCED HUB AND
PYLON FAIRING CONFIGURATIONS TO
REDUCE HELICOPTER DRAG (NASA)
93 p

N94-2660

Unclas

H1/05 0209759



Experimental Investigation of Advanced Hub and Pylon Fairing Configurations to Reduce Helicopter Drag

D. M. Martin, *Sterling Software, Palo Alto, California*
R. W. Mort, *Bell Helicopter Textron, Inc., Fort Worth, Texas*
L. A. Young, *Ames Research Center, Moffett Field, California*
P. K. Squires, *Bell Helicopter Textron, Inc., Fort Worth, Texas*

SEPTEMBER 1993



National Aeronautics and
Space Administration

Ames Research Center
Moffett Field, California 94035-1000

10/10/2020

10/10/2020

Contents

	Page
Symbols	iv
Summary	1
Introduction.....	1
Test Objectives.....	1
Model Description and Wind Tunnel Setup	2
Instrumentation	2
Test Conditions	2
Tare and Interference Procedure.....	2
Accuracy	3
Description of Hub and Pylon Fairing Configurations	3
Pylon Fairings.....	3
Hub Fairings	4
Integrated Hub and Pylon Fairings	4
Dual Component Configurations.....	4
Test Matrix	5
Results.....	5
Drag Reducing Configurations	5
Unfaired Rotor Hub with Pylon Fairings	5
Hub Fairings with a Nontapered Pylon Fairing.....	6
Component Buildup of the 15%/Nontapered Configuration.	7
Additional Data.....	8
Comparison of 15% and 22% Hub Fairings with Nontapered, Tapered, and Inverse Tapered Pylon Fairings	8
Comparison of Single Pylon Fairing with 15% and 22% Hub Fairings, and as Dual Component #1 and #2 Configurations.	9
Component Buildup of Integrated Hub and Pylon Fairing Configurations	9
Dual Component Configurations.....	9
RPM and Reynolds Number Effects.....	10
RPM Effects	10
Reynolds Number Effects.....	10
Conclusions.....	10
References.....	11

Symbols

D	drag force in wind axes, lb
L	lift force in wind axes, lb
M	pitching moment in wind axes, ft-lb
N	yawing moment in wind axes, ft-lb
q	dynamic pressure, lb/ft ²
Re	Reynolds number ($\rho V_{\infty} / \mu$), ft ⁻¹
RM	rolling moment in wind axes, ft-lb
V_∞	tunnel speed, ft/sec
Y	side force in wind axes, lb
α	fuselage angle of attack, deg
μ	coefficient of viscosity, slugs/ft-sec
ψ	fuselage yaw angle, deg
ρ	density, slugs/ft ³

Abbreviations

DC	dual component
HF	hub fairing
PF	pylon fairing
RPM	revolutions per minute

Experimental Investigation of Advanced Hub and Pylon Fairing Configurations to Reduce Helicopter Drag

D. M. MARTIN,* R. W. MORT,** L. A. YOUNG, AND P. K. SQUIRES**

Ames Research Center

Summary

New hub and pylon fairing designs were tested on a one-fifth scale Bell Helicopter Textron Model 222 helicopter with a bearingless main rotor hub. The blades were not installed for this test. The fairings were designed by NASA and Bell Helicopter Textron under a joint program and tested in the Ames Research Center 7- by 10-Foot Wind Tunnel. All six aircraft forces and moments were measured using the tunnel scales system. Previous research has identified the integrated hub and pylon fairing approach as the most efficient in reducing helicopter drag. Three hub fairings and three pylon fairings were tested (in various combinations) resulting in a total of 16 different configurations, including the baseline helicopter model without fairings. The geometry of the new fairings is described in detail. Test results are presented in the form of plots of the six model forces and moments. The data show that model drag can be reduced by as much as 20% by combining a small hub fairing (that has a circular arc upper surface and a flat lower surface) integrated with a nontapered pylon fairing. To minimize drag, the gap between the lower surface of the hub and upper surface of the pylon fairing must be kept to a minimum. Results show that the aerodynamic effects of the fairings on static longitudinal and directional stability can also be important.

Introduction

The reduction of helicopter parasite drag associated with hub and rotating hardware components has long been a goal of NASA and the helicopter industry. Comprehensive reviews of this problem have shown that the drag of the rotor head, mast, and control system account for 20 to 30% of total helicopter parasite drag (refs. 1-3). A reduction in parasite drag would result in one or more of the following performance improvements: lower required power, higher speed, and increased range.

Since 1985, NASA has been investigating various drag reduction methods aimed primarily at fairing the rotor

head, mast, and control system hardware. A series of experimental studies has been conducted (refs. 4-8), which investigated a number of hub and pylon fairing shapes. In reference 8, the authors supported the observations made by previous researchers that the design of hub and pylon fairings should be integrated, and that hub fairings with circular arc upper surfaces and flat lower surfaces produced the greatest reduction in model drag.

During previous phases of the NASA hub drag reduction program, only nonrotating hub data had been acquired. It was assumed that rotation of the hub would not affect the relative drag trends between the various configurations. Also, the results of references 4-8 were obtained for hubs without blades or blade shanks. The fairing configurations tested previously were not compared to a baseline helicopter model having an unfaired hub, mast, and controls. Furthermore, the influence of hub and pylon fairings on helicopter static stability had not been adequately explored. The test discussed in this report addresses all of these issues. The initial phase of the joint program consisted of the design of improved hub and pylon fairings by NASA and Bell Helicopter Textron. These were then tested on a scale model of the Bell 222 helicopter with an advanced, low-drag rotating hub and blade cuffs.

Test Objectives

The objectives of the test program were as follows:

1. Measure the total drag reduction associated with the NASA/Bell hub and pylon fairings and compare the results with the drag levels of an unfaired Bell M-222 model with a bearingless hub.
2. Identify the configuration which yields the largest reduction in drag compared to the unfaired rotor and mast.
3. Demonstrate the advantages of the integrated hub/pylon fairing concept in reducing drag.
4. Study the aerodynamic effects of the new fairings on helicopter longitudinal and lateral forces and moments.

*Sterling Software, Palo Alto, California.

**Bell Helicopter Textron, Inc., Fort Worth, Texas.

5. Use the component build-up method to study the individual drag contributions of the hub and pylon fairings.
6. Determine whether drag reductions are affected by hub RPM.

Model Description and Wind Tunnel Setup

In the following discussion, reference will be made to the aerodynamic characteristics of the baseline model, shown in figure 1. This is the model helicopter configuration, with unfaired hub and rotor shaft and bearingless main rotor, to which all subsequent fairing designs are compared. The baseline configuration consists of a one-fifth scale Bell Model 222 fuselage with 680 bearingless rotor hub (without blades but with blade shanks). A horizontal tail with negative camber and vertical tail cambered on the starboard side were installed on the model for all data runs. The mast, yoke, blade cuffs, control rods, and swashplate were also scaled to one-fifth of the full-scale aircraft. The advanced technology hub/yoke assembly was designed to accommodate four blades. The Model 222 airframe depicted in figure 1 was previously used in unrelated research for demonstration of the 680 rotor.

Figure 2 is a side view of the wind-tunnel model on its support strut. The strut was attached directly to the tunnel floating frame to allow measurement of lift, drag, and pitching moment as well as side force, yawing moment, and rolling moment. The angle of attack about the pitch axis was adjusted through actuation of an electric motor/screw gear assembly located at the top of the strut (inside the model, not visible in fig. 2). Positive angles of attack were set by pitching the model in the nose-up direction. Yaw angles were set by rotating the tunnel turntable, with the positive orientation defined as the nose-right direction. A strut fairing was mounted onto a steel plate that bridged across the turntable. As the turntable rotated, the strut fairing remained aligned with the free stream direction, regardless of the model yaw angle. This reduced the flow disturbance below the fuselage and its impact on the measured loads. The moment reference center (along the rotor hub centerline) was selected to match the location used in previous tests (ref. 9). Figure 2 also shows the orientation of positive directions for measured forces and moments.

Instrumentation

In addition to the tunnel scale system, which was used as the primary load-measuring device, a number of safety instrumentation transducers were installed on the model. Lateral accelerations were monitored by an accelerometer

mounted inside the model. This transducer was also used to acquire data for hub balancing. Longitudinal accelerations were monitored by a second accelerometer located on the fuselage centerline. The hub rpm was measured by a phototach. Health monitoring of the electric motor which powered the shaft was accomplished through a display of stator temperature as measured by a thermocouple. Motor cooling water temperatures were also monitored at various stations.

Test Conditions

The tunnel flow conditions and model parameter ranges for the test are listed in table 1.

The majority of the test data were acquired on the new hub fairing configurations at a tunnel dynamic pressure of 80 psf ($Re = 1.65 \times 10^6 \text{ ft}^{-1}$). A limited number of runs were performed at 40 and 60 psf ($Re = 1.17 \times 10^6 \text{ ft}^{-1}$ and $Re = 1.43 \times 10^6 \text{ ft}^{-1}$) to study the effects of Reynolds number. For most runs, hub rotation was set at 1500 rpm.

Table 1. Test conditions and $\alpha - \psi$ limits

Dynamic pressure	40, 60, 80 psf
Tunnel velocity	108.6, 133.0, 153.6 knots
Reynolds number	$1.17 \times 10^6 \text{ ft}^{-1}$ $1.43 \times 10^6 \text{ ft}^{-1}$ $1.65 \times 10^6 \text{ ft}^{-1}$
Hub rotation speed	400, 800, 1200, 1500 rpm
α and ψ sweeps	
	$\psi = 0.0^\circ, -10.0^\circ \leq \alpha \leq 16.0^\circ$
	$\psi = 5.0^\circ, -10.0^\circ \leq \alpha \leq 16.0^\circ$
	$\alpha = 0.0^\circ, -10.0^\circ \leq \psi \leq 10.0^\circ$

This RPM would produce the correct full-scale hover tip speed if the one-fifth-scale blades had been installed. Some data were also acquired at lower hub rotation speeds to determine the effects of RPM on model forces and moments.

Tare and Interference Procedure

Although the major test objectives called for comparison of the baseline unfaired model results with the faired configurations, aerodynamic tares were measured nonetheless and subtracted to obtain model-alone data.

The aerodynamic tare data were acquired in three phases. First, the model was mounted in an inverted position as shown in figure 3. The image fairing and strut system suspended above the model were designed and installed to duplicate exactly the hardware and critical dimensions of the model support strut in the upright position. In this inverted configuration, the model itself was supported by the lower strut and tunnel floating frame. The non-metric upper image fairing was supported by the wind tunnel structure. The image strut, which appears to extend from the image fairing, was actually mounted on the model on the metric side. This ensured that the interference of the image fairing on the strut, as well as the interference of the fairing and strut on the model, were included in the loads measured in the first phase of the tare and interference procedure. Data were acquired for all test conditions described in table 1 for this configuration. Third order curve-fit coefficients were obtained for each of the six components of model loads.

In the second phase, the image fairing was removed, as was the metric image strut attached to the fuselage. This configuration is shown in figure 4. Data were acquired again for the ranges specified in table 1 and were curve fitted as well. The tare correction was then calculated by subtracting the data acquired without the image system from the data with the image system in place (the higher drag configuration):

$$D_{\text{tare}} = D_{\text{im sys}} - D_{\text{w/o im sys}} \quad (1)$$

For the drag loads, a net streamwise residual force thus remained that was equivalent to the interference drag of the fairing and strut on the model plus the interference drag of the fairing on the support strut. These results were then curve fitted and permanently stored into the data system. For the remainder of the test, the tare and interference contributions for a given dynamic pressure (and Reynolds number), angle of attack, and yaw angle were thus automatically subtracted from the measured loads. For example, the corrected drag force would be given by:

$$D_{\text{corr}} = D_{\text{meas}} - D_{\text{tare}} \quad (2)$$

The same procedure was used to correct the five other forces and moments presented in this report. No other corrections were applied to the data.

Accuracy

The accuracies for the measured forces and moments are listed in table 2. These are based on the design accuracy of the tunnel scales. Note that a realistic estimate of accuracy on rolling moment was not possible. This was

found to be caused by hysteresis effects in the weight tares at negative ψ angles. This problem affected the entire weight tare curve fit. All rolling moment data presented in this report are thus in error by an undetermined factor.

Table 2. Measured accuracy for model forces and moments

Force or moment	Maximum error	% Full scale
Lift	±0.6 lb	±0.01
Side force	±1.0 lb	±0.03
Drag	±0.4 lb	±0.03
Pitching moment	±3.5 ft-lb	±0.19
Yawing moment	±6.0 ft-lb	±0.24
Rolling moment	—	—
Dynamic pressure	±0.7 psf	±0.49

Description of Hub and Pylon Fairing Configurations

This test was the third in a series of experiments to study the characteristics of hub and pylon fairing configurations. An extensive body of data had been acquired on various early designs which led to many new and interesting fairing concepts. Short descriptions of each fairing (along with some comments on design philosophy) are included in the paragraphs that follow.

Pylon Fairings

Experience from previous tests (refs. 1-8) and general trends in the helicopter industry have shown that substantial reductions in vehicle drag can occur if the mast, control rods, and associated hardware above the fuselage cowling are faired.

The first of three fairings designed for this test consisted of a nontapered pylon fairing with a constant chord of 1.70 ft (20.4 in.) as shown in figure 5. NACA 0034 airfoil profiles were used to define the cross section. This fairing is relatively thick, and allows for larger diameter swashplates and bulky rotating hardware in the vicinity of the rotor shaft. It is shown installed on the model in figure 6.

The second pylon fairing concept was tapered from bottom to top and defined by NACA 63-series airfoils. A sketch is shown in figure 7. The upper third of the fairing was defined by 63-021 sections; 63-024 sections were used for the middle third of the fairing; the bottom third

contours were based on thicker 63-028 airfoil sections. The chord length at the cowling-fairing junction was 2.68 ft (32.2 in.) and the taper ratio was 0.78. As shown in figure 8, this fairing is very long and extends farther forward than the NACA 0034 and as far aft as the engine exhaust nozzles.

The inverse tapered pylon fairing depicted in figure 9 was designed to reduce the net wetted area of the fairing (as compared to the straight fairing) while still streamlining the mast, swashplate, and control rods. The fairing contours were also defined by NACA 0034 airfoil sections. At the base, the fairing chord was 1.4 ft (16.8 in.) while at the top it was 1.70 ft (20.4 in.). The taper ratio was 1.21. The inverse tapered pylon fairing is shown mounted on the model in figure 10. The pylon fairings will be referred to hereafter as the nontapered, tapered, and inverse tapered configurations.

Hub Fairings

The main emphasis in the design of the hub fairings lies in the reduction of parasite drag associated with the rotating hub. As shown in references 5–8, the cambered-elliptical or cambered-circular arc shape with flat lower surface has proven to be effective in reducing the drag of nonrotating hubs without blades. A flat lower surface also allows for reduction of the gap between hub and pylon fairings, thus eliminating any flow between the two. Among other design features, the hub fairings designed for this test have cutouts which are sized with sufficient clearance to allow for blade flapping and lead-lag motion. Finally, the leading edges of the hub fairings were rounded, as opposed to the sharp edges of past circular-arc designs. This modification was incorporated to model a proposed full-scale implementation approach as discussed in reference 10.

Figure 11 shows a sketch of the smallest diameter hub fairing for which data were acquired. This configuration consists of a circular-arc hub fairing with flat lower surface as described in the previous paragraph. Its radius is equivalent to 15% of the rotor radius with the blades installed. The fairing diameter is 1.15 ft (13.8 in.) and its maximum thickness is 0.23 ft (2.80 in.), which results in a thickness to diameter ratio of 20%. Note that with this small fairing, large portions of the blade cuffs are exposed to the flow, and the potential for interference drag effects between the cutouts and the blade cuffs is relatively high. The 15% fairing is shown installed on the model in figure 12. Small cutouts on the hub fairing baseplate were made to allow the control rods to extend from the swashplate to the blade roots.

Figure 13 depicts the second hub fairing tested, which is identical in shape to the 15% design but with a radius equivalent to 22% of the rotor radius. This results in a greater portion of the fairing enclosing the blade cuffs, but it increases the wetted area as well as the cross-sectional area of the fairing. The maximum thickness of the 22% hub fairing is the same as for the smaller one (0.23 ft). The fairing diameter is 1.67 ft (20.04 in.). The thickness-to-diameter ratio of this fairing is 14%. Figure 14 shows the 22% radius hub fairing installed on the model. The small and large hub fairings will be referred to subsequently as the 15% and 22% fairings.

Integrated Hub and Pylon Fairings

The primary design objective of integrating the hub and pylon fairings is to reduce the gap between the two bodies. In other words, the rotating flat lower surface of the hub fairing must fit as close as possible to the flat top surface of the pylon fairing. As shown in reference 7, for nonrotating hubs, minimizing this gap was shown to reduce parasite drag considerably.

For most of the integrated hub and pylon fairing configurations designed for this test, friction between the rotating and nonrotating parts (as well as vibration) was minimized by bonding a layer of felt to the top of the pylon fairing. Close-up views are shown in figure 15. The felt material approach is impractical to apply to a flight vehicle. Conceptual designs of hub and pylon fairings that allow for hub motion (while still minimizing the gap) have been produced by helicopter manufacturers and NASA (ref. 10). Simplified versions of these designs were studied during this test. These concepts will be discussed in the next section.

Figure 16 shows two views of the Model 222 fuselage with the nontapered pylon fairing and 15% hub fairing. Notice that the gap between the fairings is so small that it is not discernible. Figures 17 and 18 show the 15% hub fairing with the tapered and inverse tapered pylon fairings, respectively.

Figures 19–21 depict the 22% rotor radius hub fairing matched with the nontapered, tapered, and inverse tapered pylon fairings respectively. One of the major differences between this set of configurations and the previous group is the obvious overhang of the hub fairing beyond the leading edge of the pylon fairings.

Dual Component Configurations

The dual component fairings are entirely new concepts not previously evaluated in the wind tunnel. They consist of a rotating hub fairing and a pylon fairing with a

nonrotating circular plate attached to its top portion. This design approach was taken to examine more practical alternatives to the minimum gap requirement between rotating and nonrotating components. Also, these fairing combinations are believed to be more realistic in addressing the hub motion problem discussed in the preceding section. Figure 22 shows a sketch of the rotating portion of the Dual Component #1 concept. This is a large hub fairing, with a radius equivalent to 24% of the installed rotor radius. The outer edge of the hub fairing is machined so that it forms a shoulder that rotates inside a circular channel within the nonrotating baseplate (as seen in figure 23 assembled with the nontapered pylon fairing). This decreases the flow of air between the hub fairing and the circular plate. The diameter of the fairing (including the fixed base plate) is 1.83 ft (22.0 in.). Its equivalent thickness to chord ratio is 19%.

Figure 24 shows the Dual Component #1/nontapered configuration mounted on the model. A 1-inch portion of the pylon fairing was removed to allow installation of the circular nonrotating component. On a production helicopter, the groove in the nonrotating component would be wide and deep enough to allow for motion of the hub fairing edge caused by longitudinal and lateral hub motion. As will be discussed later, data were also acquired in this configuration with the tapered pylon fairing.

The Dual Component #2 configuration is shown in a close-up view of the model in figure 25 with the inverse tapered pylon fairing. This design incorporates the original 15% hub fairing. The circular nonrotating baseplate mounted on top of the pylon fairing is thin and simulates an inflatable seal. On a production helicopter, this seal would change shape as a result of motion of the hub fairing while it closed the gap between the hub and pylon fairings. Data were also acquired for this configuration with the nontapered pylon fairing.

Test Matrix

A total of sixteen configurations, including the unfaired baseline rotor and shaft, were tested. These include pylon fairings with unfaired hubs, faired hubs without pylon fairings, as well as integrated fairings and dual component configurations. Table 3 shows those configurations, for each of which two α sweeps ($\psi = 0^\circ$ and $\psi = 5^\circ$) and one ψ sweep ($\alpha = 0^\circ$) were performed at a tunnel dynamic pressure of 80 psf.

Results

The results will be presented in two parts. First, test data for the configurations with best drag-reducing capabilities will be presented and discussed. Although the main focus of this research program deals with drag reduction, the influence of the hub and pylon fairings on all model forces and moments and on static stability is important. These data will also be presented along with the drag data. Results for the remaining configurations will be presented in a second section to provide a comprehensive look at the overall scope of the test data set. Finally, the last section will deal with the effects of hub RPM and Reynolds number on the results. All data discussed in this report have been scaled to full-scale loads.

Drag Reducing Configurations

Unfaired Rotor Hub with Pylon Fairings

Figure 26(a) shows the variation of D/q vs α at $\psi = 0^\circ$ for the unfaired hub and rotor mast as compared to the unfaired hub with the addition of the nontapered, tapered, and inverse tapered pylon fairings. Clearly, the addition of a streamlined fairing substantially reduces the parasite drag of the rotating mast, swashplate, and control rods above -4° of fuselage angle of attack. The minimum drag

Table 3. Hub and pylon fairing configurations tested

Hub fairing	Pylon fairing			
	None	NACA 0034 nontapered	Inverse tapered	NACA 63 Series tapered
None	X	X	X	X
15% rotor radius	X	X	X	X
22% rotor radius	X	X	X	X
Dual component (#1)	—	X	—	X
Dual component (#2)	—	X	X	—

point for all configurations occurs somewhere around $\alpha = 3^\circ$, rather than at the minimum fuselage angle of attack. This is due in part to the drag contribution of the hub, which is fixed at an angle of -5° relative to the fuselage. For $\alpha = 3^\circ$, the hub chord is almost aligned with the flow, and its drag is at a minimum.

The data suggest that there is very little difference between the tapered pylon fairing and the nontapered fairing for $-10^\circ \leq \alpha \leq 4^\circ$. The small differences in D/q can probably be attributed to the effect of wetted area on skin friction drag. The curves show that despite having less wetted area, the inverse tapered pylon fairing produces more drag. This is not clearly understood, but it may be related to interference effects between the top of the fuselage and the bottom of the fairing. Figure 26(b) shows a comparison of the same configurations, but at $\psi = 5^\circ$. The same trends are observed here with the nontapered pylon fairing yielding the most drag reduction but by a slightly wider margin, especially in the negative α range.

The minimum drag measured for both $\psi = 0^\circ$ and $\psi = 5^\circ$ is compared as a function of pylon fairing configuration in figure 26(c). As one might expect, the minimum total model drag is larger for the non-zero yaw angle. From these data, the calculated reduction in D/q achieved through installation of the nontapered pylon fairing (as compared to the unfaired baseline configuration) is 14.5% for $\psi = 0^\circ$ and 11.2% for $\psi = 5^\circ$.

Figures 27 and 28 show the effects of the pylon fairings on the lift and pitching moment variations with α . The lift is unaffected (fig. 27(a)) while substantial differences in pitching moment are observed. Note that without a rotor, the model pitching moment is positive through the range of α used for the test. With the pylon fairings installed, the slope of the pitching moment curve becomes more negative for $\alpha \leq 6^\circ$. The flowfield downstream of the pylon fairing is more uniform. Apparently, this leads to an increase in tail effectiveness, which causes the change in pitching moment slope. The trends for the $\psi = 5^\circ$ case are similar in nature (fig. 28(a) and 28(b)), with the nontapered pylon fairing yielding the highest increase in tail effectiveness. Since the slope of the pitching moment curve increases negatively because of the pylon fairing, the static longitudinal stability of the model is increased for a large portion of the fuselage angle of attack range.

Figure 29 illustrates the results of a yaw angle sweep for side force, yawing moment, and rolling moment all normalized by dynamic pressure. As observed from the data of figure 29(a), the presence of the pylon fairings causes an increase in the side force component of the model which grows linearly with the magnitude of the yaw angle. The non-zero offset in Y/q at zero yaw is

caused by the cambered vertical tail. Figure 29(b) shows that the baseline model is statically stable directionally because the N/q curve has a negative slope. However, the addition of pylon fairings destabilizes the model, in particular with the tapered configuration. This is believed to be caused by the combination of two effects. First, since the aerodynamic centers of the pylon fairings lie in the vicinity of the quarter-chord, they are located slightly ahead of the model moment reference center. As the loading (acting at the aerodynamic center) on the pylon fairing increases, the model is destabilized. Second, the vortex shed off the top of the pylon fairing induces sidewash which alters the loading on the vertical tail, contributing to the unstable behavior.

The data of figure 29(b) show that the instability problem is not as severe for the inverse tapered pylon fairing. This is the only pylon fairing that gives at best some degree of neutral directional stability (zero slope of the N/q curve) in the range $-4^\circ \leq \psi \leq 4^\circ$. A more detailed explanation of these effects is provided in reference 10.

As for rolling moment, it is not clearly understood why the addition of pylon fairings reduces RM/q over the entire range of ψ . Because the aerodynamic center of the pylon fairing is above the model roll axis, a positive increase in RM/q for $\psi > 0^\circ$ (nose right) and a negative increase for $\psi < 0^\circ$ would be expected. However, as mentioned previously, no conclusive interpretation of the rolling moment results is possible because of the weight tare problem.

Hub Fairings with a Nontapered Pylon Fairing

The aerodynamic effects of the hub fairings in combination with a pylon fairing will now be discussed. The results of reference 6 showed that maximum drag reduction was obtained when the gap between the lower surface of the hub fairing and the upper portion of the pylon fairing was minimized. In the present study, this design goal was achieved by allowing the lower surface of the hub fairing to come as close as possible to the top of the pylon fairing, as discussed previously.

Because the nontapered pylon fairing showed the best drag reduction characteristics (although by a small margin), it is used here as the baseline pylon fairing to compare hub fairing effects in integrated configurations. Figures 30(a) and 30(b) show the variation of D/q vs α for the four hub fairings matched with the nontapered pylon fairing at $\psi = 0^\circ$ and $\psi = 5^\circ$. The data show that the smallest hub fairing (15% of rotor radius) yields the largest reduction in drag, particularly for $\alpha < 2^\circ$.

From the curves for the large Dual Component #1 and 22% rotor radius hub fairings, it can be concluded that

large hub fairings are not appropriate for drag reduction. It was originally thought that because they cover a greater portion of the blade cuffs, larger hub fairings might reduce the form drag of the rotating hubs to a greater extent. However, note that for $\alpha > 4^\circ$, the variation of D/q for the 15% and 22% are almost identical. This may be related to a drop in form drag of the 22% hub fairing because the large blade cutouts are not directly exposed to the flow at positive shaft angles of attack (for $\alpha \approx 5^\circ$, the shaft incidence angle relative to the free stream is $\approx 0^\circ$).

As mentioned above, the Dual Component #1 hub fairing (with the slotted baseplate) actually increased the drag considerably as compared to the unfaired hub. This is most probably caused by pressure drag effects related to this unique configuration. Since the Dual Component #1 and 22% radius hub fairing diameters were approximately the same, the results clearly show that the Dual Component #1 is not a viable option. For example, if the Dual Component #1 were reduced to the same radius as the 15% hub fairing, there would still be a drag penalty for the smaller Dual Component #1 compared to the 15% fairing. This conclusion can be reached by analogy to the comparison of the Dual Component #1 and the 22% fairing shown in figures 30(a) and 30(b).

It is also surprising that the simple addition of a fixed baseplate as in the Dual Component #2 concept results in a relatively large drag increase from the basic 15% hub fairing with the nontapered pylon fairing. The reason for this substantial difference is not clearly understood. Nonetheless, the D/q curves for the Dual Component #2 seem to come closer to those of the 15% hub fairing for $\alpha < -2^\circ$ than to those of other configurations.

Figure 30(c) illustrates more clearly the degree of drag reduction achieved for each hub fairing under study. As in figure 26(c), this plot compares the minimum measured D/q for each configuration. For these full-scale data, the 15% hub fairing yields an additional reduction of 7.3% over the nontapered pylon fairing with unfaired hub configuration at $\psi = 0^\circ$. For $\psi = 5^\circ$, the drag is reduced an additional 3.6% by adding the hub fairing. Note also that as far as minimum drag is concerned, the 22% rotor radius hub fairing gives better results than the Dual Component #2, which uses the smaller, 15% hub fairing.

Figures 31 and 32 show the variation of L/q and M/q with α for the same configurations. As expected, the larger diameter hub fairings (22% and Dual Component #1) increase the lift curve slope (fig. 31) because the lifting area increases. Note the decrease in pitching moment for the Dual Component #1 in the negative α range. This is caused by the interaction of several factors. First, the hub fairing aerodynamic center is slightly forward of the model moment reference center; therefore, negative lift

reduces the positive pitching moment. Second, and perhaps most important, the separated wake shed from the large dual component hub fairing reduces the model tail effectiveness. Also, an opposite effect (nose-up moment) is produced by the drag increase of the hub fairing. In figures 31(b) and 32(b), it is also seen that since the 15% hub fairing and the Dual Component #2 are similar configurations, their pitching moment curves follow the same trends. The offset between the two can be attributed to a reduction in tail effectiveness associated with the Dual Component #2 fairing.

To conclude this section on hub fairing effects, the lateral-directional forces and moments are shown in figure 33. All three plots are consistent with the conclusions reached previously (fig. 29) regarding yaw angle effects. The addition of a hub fairing, regardless of its size and shape, seems to make little difference because the curves of Y/q (fig. 33(a)) and N/q (fig. 33(b)) for the different hub fairings tested are grouped together. The changes between the baseline unfaired hub and the hub/pylon fairing combinations for Y/q , N/q are, therefore, primarily the result of pylon fairing effects.

Component Buildup of the 15%/Nontapered Configuration

It was shown in the preceding section that the combination of a hub and pylon fairing with minimum gap is necessary to achieve minimum model drag. A closer look at the relative contributions of the 15% hub fairing and the nontapered pylon fairing provides a better understanding of the drag reduction process associated with the integrated hub and pylon fairing configuration. Figures 34(a) and (b) illustrate the variations of D/q with α for $\psi = 0^\circ$ and $\psi = 5^\circ$. Figure 34(c) shows the individual contributions at their respective minimum drag point.

The first conclusion drawn from the data of figures 34(a) and 34(b) is that, by itself, the addition of a hub fairing does not reduce model drag. It actually increases D/q over the entire range of α . This clearly indicates that for the large diameter hub fairings tested, the concept of fairing the rotor head and blade shanks alone is a practice to be avoided. As depicted in figure 34(c), the pylon fairing with the unfaired hub achieves an average (for $\psi = 0^\circ$ and 5°) reduction in drag of 12.9% as measured for the minimum drag point. The reduction in drag generated by fairing the rotating mast and control rods far outweighs the added interference between the rotating hub/blade cuffs and the top of the pylon fairing.

When the small 15% hub fairing is added to cover the rotor head and blade cuffs, thus closing the gap between the two bodies, model drag is at its lowest over the entire

range of fuselage angle of attack (see figs. 34(a) and 34(b)). As illustrated in figure 34(c), the integrated hub and pylon fairing configuration yields a 20.8% reduction in total model drag over the unfaired baseline configuration at $\psi = 0^\circ$. Since the hub fairing alone increases drag slightly, the fact that further reduction is observed when the two fairings are assembled together clearly shows that there is a substantial interference effect between the rotating hub and the top of the pylon fairing. Adding a hub fairing which closes the gap between the two bodies clearly reduces this interference drag production. The fundamental observation to be made from the data of figure 34(b) at $\psi = 5^\circ$ is that a small amount of sideslip or yaw angle will not change the important gains in drag reduction from the integrated hub and pylon fairing combination. The trends resulting from individual contributions of the components are also unaffected by yaw angle.

Figures 35 and 36 illustrate the variation of L/q and M/q with α for the component buildup sequence. The L/q curves show a slight increase in lift due to the hub fairing (fig. 35(a)). In figures 35(b) and 36(b), the almost constant offset in M/q between the unfaired and hub-fairing-alone cases is most probably due to drag. The pitching moment increases positively due to the location of the hub fairing above the moment center. Figures 35(b) and 36(b) also show that with a hub fairing added to the pylon fairing, the tail effectiveness discussed previously is increased slightly compared to the pylon-fairing-alone case.

Figure 37 shows the lateral-directional data acquired for the component buildup sequence. As expected, the hub fairing alone does not generate much side force (fig. 37(a)) or yawing moment (fig. 37(b)). However, the pylon fairing side force increases with the addition of a hub fairing. This is due to the endplate effect caused by the hub fairing on top of the pylon fairing. The data plotted in figure 37(b) show that the endplate effect causes further degradation of the directional stability of this model, particularly for $\psi < 0^\circ$. These data seem to lend more weight to the theory that the directional instability is caused by a forward offset in the pylon fairing aerodynamic center and that the sidewash at the vertical tail could be a secondary effect.

Additional Data

In the preceding section, the configurations which resulted in the largest drag reduction were presented. As shown in table 3, many combinations of hub and pylon fairings were tested during the course of this experimental program. The following section will present the remainder of the acquired data and discuss noteworthy points

which might not have been brought to light in the preceding discussion. In particular, the discussion to follow will also reinforce some of the observations made earlier.

The configurations are discussed as a function of similarity and design characteristics, not relative to measured performance. Both longitudinal and lateral-directional aerodynamic data are presented. For all cases, three series of plots are shown. The first two are of longitudinal data (α sweeps) at $\psi = 0^\circ$ and $\psi = 5^\circ$, and the last set presents the lateral-directional data (ψ sweeps) at $\alpha = 0^\circ$.

Comparison of 15% and 22% Hub Fairings with Nontapered, Tapered, and Inverse Tapered Pylon Fairings

In this section, the data acquired for the 15% and 22% hub fairings will be presented.

Figures 38–40 show the test data for the 15% hub fairing with the three pylon fairings. The lowest drag configuration (hub fairing with the untapered pylon fairing) clearly stands out in the D/q plots at $\psi = 0^\circ$ and 5° (figs. 38(a) and 39(a)). In figures 38(c) and 39(c), the low drag combination is seen to increase the tail effectiveness by the largest amount. The ψ sweeps of figure 40 show the same basic trends as observed before: the tapered pylon fairing produces the largest departures from directionally stable behavior.

The data for the 22% hub fairing in combination with the three pylon fairings are shown in figures 41–43. For $\psi = 0^\circ$ and $\psi = 5^\circ$, the nontapered pylon fairing still produces less drag with the 22% hub fairing (figs. 41(a) and 42(a)) for the positive α range. However, for $\alpha \leq -4^\circ$, the total faired drag is above the unfaired hub drag. This could be caused by an increase in interference drag in the blade shank/cutout area as the upper surface of the hub fairing is exposed to the free stream.

As discussed previously, an increase in L/q slope is observed because of the larger sized hub fairing (figs. 41(b) and 42(b)). The main point to note from the M/q plots of figures 41(c) and 42(c) is that the magnitude of the pitching moment in the negative α range is not as large as with the 15% hub fairing (figs. 38(c)–39(c)). Again, this is attributed to the large separated wake of the 22% hub fairing. The offset in M/q between the hub fairing with untapered pylon fairing and the two others is highlighted in figure 41(c). This can also be observed in figure 38(c), and it is consistent with previous conclusions that the untapered pylon fairing yields the largest increase in tail effectiveness (see fig. 27(b)).

The lateral-directional data for this combination (fig. 43) are very consistent with the results shown previously for

the 15% hub fairing. The deviations in Y/q and N/q are the least with the inverse tapered pylon fairing and more severe with the tapered fairing. Note that a comparison of N/q curves between the 15% hub fairing with tapered pylon fairing (fig. 40(b)) and the 22% hub fairing with the same pylon fairing (fig. 43(b)) reveals that the larger hub fairings yield greater magnitudes in maximum and minimum N/q .

Comparison of Single Pylon Fairing with 15% and 22% Hub Fairings, and as Dual Component #1 and #2 Configurations

In the first part of this report, a comparison of all data available from hub fairings with a single pylon fairing led to the conclusion that the 15% hub fairing, along with the nontapered pylon fairing, produced the greatest drag reduction. This approach is repeated here for the inverse tapered and tapered pylon fairings to determine whether further conclusions about alternative configurations can be made.

Figures 44–46 show the data acquired for the inverse tapered pylon fairing with hub fairings installed. No data were acquired for this pylon fairing with the Dual Component #1 hub fairing. Note that there is very little difference in D/q between the various combinations (figs. 44(a) and 45(a)) except for a steep drag rise caused by the 22% hub fairing for $\alpha < 2^\circ$.

The conclusions regarding the effect of the large hub fairing on the tail effectiveness are once again supported by the M/q curves (figs. 44(c) and 45(c)). The rolling moment data of figure 46(c) show the same trends described before that were caused by the suspected weight tare problem.

Figures 47–49 show the plots of data acquired for the tapered pylon fairing with the various hub fairings. In this case, no data were taken for the Dual Component #2 configuration. The wakes associated with the 22% hub fairing, and especially the Dual Component #1 fairing, reduce the download on the tail greatly as compared to the 15% hub fairing (fig. 47(c)). As in the previous case, the lateral-directional data (fig. 49) show no appreciable sensitivity to the particular hub fairing used.

Component Buildup of Integrated Hub and Pylon Fairing Configurations

Data illustrating the various aerodynamic effects of adding individual components to the basic helicopter model follow. The buildup of the 15% and 22% hub fairings with all three pylon fairings will be shown separately.

Figures 50–52 show the differences in the forces and moments between the unfaired case, the pylon fairing only, hub fairing only, and integrated fairing for the 22%/nontapered configuration. The drag rise associated with the 22% hub fairing is so large, that for $\alpha < 0^\circ$ ($\psi = 0^\circ$, fig. 50(a)) and $\alpha < 4^\circ$ ($\psi = 5^\circ$, fig. 51(a)) the integrated fairing produces more drag than does the pylon fairing alone, thus defeating the purpose of the hub fairing.

The component buildup data for the 15%/inverse tapered pylon configuration are shown in figures 53–55. The D/q data at $\psi = 0^\circ$ and $\psi = 5^\circ$ (figs. 53(a) and 54(a)) show that no appreciable gain is obtained by adding the hub fairing to the pylon fairing. This is not clearly understood in light of the additional reduction observed when the 15% hub fairing was added to the nontapered pylon fairing (figs. 34(a)–(b)).

Force and moment data for the 22%/inverse tapered component buildup are shown in figures 56–58. Again, for $\alpha < 4^\circ$ (figs. 56(a) and 57(a)), the pylon-fairing-alone configuration produces less drag than with the combination of both fairings.

The 15%/tapered fairing component buildup data are shown in figures 59–61. As for the 15%/inverse tapered case, no further drag reduction is measured by adding the hub fairing (figs. 59(a) and 60(a)). As observed for the preceding configuration, integrated fairing drag can be seen to increase above that of the pylon-fairing-alone configuration for $\alpha > 4^\circ$.

Figures 62–64 present the data obtained from the 22%/tapered component buildup. At $\psi = 5^\circ$ (fig. 63(a)), the integrated hub/pylon fairing shows a noticeable increase in D/q over the entire range of α tested. Also, figures 62(c) and 63(c) show that only the pylon-fairing-alone configuration increases the tail effectiveness in the negative α range. The tail effectiveness is also increased by the hub-fairing-alone configuration for $\alpha > 0^\circ$, but this is longitudinally destabilizing. The lateral-directional data (fig. 64) only seem to confirm the large effects of the tapered pylon fairing on Y/q and N/q and the endplate effect caused by the hub fairing.

Dual Component Configurations

Figures 65–67 show comparisons of the data acquired for the four dual component configurations tested. At $\psi = 0^\circ$ (fig. 65(a)) and $\psi = 5^\circ$ (fig. 66(a)), little difference in D/q is observed between configurations with common hub fairings but different pylon fairings. The dominating aerodynamic effects are due to the type of hub fairing used.

The M/q curves (figs. 65(c) and 66(c)) point to a substantial loss in horizontal tail effectiveness below the baseline (unfaired) value with the Dual Component #1 at negative values of α . This illustrates the rather high sensitivity of the tail effectiveness not only to the presence of a pylon fairing but also to large hub fairing configurations. Notice from figure 65(c) that the extremes in M/q (for $\alpha < 0^\circ$) are both due to integrated hub and pylon fairing configurations; whereas the completely unfaired hub data lie in the middle range. This illustrates the wide ranges of pitching moment trends that are observed with integrated fairing configurations. The Y/q and N/q curves (figs. 67(a) and 67(b)) also illustrate the wide range of loads measured during this test and the effects of those loads on directional stability.

RPM and Reynolds Number Effects

RPM Effects

Most of the data presented in this report were acquired for a hub rotational speed of 1500 rpm. Although blades were not installed on the model, this hub RPM was selected so as to match the rotor tip speed if the blades had been present. It was assumed in earlier hub drag studies that hub rotation had little influence on drag trends for hub fairings. Limited RPM sweeps were performed to verify this long-held assumption. Data were not acquired at zero rpm because of mechanical difficulties in locking out the hub and time constraints on the test.

RPM sweeps were performed for the unfaired rotor hub as well as for the 22% hub fairing with the tapered pylon fairing. The variation of longitudinal loads with RPM for the unfaired hub case is shown in figure 68 for $\psi = 0^\circ$. Lateral-directional loads are plotted in figure 69. The RPM sweeps were performed for $\alpha = -10^\circ, 0^\circ, 10^\circ$, and 16° at $\psi = 0^\circ$ which covered the range of α selected for this test. No ψ sweeps were performed. For the unfaired hub, figures 68 and 69 show almost no influence of hub RPM on the measured model forces and moments. The variation in load with RPM observed in figure 69(c) for RM/q is probably caused by the weight tare hysteresis effect on the curve fit.

Figures 70 and 71 show the RPM sweep results for the integrated 22% hub and pylon fairing case. Again, no RPM effect is observed for most of the forces and moments.

Reynolds Number Effects

The sensitivity of the model forces and moments associated with variations in Reynolds number was also

studied during this test. As in the preceding section, data were acquired for two configurations: the unfaired rotor hub and mast configuration, and the 22% hub fairing with the tapered pylon fairing. The impact of Reynolds number on the lift, drag, and pitching moment variation with fuselage angle of attack is shown in the following figures. Lateral-directional data were not acquired for this case.

The data acquired for the unfaired rotor and mast configuration at three values of Reynolds number are shown in figure 72 ($\psi = 0^\circ$) and figure 73 ($\psi = 5^\circ$). The Reynolds numbers correspond to tunnel dynamic pressures of 40, 60 and 80 psf. In figure 72(a), the D/q data show the usual trends expected with variations of Reynolds number. Since the skin friction coefficient decreases as the Reynolds number increases, the overall drag also decreases (ref. 11). The only other noticeable influence of Reynolds number variation is observed in the model pitching moment data, figures 72(c) and 73(c).

Figures 74 and 75 show the variation of longitudinal loads with Reynolds number for the integrated hub and pylon fairing configuration. Again, figure 74(a) shows a reduction in D/q for the highest Reynolds number. At $\psi = 5^\circ$ (fig. 75(a)), this effect is observed for large positive and negative incidence angles only.

Conclusions

The following conclusions can be drawn from the analysis of test results.

1. Minimum model drag was achieved during this study by combining a small circular-arc hub fairing with a nontapered pylon fairing in an integrated configuration. The hub fairing radius was 15% of the rotor's radius, and the pylon fairing cross-sections were defined by NACA 0034 airfoils. Total model drag was reduced by 20.8% as compared to the unfaired rotor hub and mast configuration.
2. Pylon fairings alone with unfaired hubs reduced total model drag by up to 14.5%, as compared to the unfaired hub and rotor mast case.
3. Hub fairings alone with unfaired masts increased model drag.
4. There is an optimal hub fairing size with respect to minimizing drag. The data show conclusively that large hub fairings increased model drag, even when integrated with a pylon fairing.
5. Differences in total model drag associated with pylon fairing geometry seemed to be primarily related to skin friction effects, with the nontapered pylon fairing having a slight advantage.

6. For the model configurations tested, pylon fairings improved horizontal tail effectiveness. The nontapered pylon fairing produced the largest increase in tail effectiveness. This increased the static longitudinal stability in the negative angle of attack range.

7. Very large hub fairings produced a decrease in longitudinal stability.

8. For the configurations tested, pylon fairings decreased static directional stability. This effect can be attributed to fairing planform area, longitudinal position of the pylon fairing relative to the model moment reference center, and to sidewash at the vertical tail.

9. The tapered pylon fairing produced the largest side forces and yawing moment while the inverse tapered pylon fairing was the least directionally destabilizing.

10. Increases in side force and yawing moment were observed when a hub fairing was added to a pylon fairing. This was primarily caused by an endplate effect for the pylon fairings and further destabilized the model directionally.

11. The drag results for the 15% and 22% radius hub fairings were very similar in the positive range of fuselage angle of attack. However, the 22% fairing showed a sharp drag rise at negative incidence angles.

12. Mixed results were obtained when hub fairings that attempt to model the features of a full-scale implementation were tested. The drag measured for these configurations is higher than for their simplified counterparts. Additional design work is necessary to satisfactorily arrive at a fairing concept suitable for implementation on an aircraft where large pylon motions occur.

13. Variations of hub rotation speed from 400 to 1500 rpm caused only negligible effects on aerodynamic loads.

Because of likely differences between the fairing models used in the present study and the full-scale prototypes that could be installed on an actual flight test vehicle, the drag reduction percentages given in this report are to be interpreted only as indicative of trends in low-drag fairing technology. Also, because the equivalent flat plate drag areas of wind tunnel models are usually lower than those of full-scale aircraft, the percentages in drag reduction measured in the present study should not be construed as being attainable drag reduction levels in an absolute sense. A more detailed discussion of this issue can be found in reference 10. It should also be noted that the effects of the pylon fairings on longitudinal and directional static stability described in this report apply strictly

to the Bell Helicopter Textron Model 222 configuration. Somewhat different results would be expected on a helicopter with different horizontal and vertical tail configurations.

References

1. Sheehy, T. W.: A General Review of Helicopter Rotor Hub Drag Data. 31st Annual Forum of the American Helicopter Society, May 1975.
2. Sheehy, T. W. and Clark, D. R.: A Method for Predicting Helicopter Hub Drag. Army Air Mobility Research and Development Laboratory, USAAMRDL-TR-75-48, Jan. 1976.
3. Keys, C. N. and Rosenstein H. J.: Summary of Rotor Hub Drag Data. NASA CR-152080, 1978.
4. Felker, F. F.: An Experimental Investigation of Hub Drag on the XH-59A. AIAA 3rd Applied Aerodynamics Conference, AIAA Paper 85-4065, Oct. 1985, pp. 14-16.
5. Young, L. A.; Graham, D. R.; and Stroub, R. H.: Experimental Investigation of Rotorcraft Hub and Shaft Fairing Drag. AIAA Journal of Aircraft, vol. 24, no. 12, Dec. 1987, pp. 861-867.
6. Young, L. A.; Graham, D. R.; and Stroub, R. H.: Reduction of Hub- and Pylon-Fairing Drag. 43rd Annual Forum of the American Helicopter Society, St. Louis, Missouri, May 1987, pp. 323-344.
7. Graham, D. R.; Sung, D. Y.; Young, L. A.; Louie, A. W.; and Stroub, R. H.: Helicopter Hub Fairing and Pylon Interference Drag Reduction. NASA TM 101052, 1989.
8. Sung, D. Y.; Lance, M. B.; Young, L. A.; and Stroub, R. H.: An Experimental Investigation of Helicopter Rotor Hub Fairing Drag Characteristics. NASA TM-102182, 1989.
9. Squires, P. K.: Investigation of Correlation Between Full Scale and Fifth Scale Wind Tunnel Tests of a Bell Helicopter Textron Model 222. NASA CR-166362, 1982.
10. Martin, D. M.; Mort, R. W.; Squires, P. K.; and Young, L. A.: Hub and Pylon Fairing Integration for Helicopter Drag Reduction. 47th Annual Forum of the American Helicopter Society, Phoenix, Arizona, May 1991, pp. 897-912.
11. Schlichting, H.: Boundary Layer Theory. Seventh Edition, McGraw-Hill, New York, 1979.

ORIGINAL PAGE
BLACK AND WHITE PHOTOGRAPH

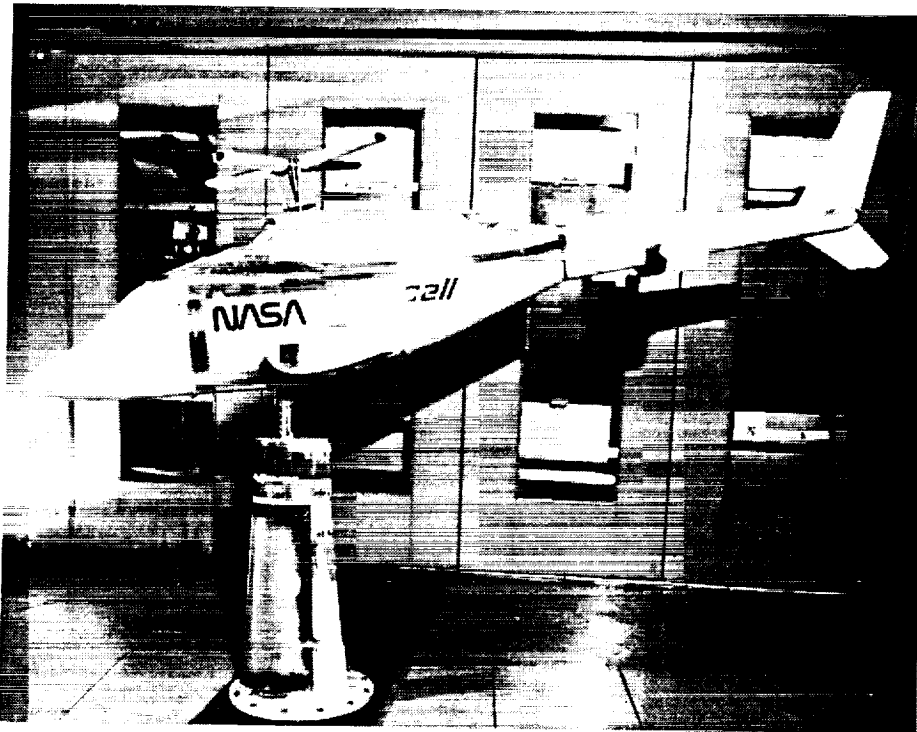


Figure 1. Baseline unfaired model of a Bell M-222 in wind tunnel. (a) Side view.

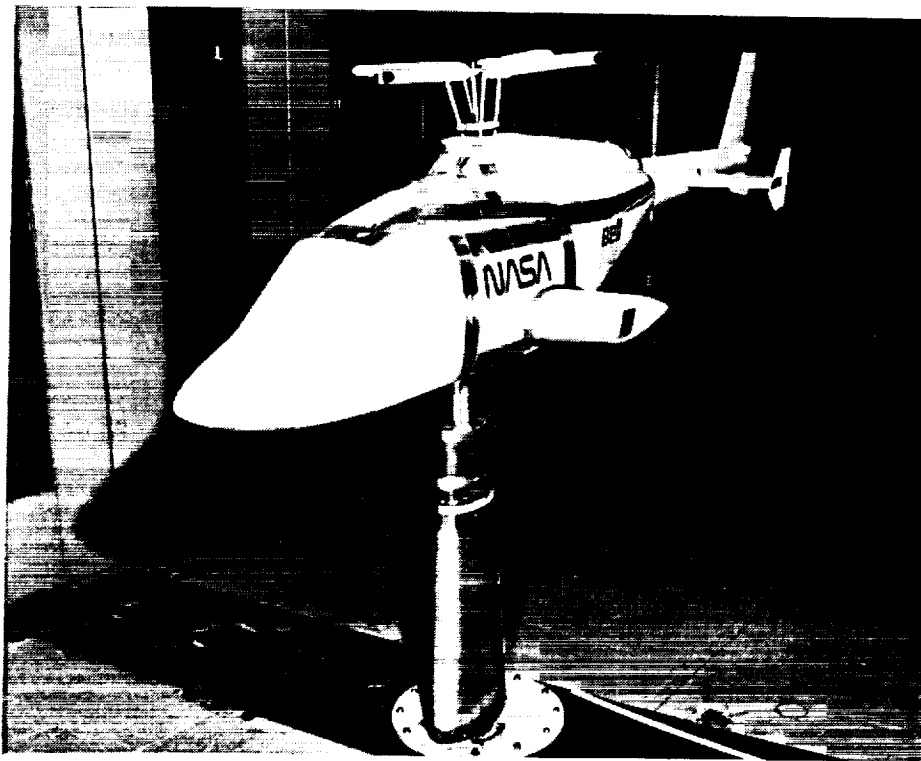


Figure 1. Concluded. (b) front view.

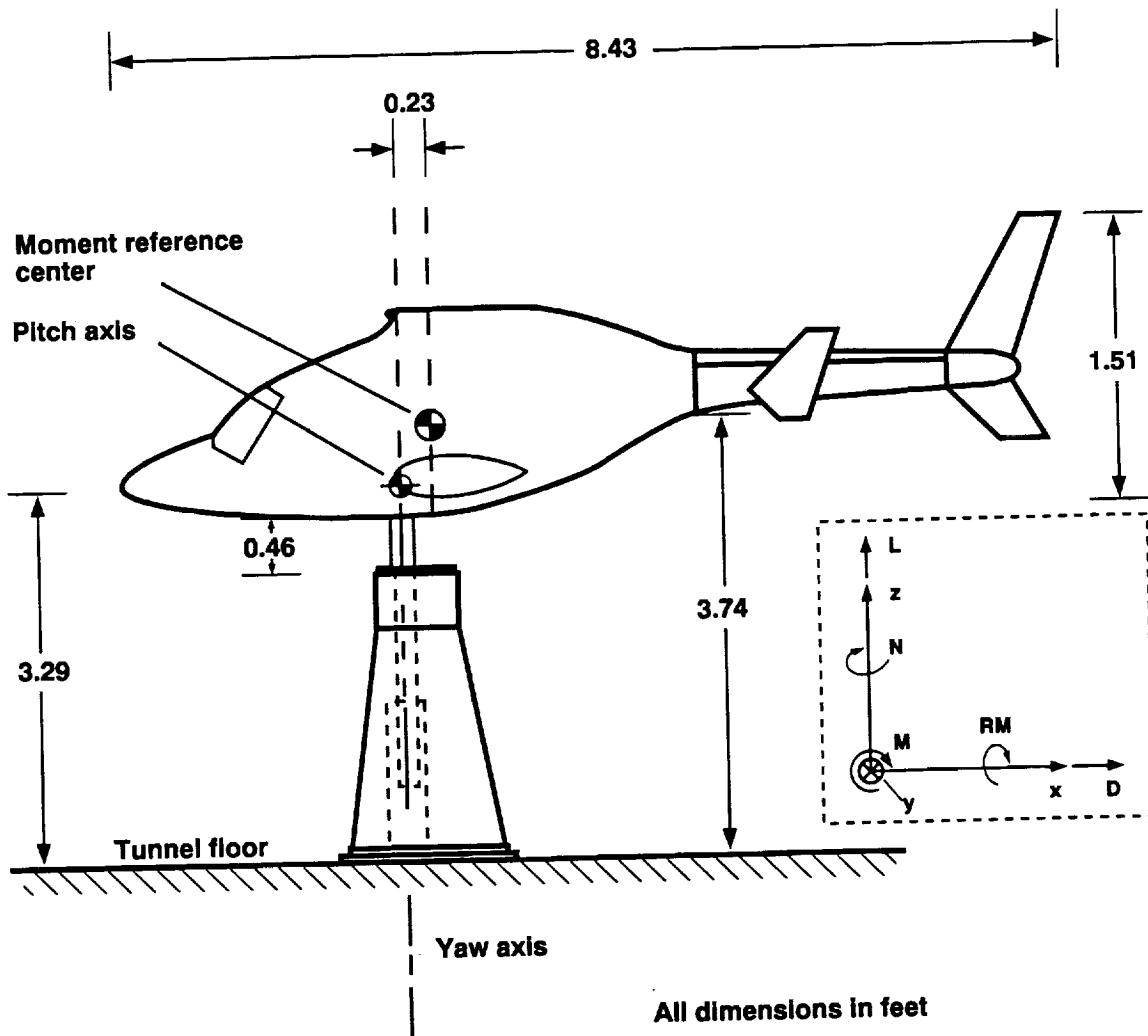


Figure 2. Wind tunnel model configuration with positive directions for aerodynamic loads.

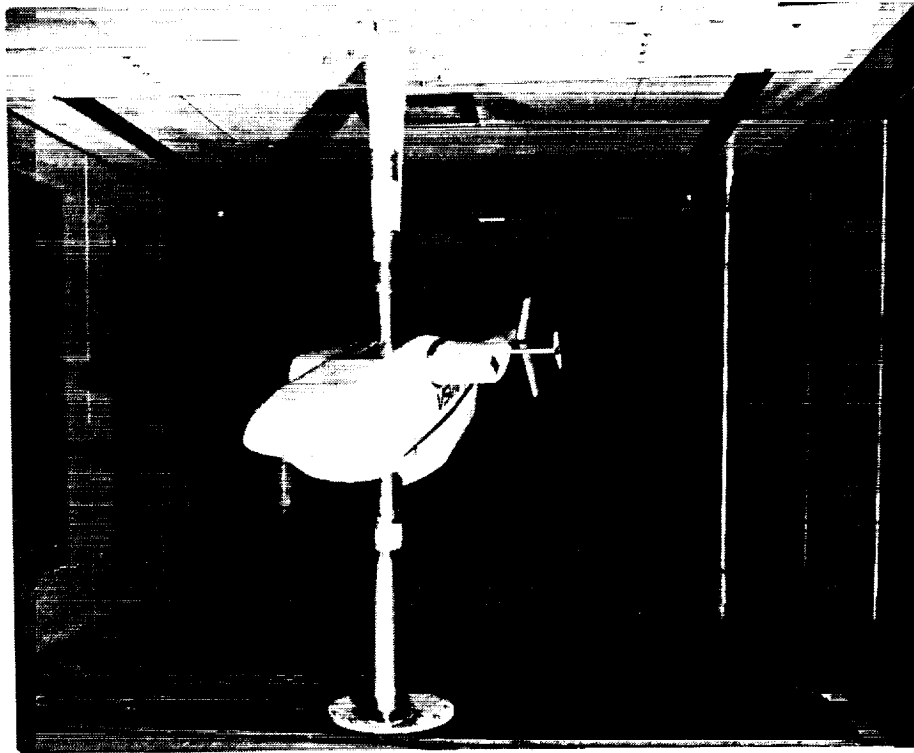


Figure 3. Model in inverted configuration with strut fairing image system. (a) Front view.

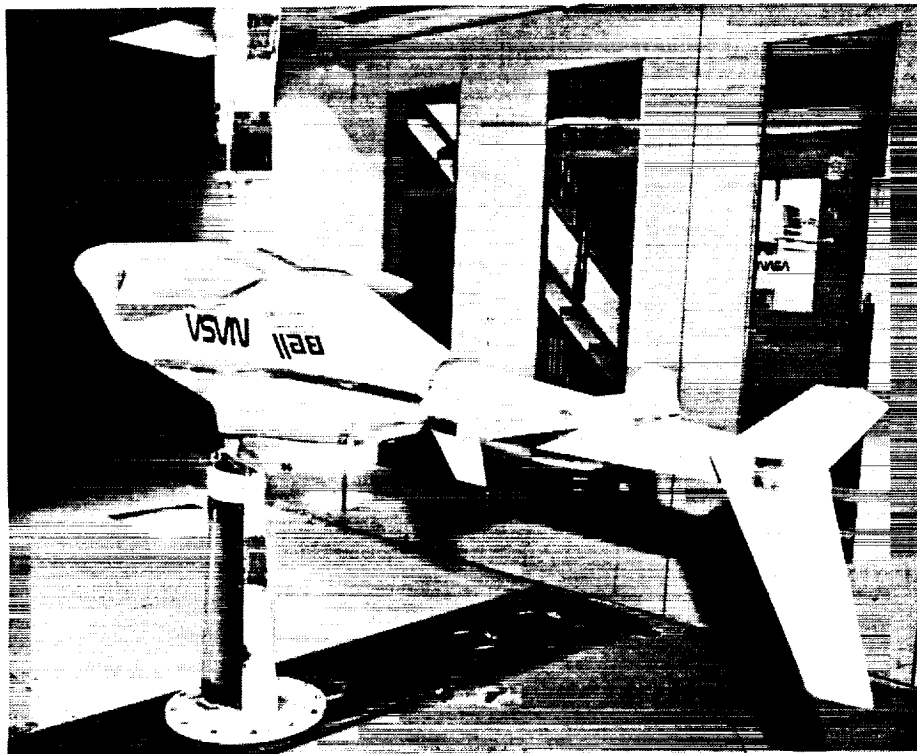


Figure 3. Concluded. (b) aft view.

ORIGINAL PAGE
BLACK AND WHITE PHOTOGRAPH

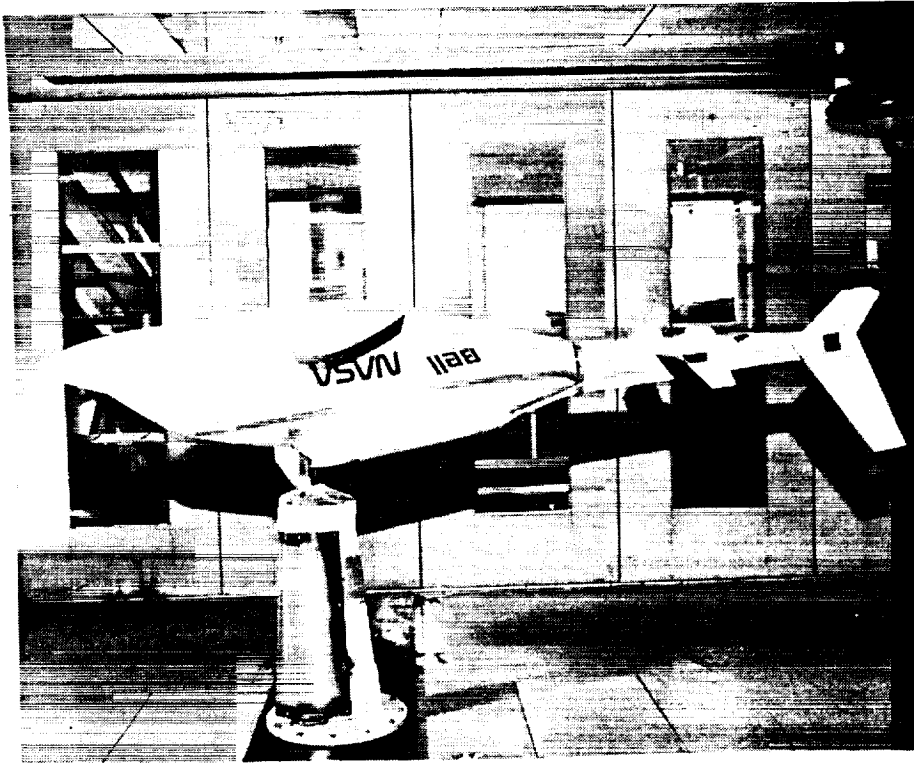


Figure 4. Model in inverted configuration with image system removed. (a) Side view.

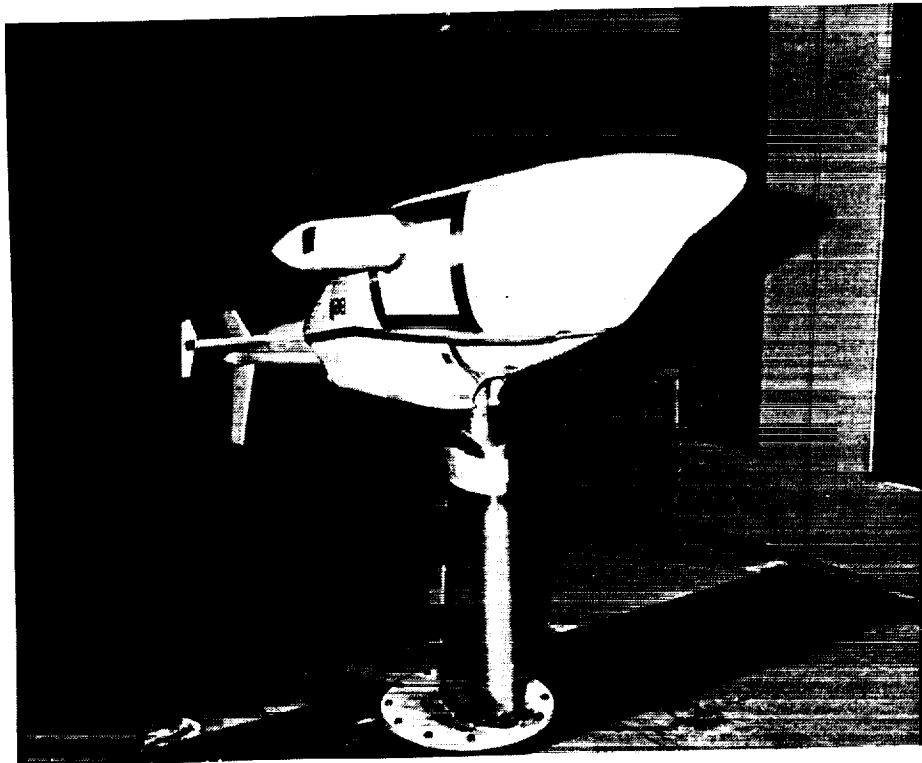


Figure 4. Concluded. (b) front view.

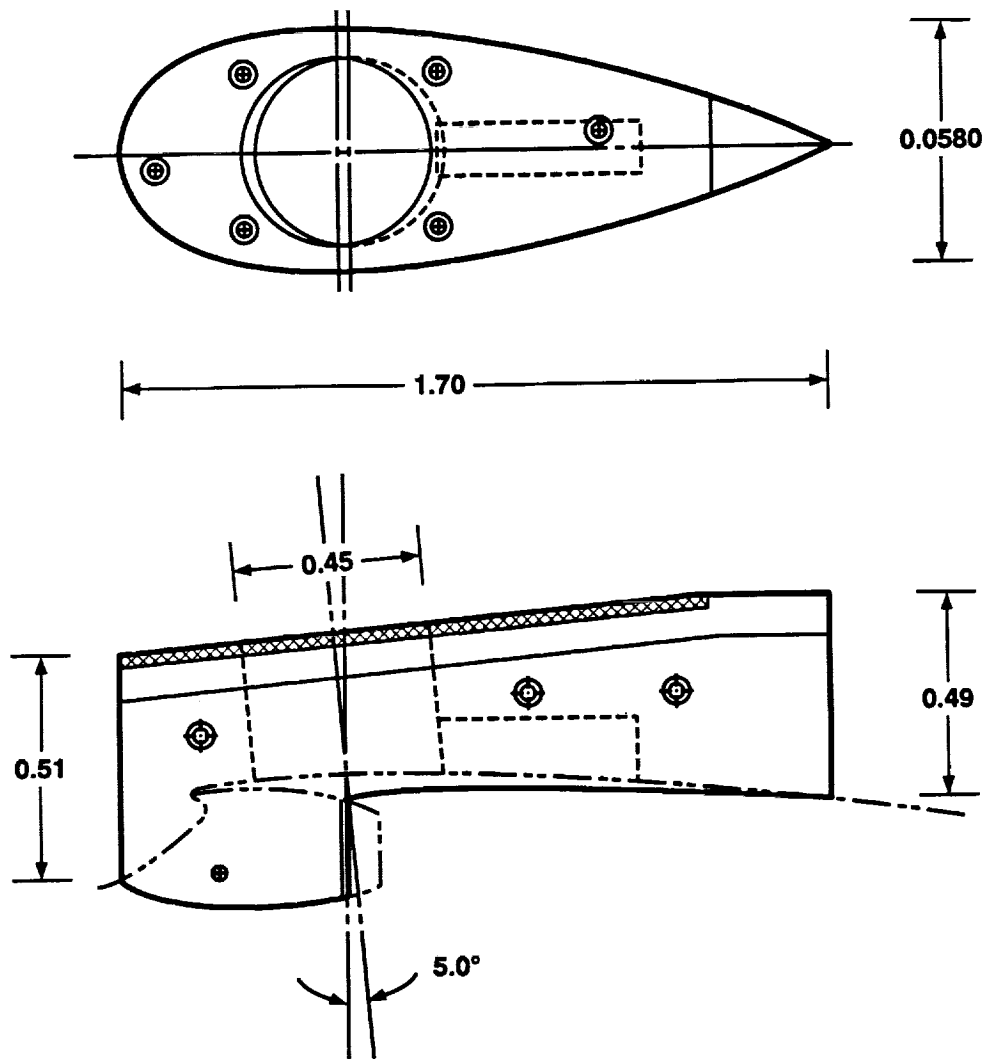


Figure 5. NACA 0034 nontapered pylon fairing.

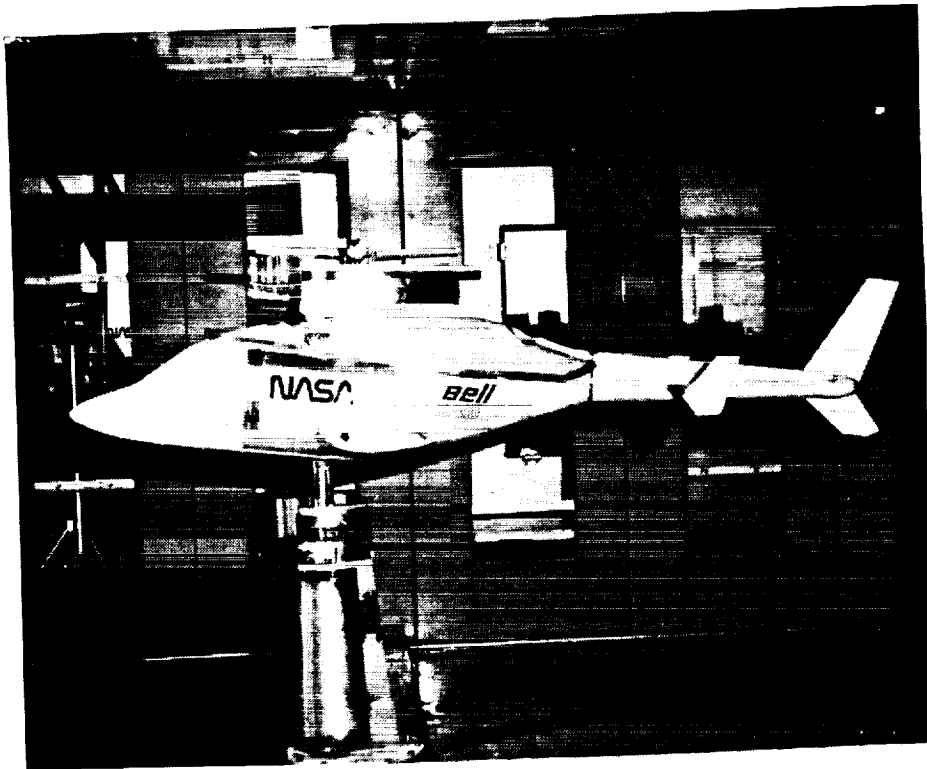


Figure 6. Model with nontapered pylon fairing installed. (a) Side view.

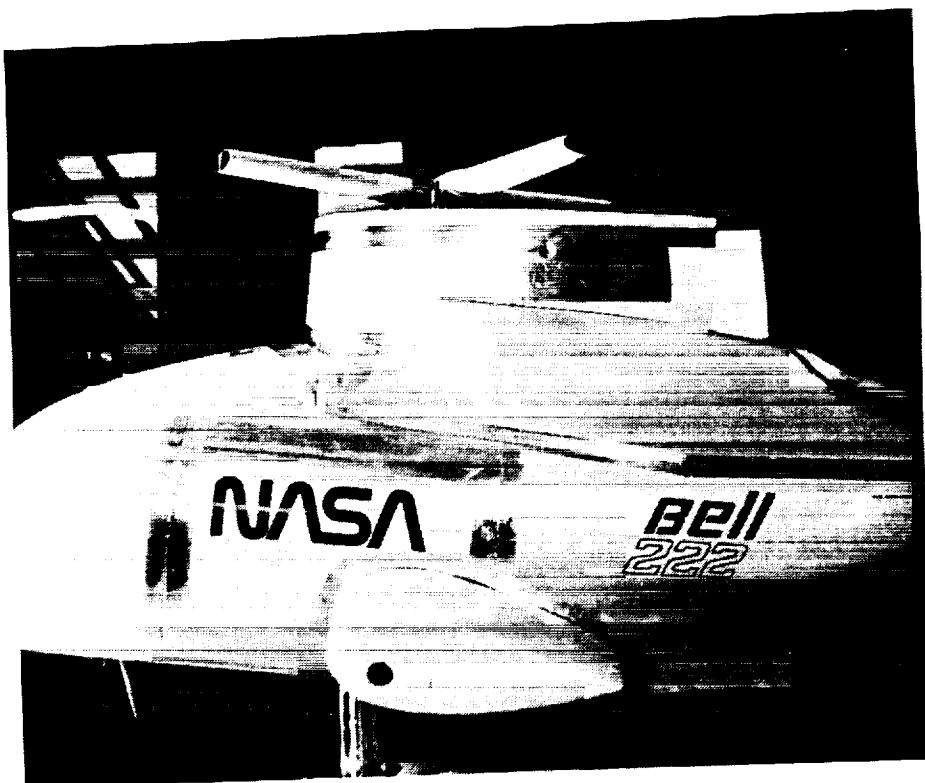


Figure 6. Concluded. (b) close-up view.

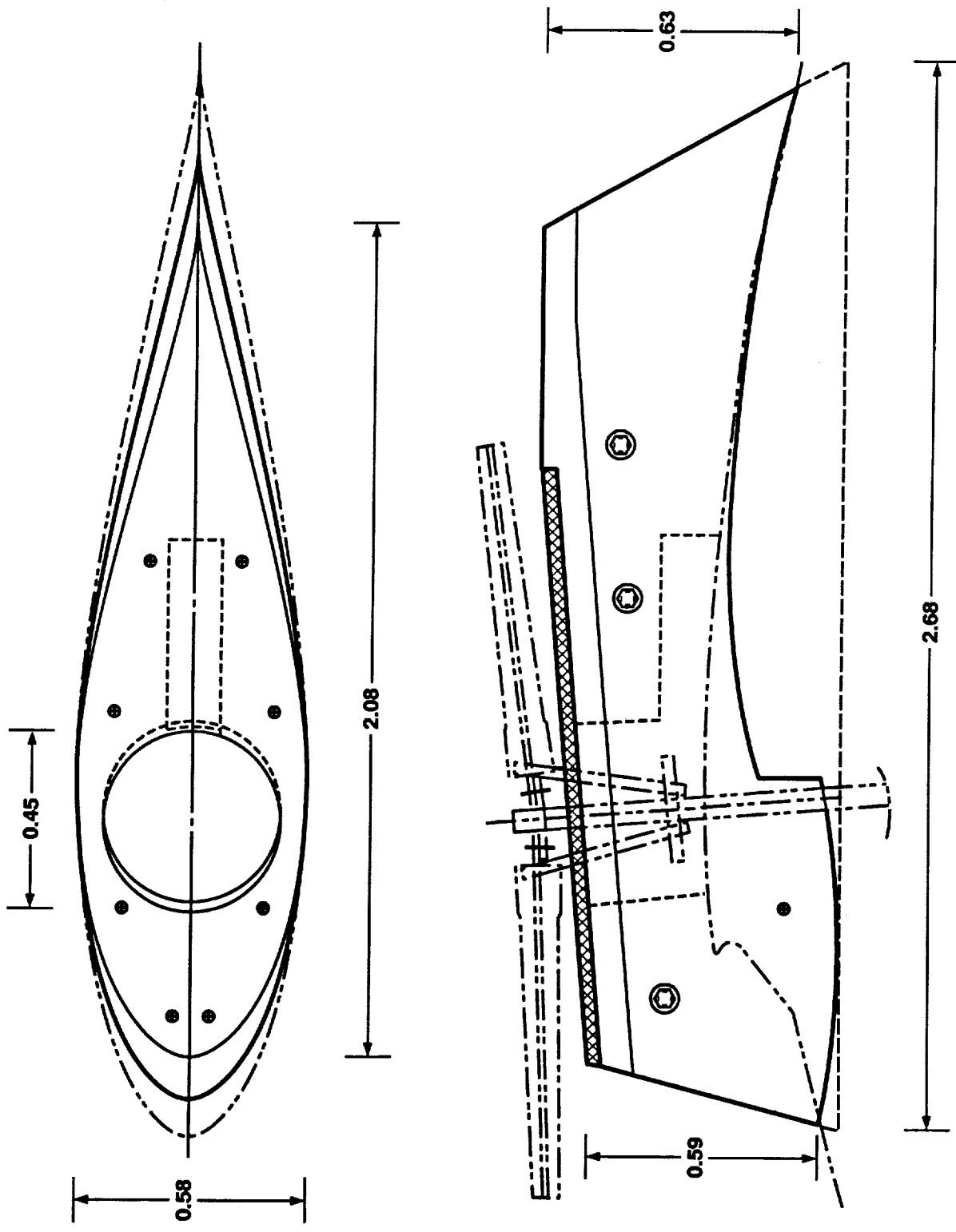


Figure 7. 63-series tapered pylon fairing.

ORIGINAL PAGE
BLACK AND WHITE PHOTOGRAPH



Figure 8. Model with tapered pylon fairing installed. (a) Side view.

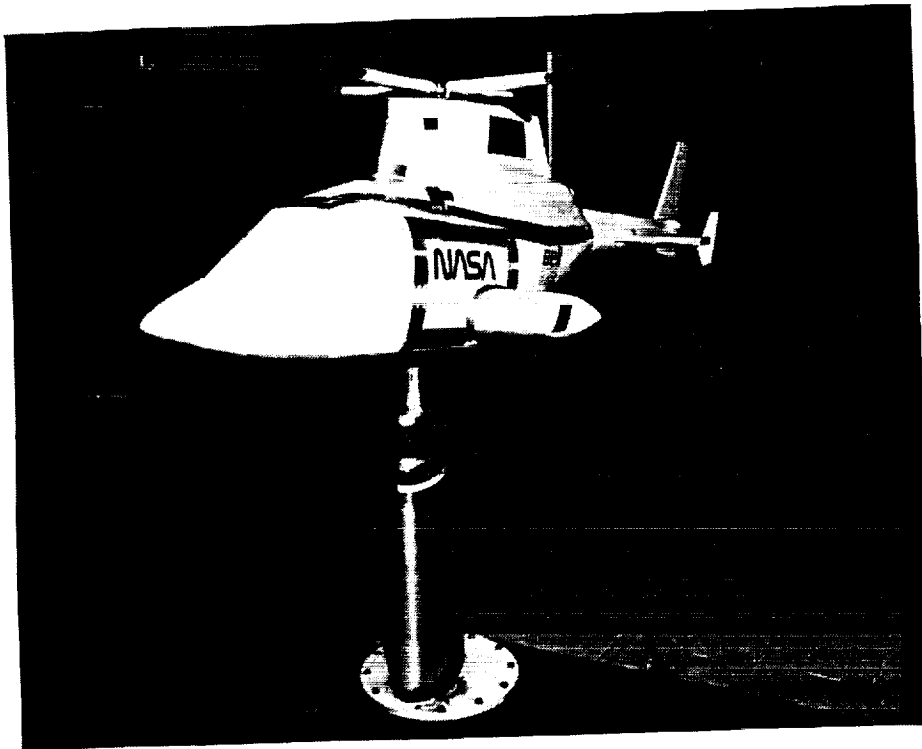


Figure 8. Concluded. (b) front view.

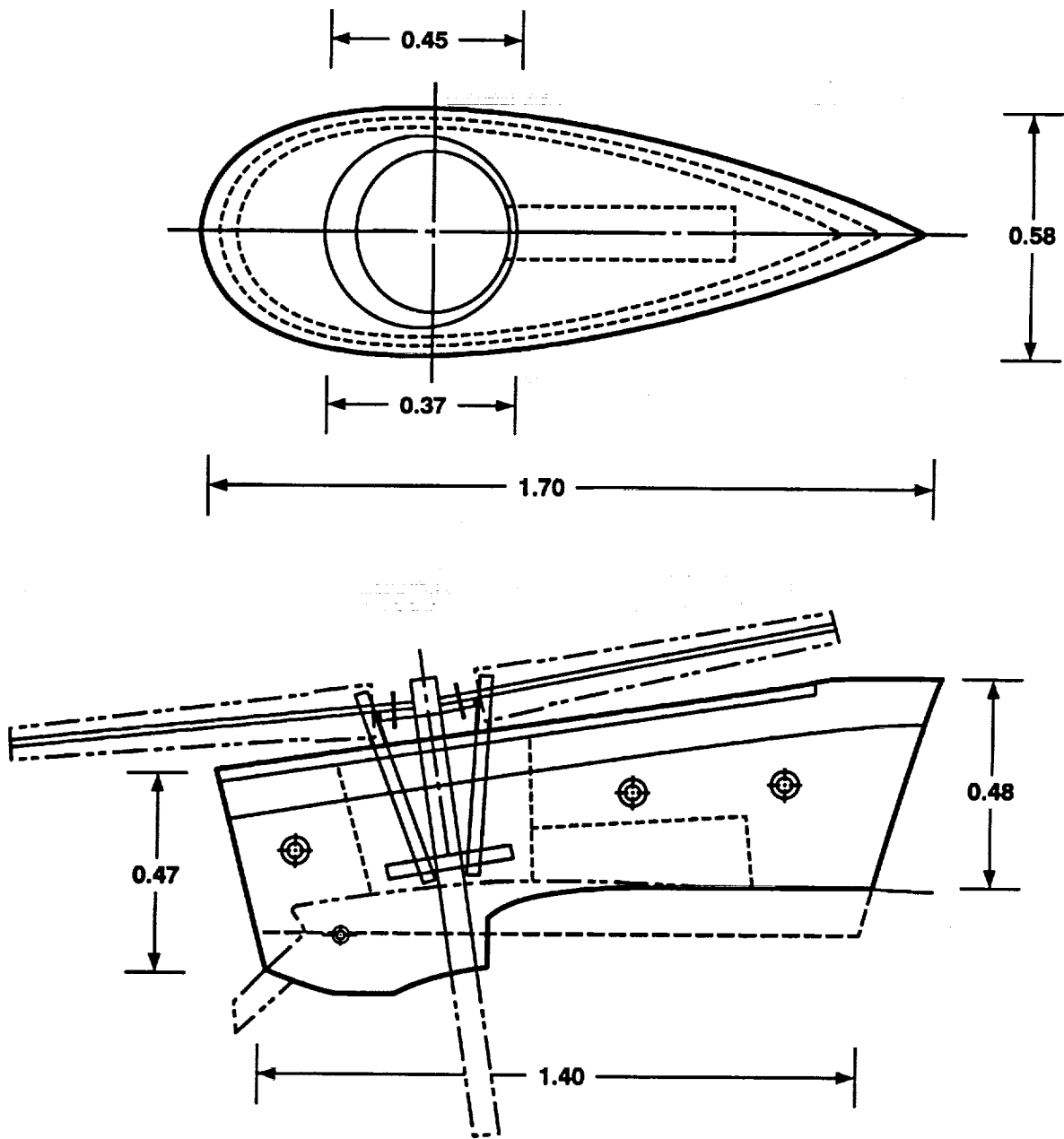


Figure 9. Inverse tapered pylon fairing.

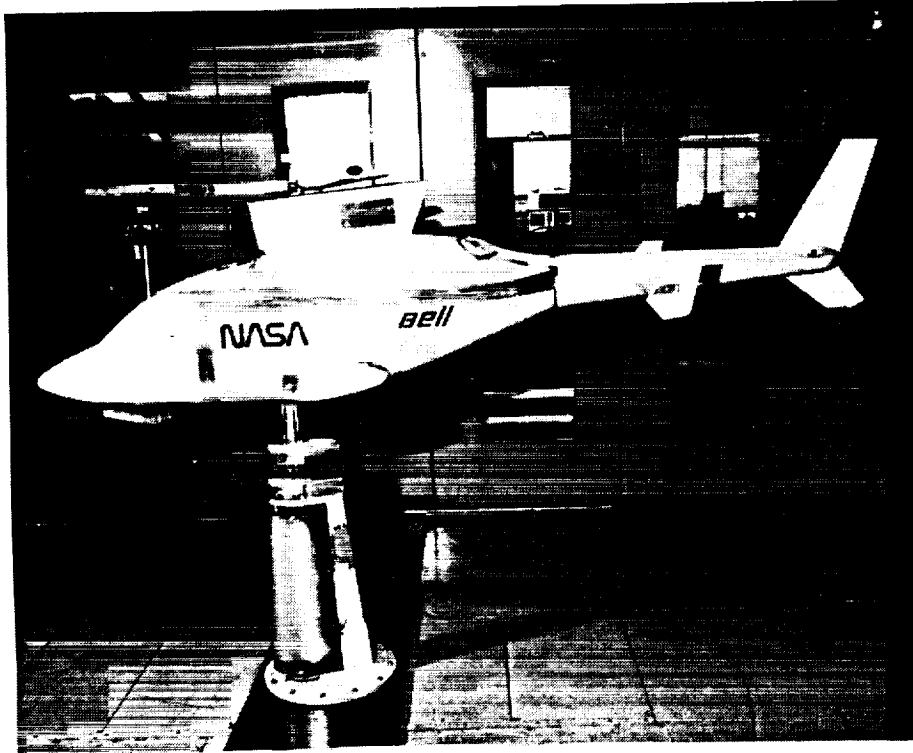


Figure 10. Model with inverse tapered pylon fairing installed. (a) Side view.

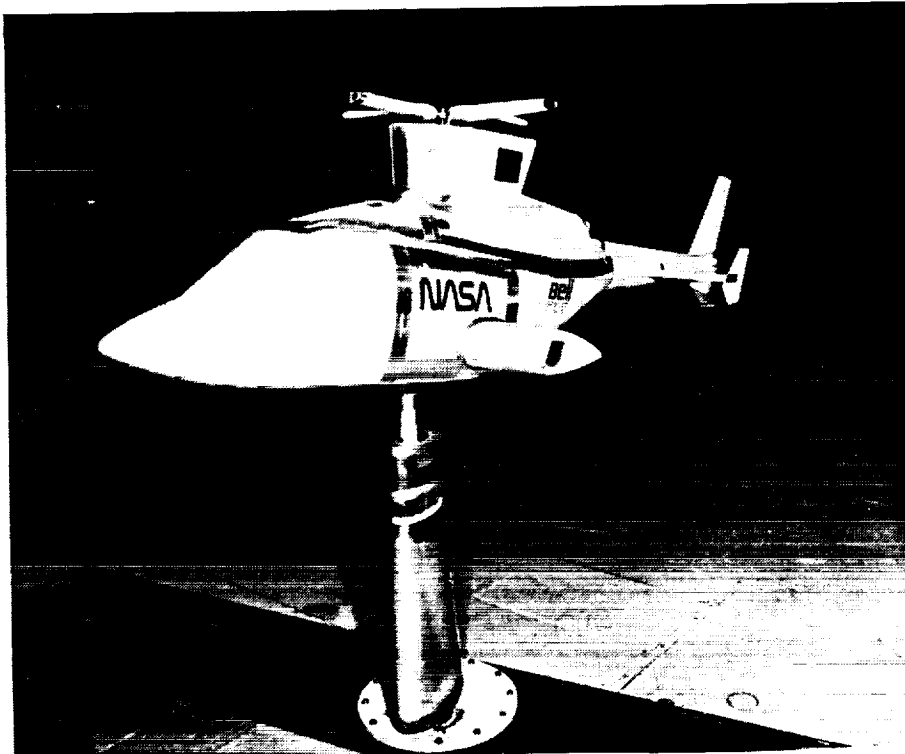


Figure 10. Concluded. (b) front view.

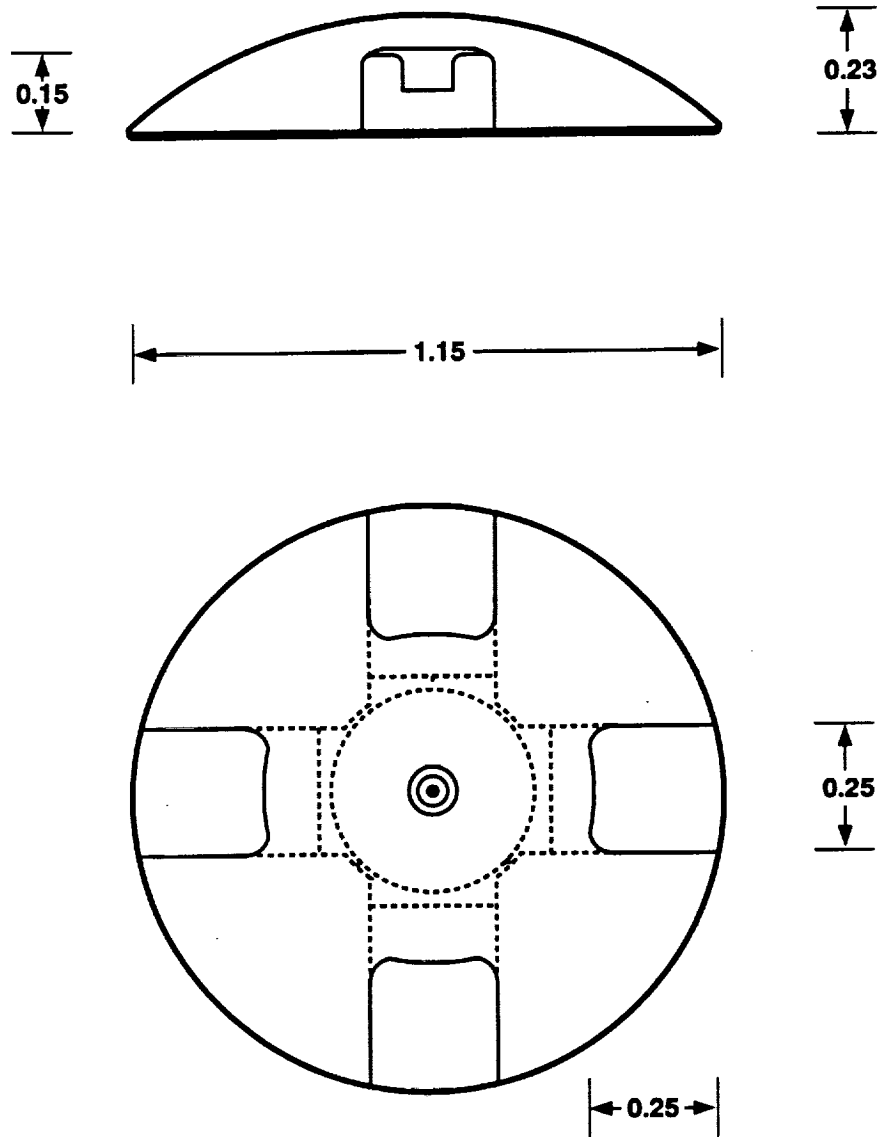


Figure 11. 15% rotor radius hub fairing.

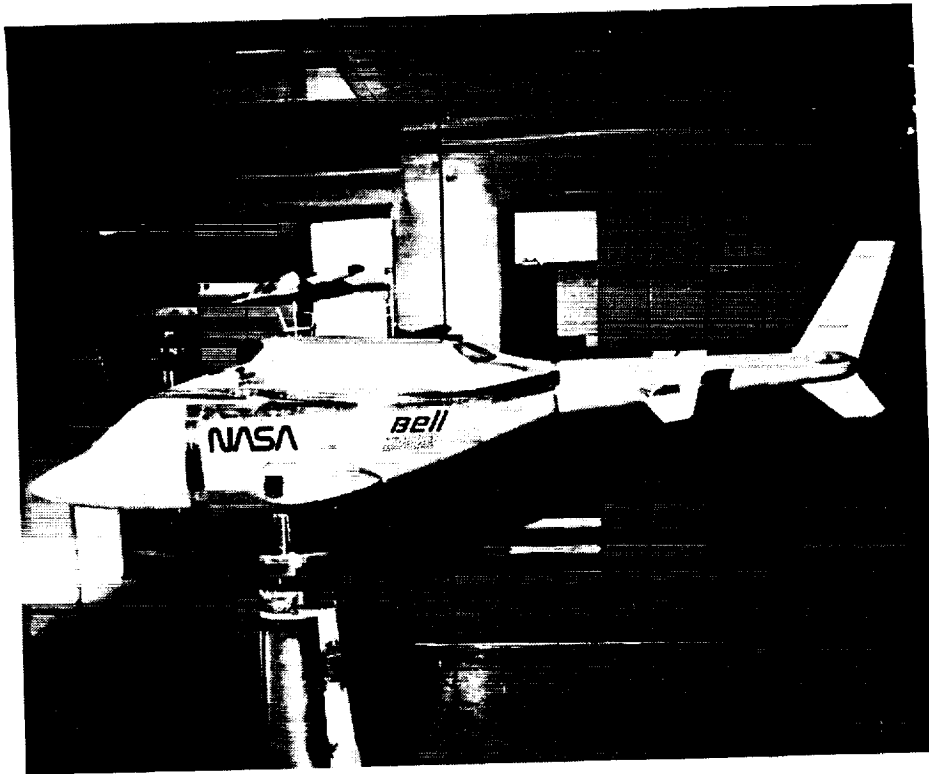


Figure 12. Model with 15% hub fairing installed. (a) Side view.

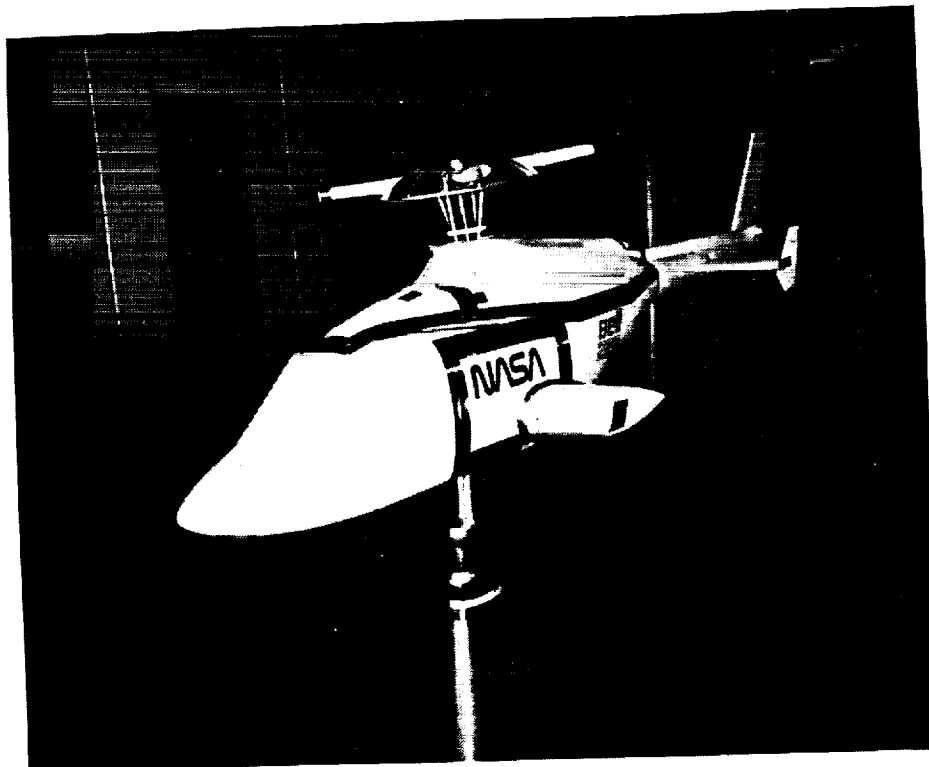


Figure 12. Concluded. (b) front view.

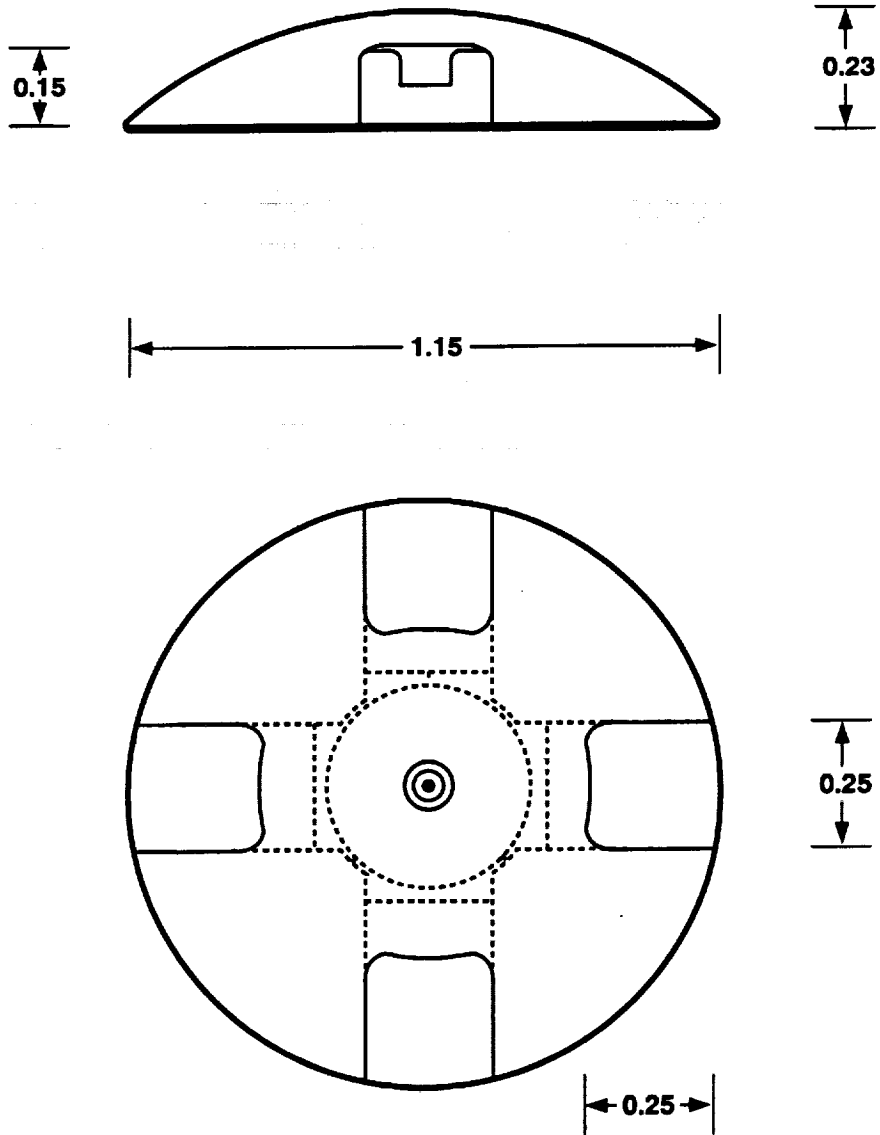


Figure 13. 22% rotor radius hub fairing.

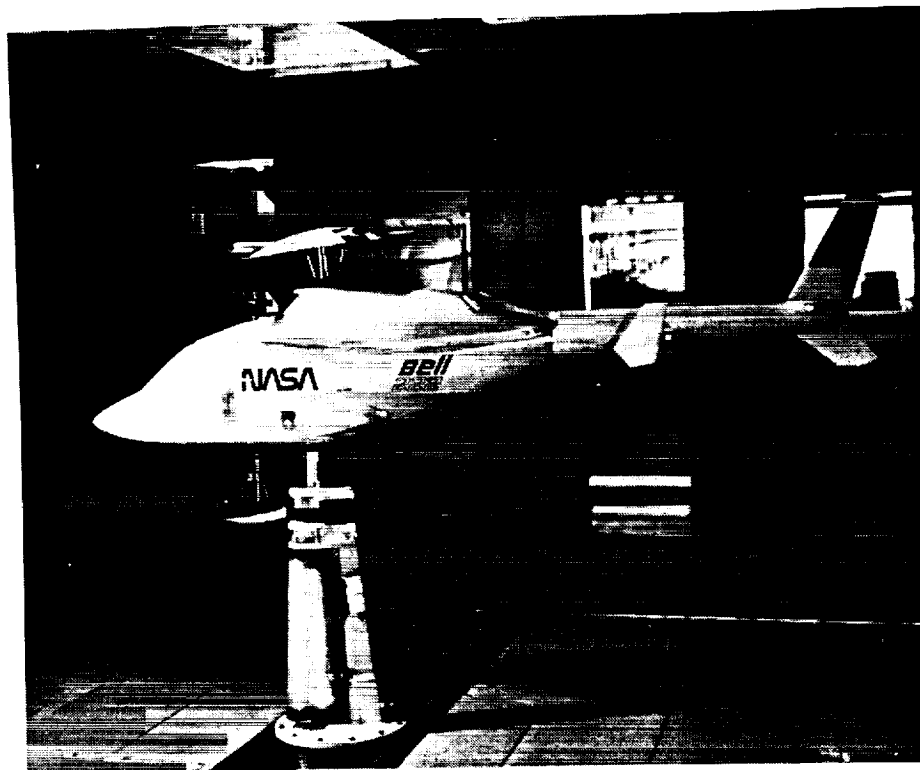


Figure 14. Model with 22% hub fairing installed. (a) Side view.

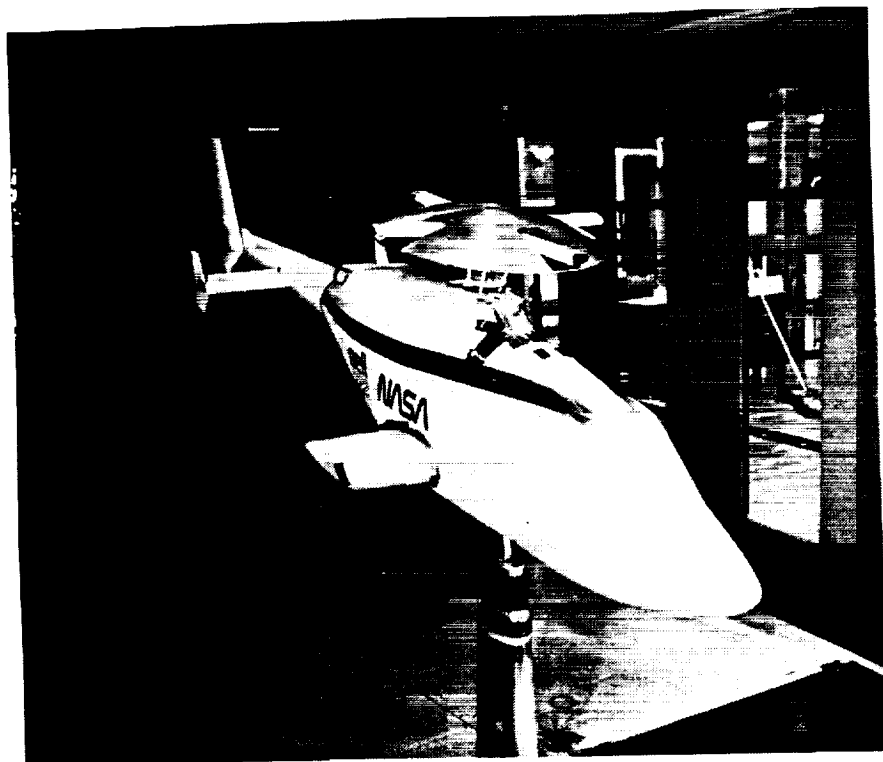


Figure 14. Concluded. (b) front view.

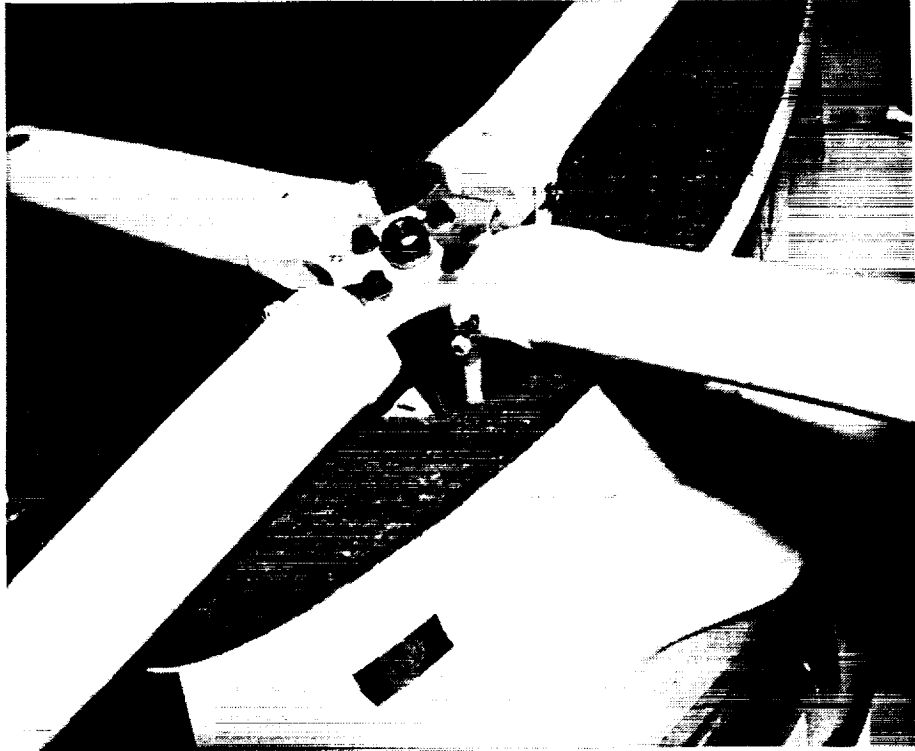


Figure 15. Close-up view of top of pylon fairing with felt layer. (a) Top view.

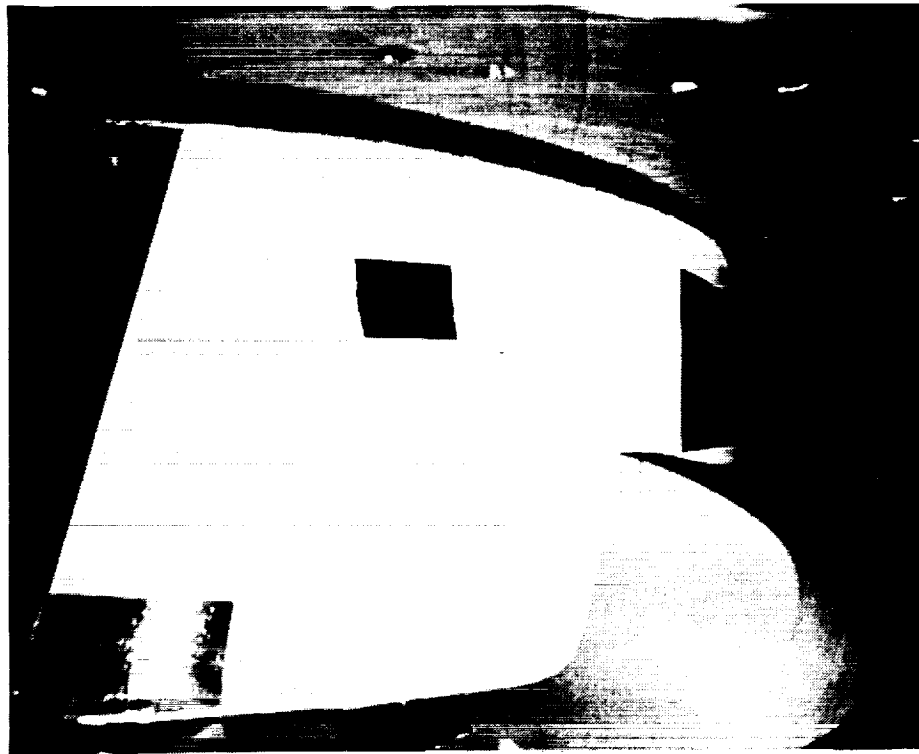


Figure 15. Concluded. (b) bottom view with hub fairing.

ORIGINAL PAGE
BLACK AND WHITE PHOTOGRAPH



Figure 16. Model with 15%/nontapered integrated hub and pylon fairing configuration. (a) Side view.

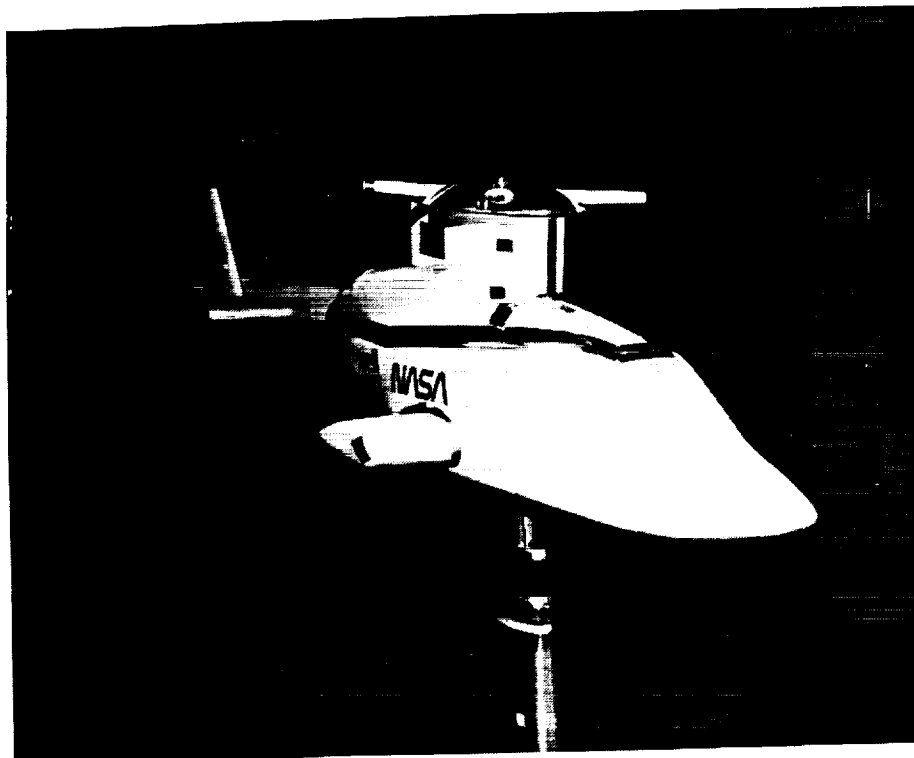


Figure 16. Concluded. (b) front view.



Figure 17. Model with 15%/tapered integrated hub and pylon fairing configuration. (a) Side view.

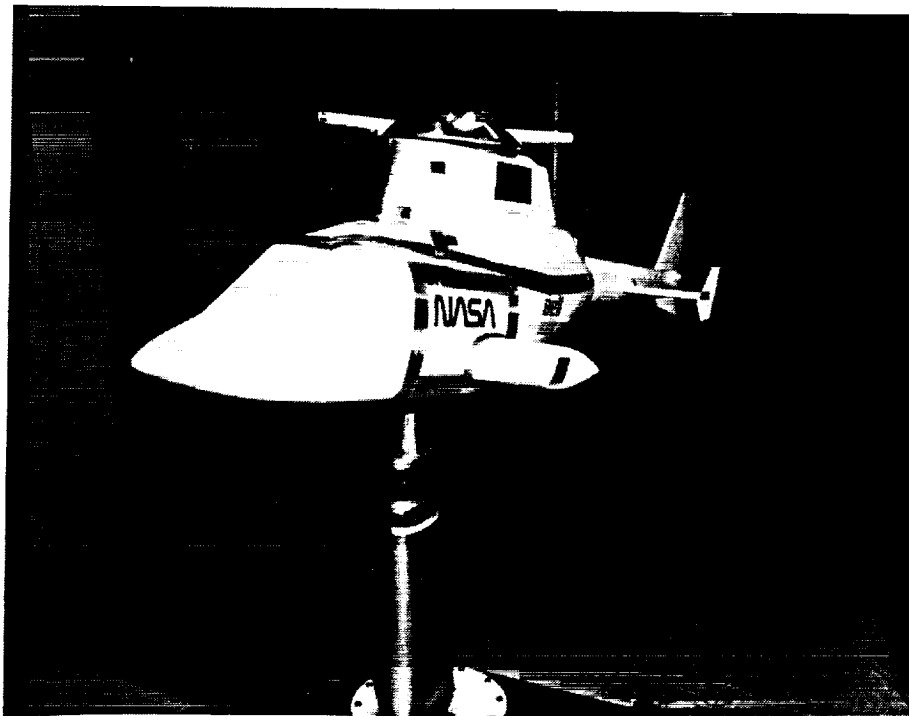


Figure 17. Concluded. (b) front view.

ORIGINAL PAGE
BLACK AND WHITE PHOTOGRAPH

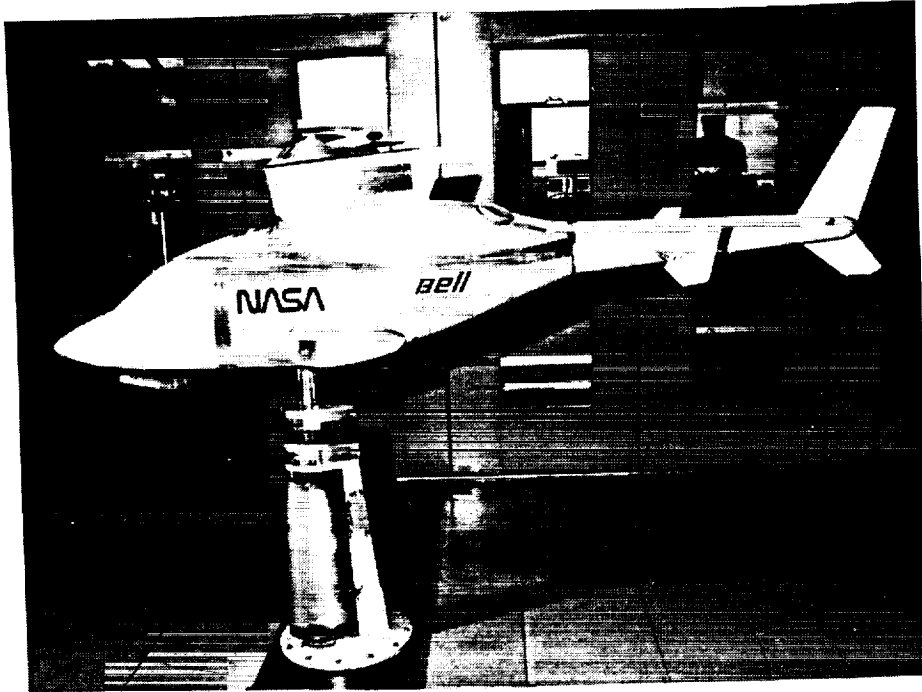


Figure 18. Model with 15% inverse tapered integrated hub and pylon fairing configuration. (a) Side view.

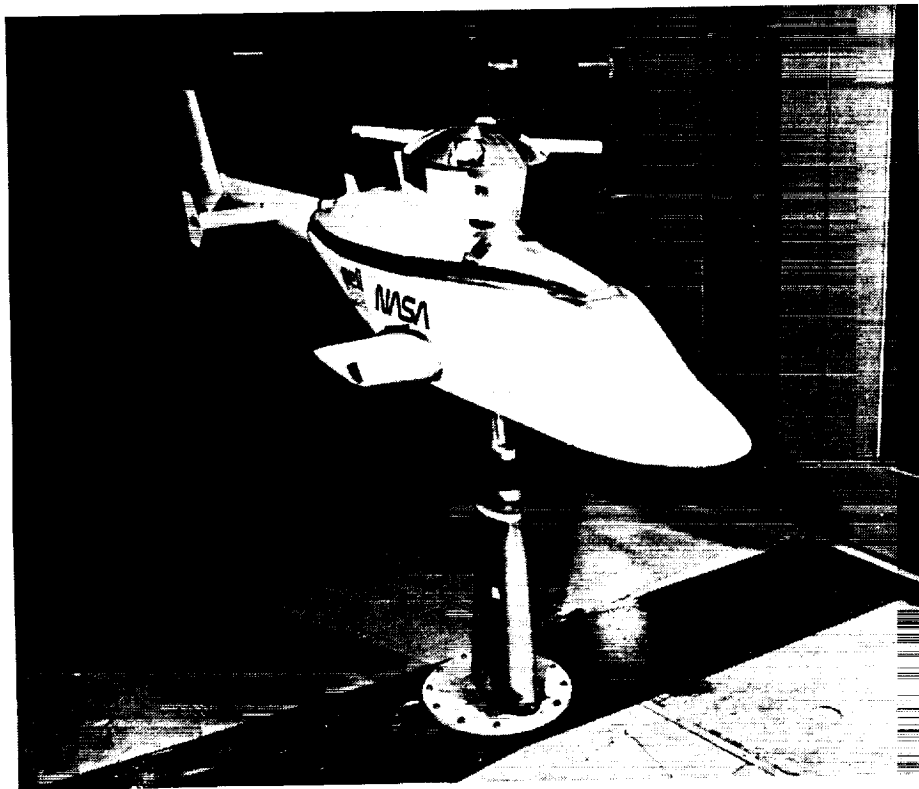


Figure 18. Concluded. (b) front view.

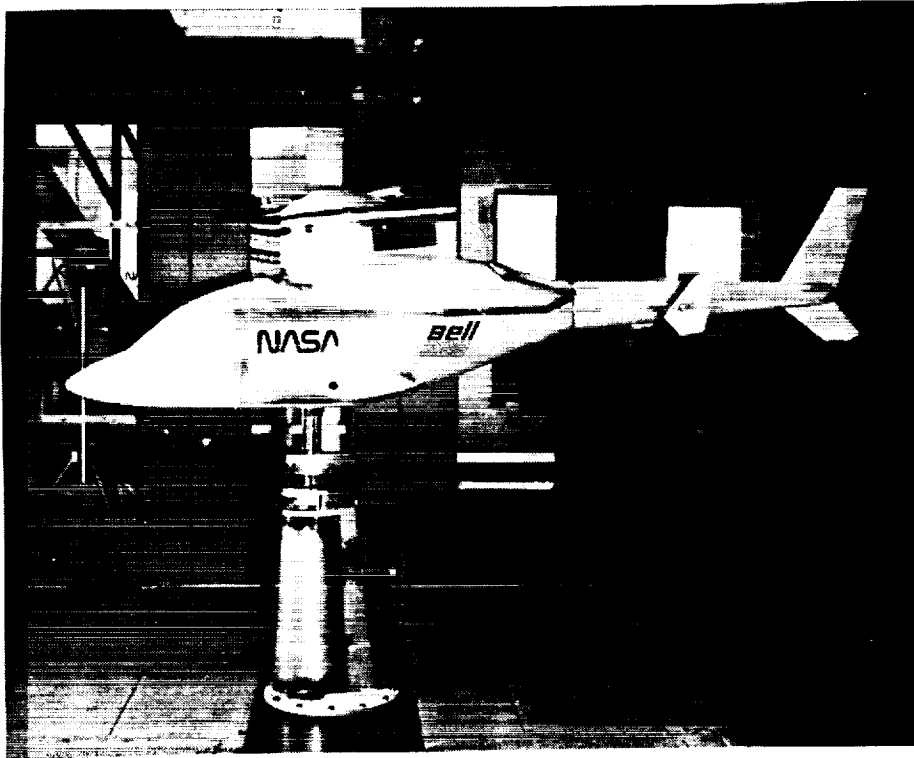


Figure 19. Model with 22%/nontapered integrated hub and pylon fairing configuration. (a) Side view.

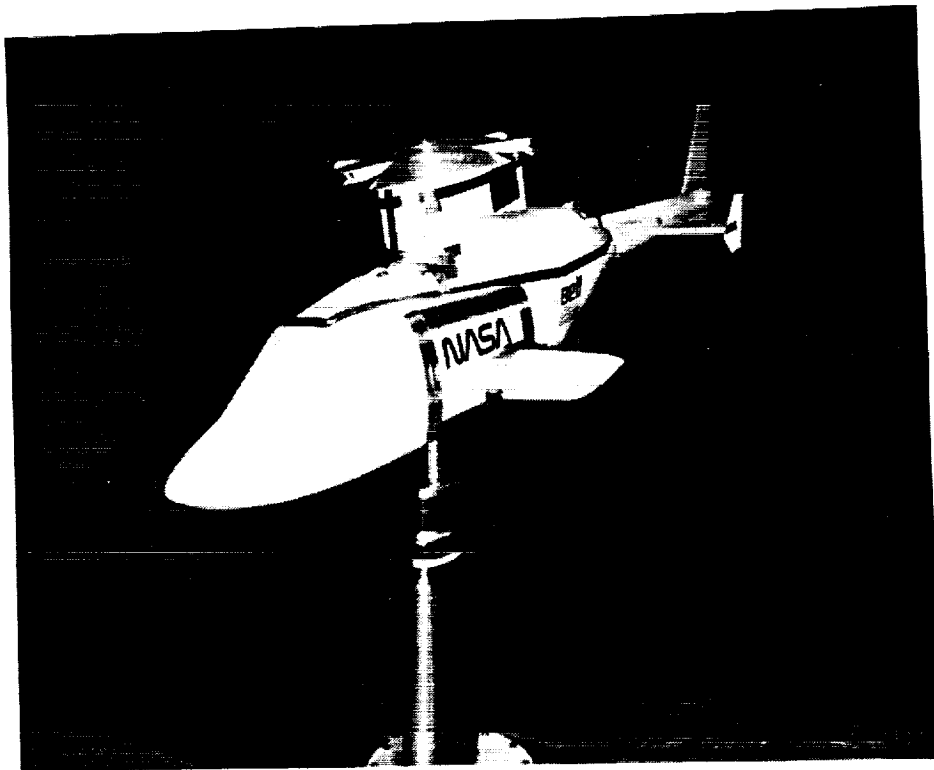


Figure 19. Concluded. (b) front view.

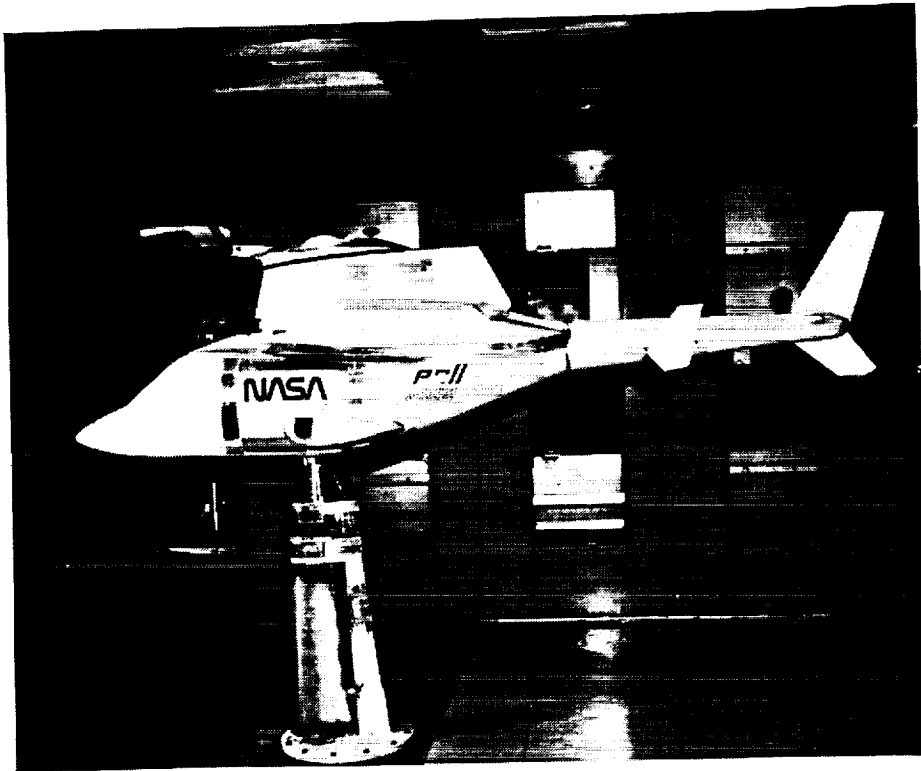


Figure 20. Model with 22% tapered integrated hub and pylon fairing configuration. (a) Side view.

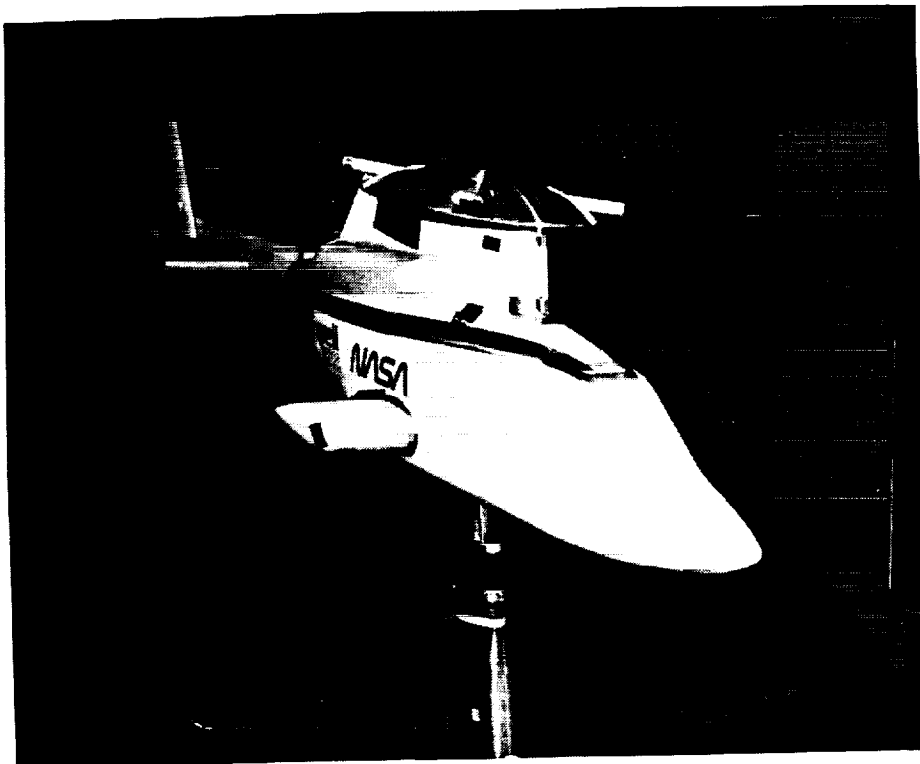


Figure 20. Concluded. (b) front view.

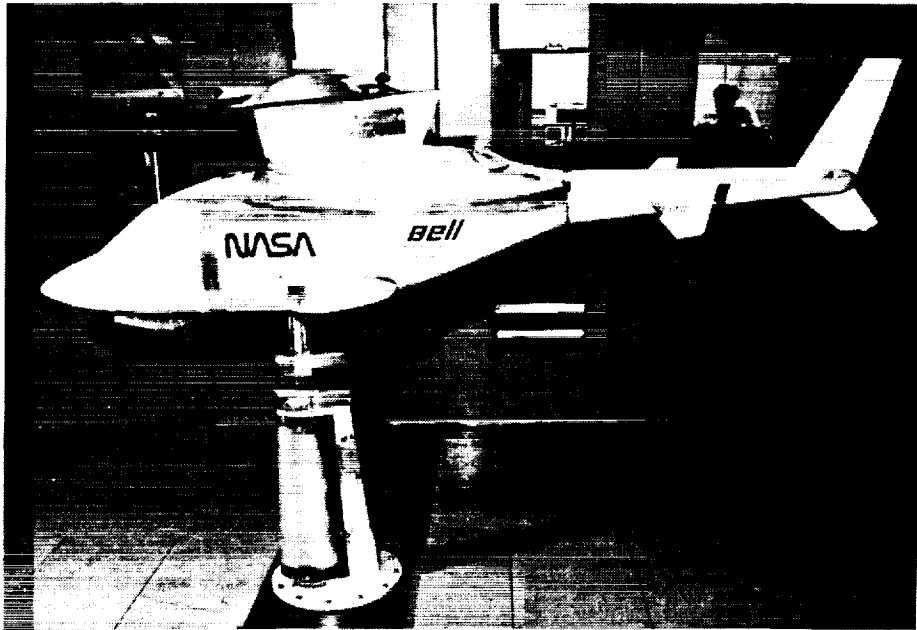


Figure 21. Model with 22% inverse tapered integrated hub and pylon fairing configuration. (a) Side view.

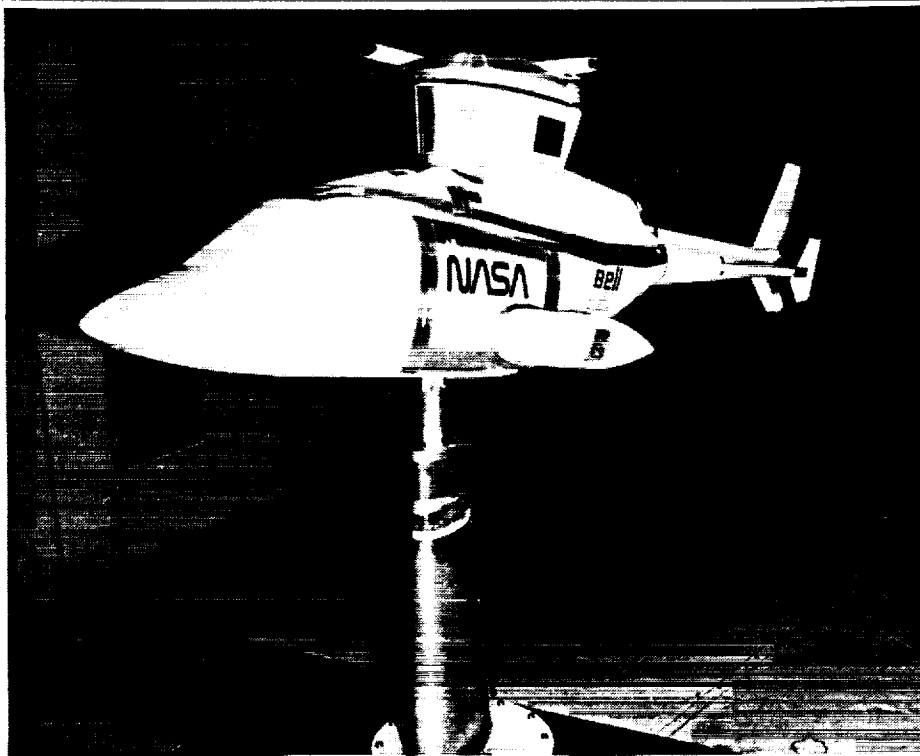


Figure 21. Concluded. (b) front view.

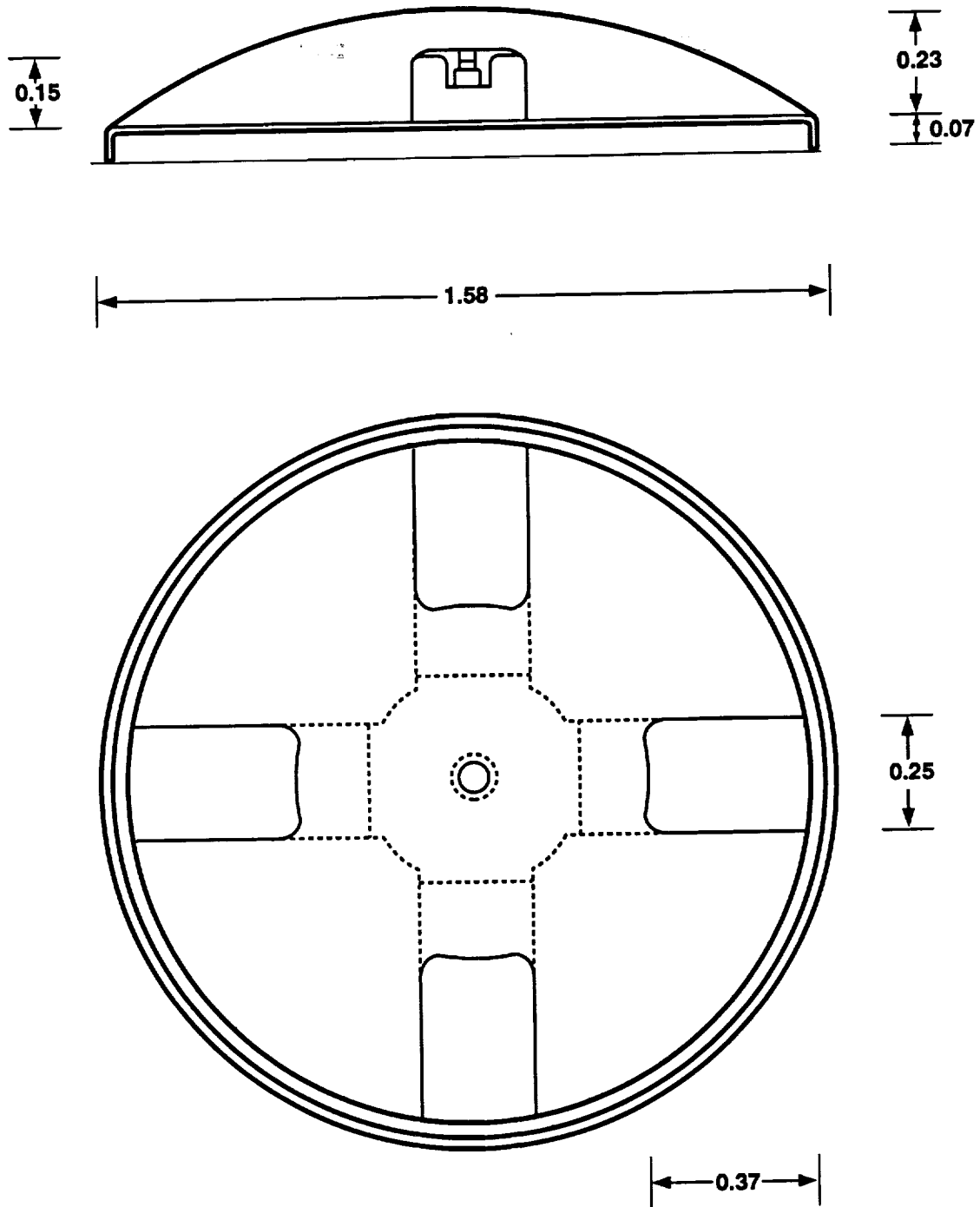


Figure 22. Dual Component #1 rotating assembly.

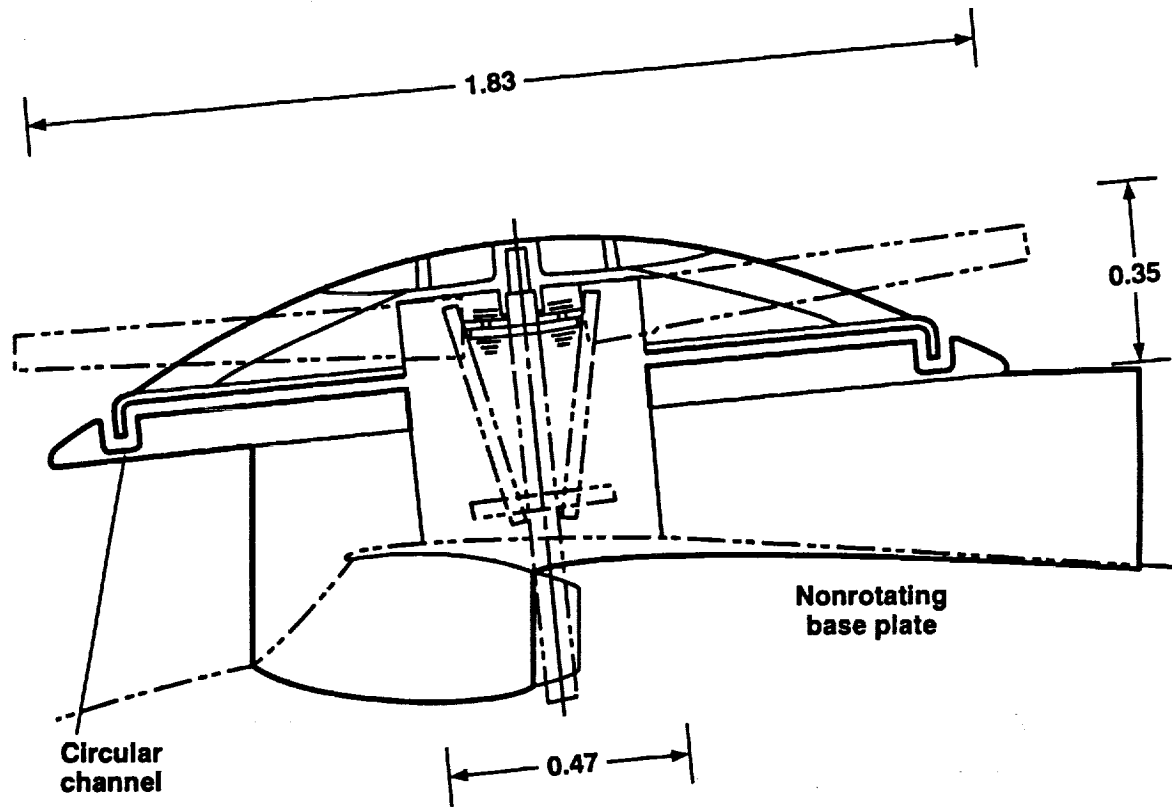


Figure 23. Dual Component #1 rotating and nonrotating hardware mounted on hub and nontapered pylon fairing.

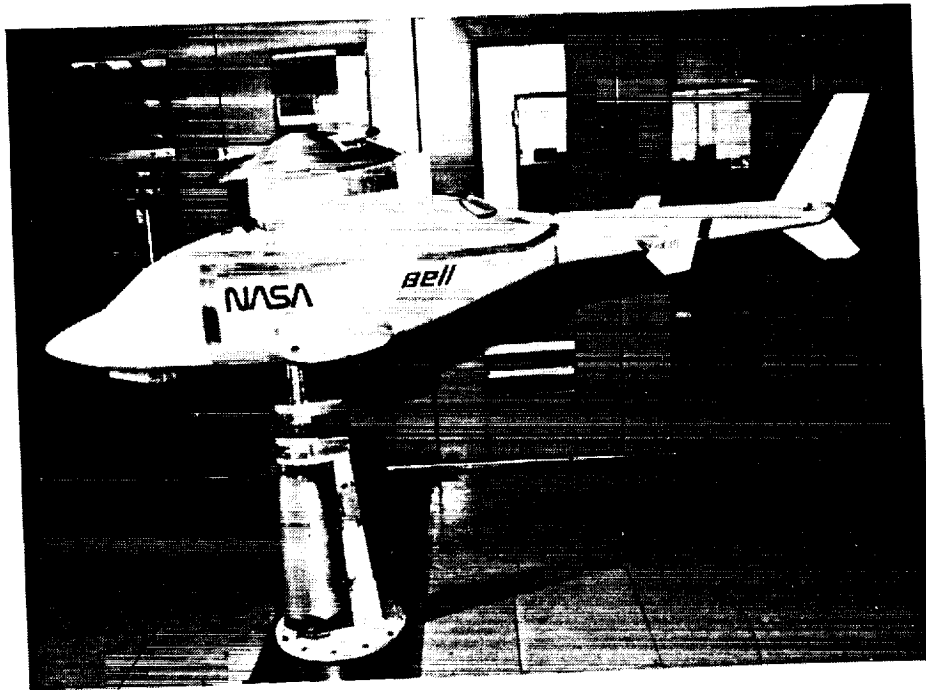


Figure 24. Model with Dual Component #1 configuration. (a) Side view.

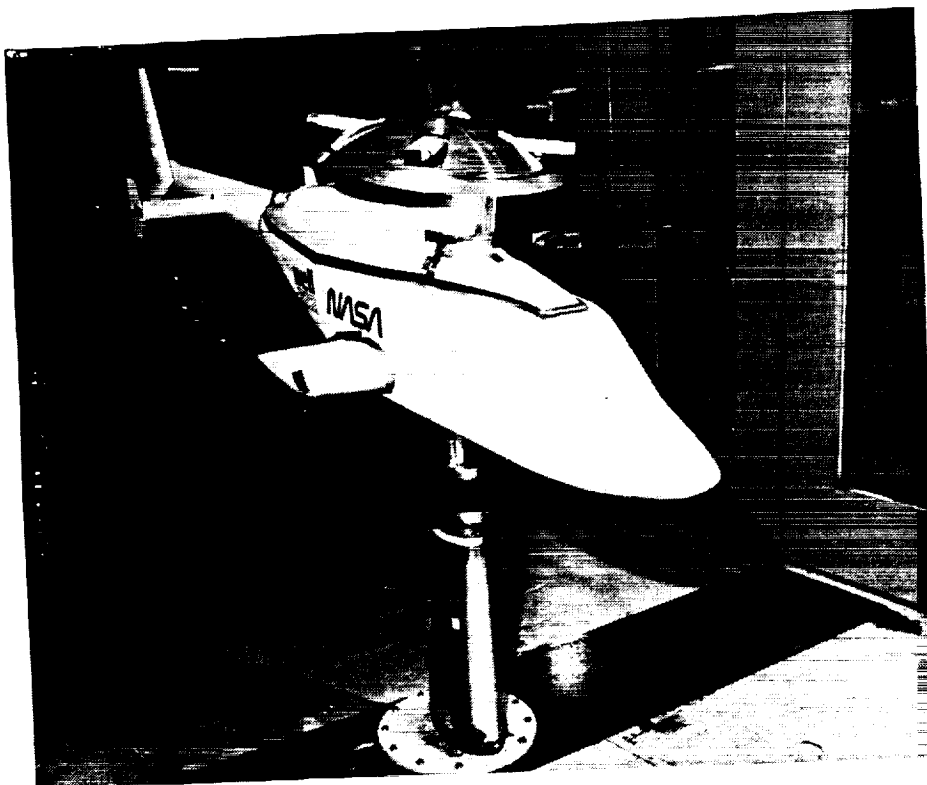


Figure 24. Concluded. (b) front view.

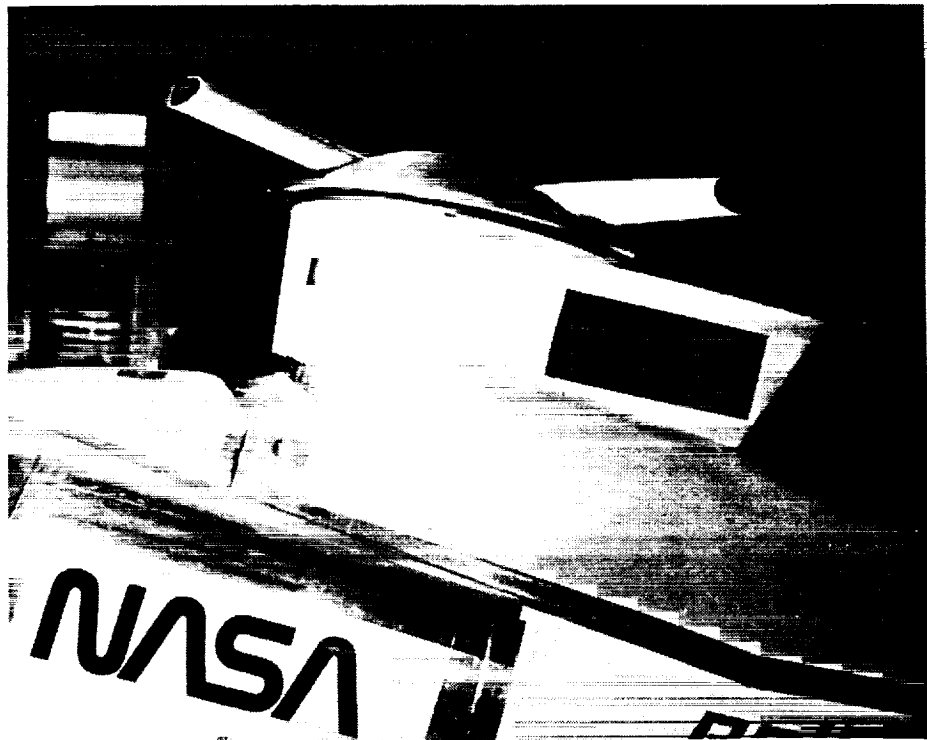


Figure 25. Close-up view of model with Dual Component #2 configuration.

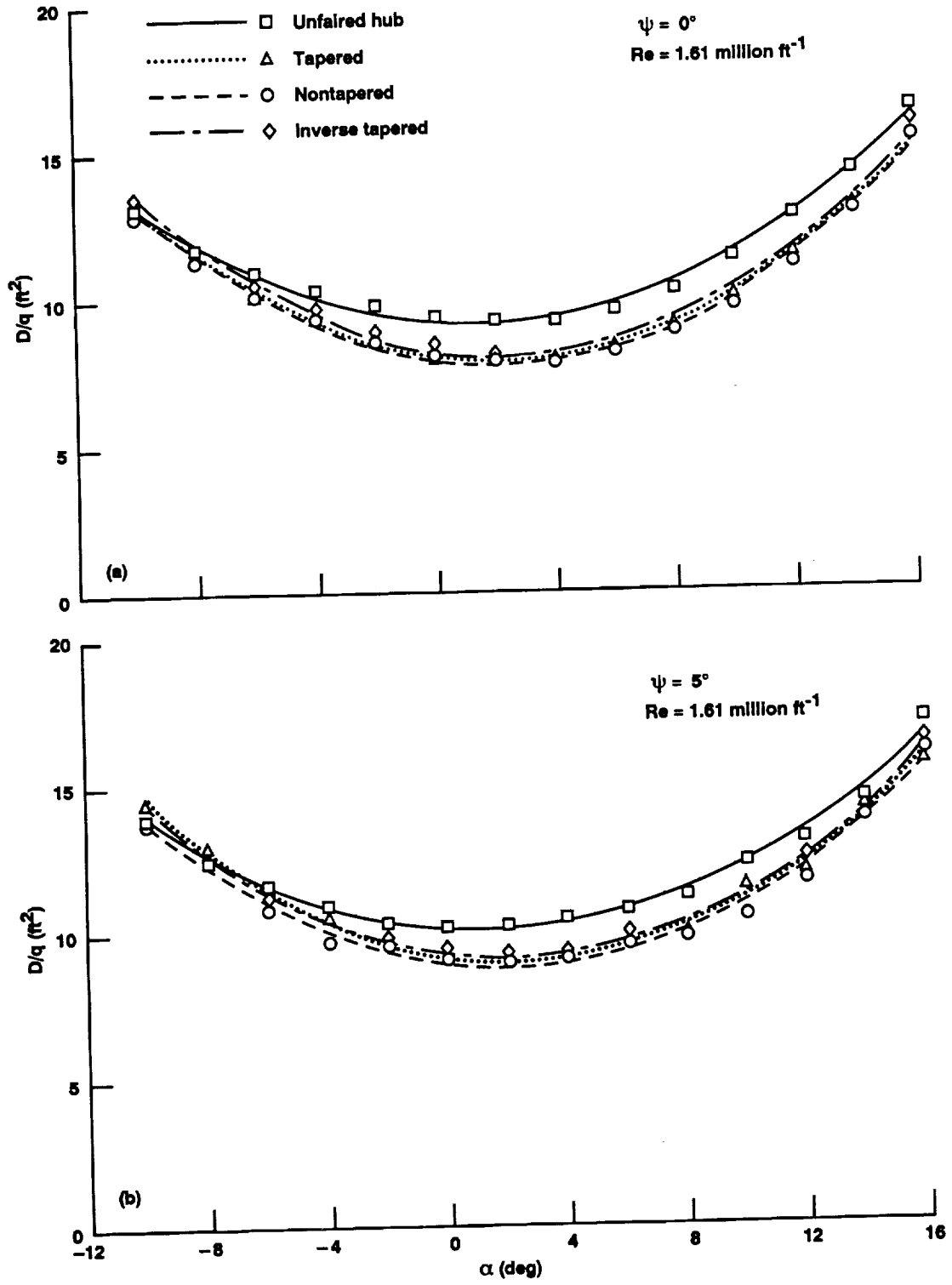


Figure 26. Variation of model drag with α for unfaired hub and pylon fairings. (a) $\psi = 0^\circ$, (b) $\psi = 5^\circ$.

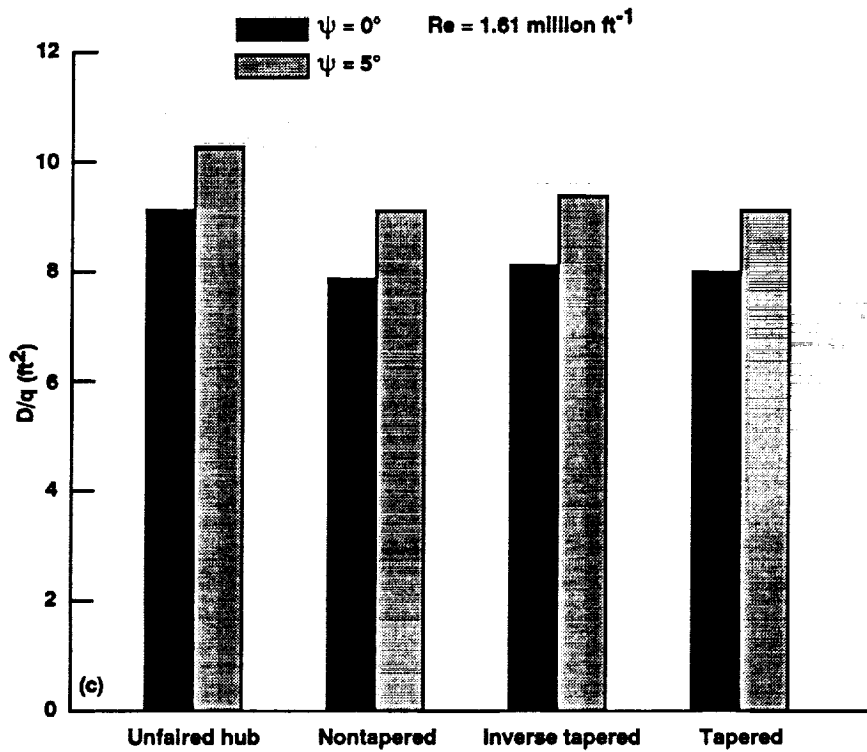


Figure 26. Concluded. (c) minimum drag comparison.

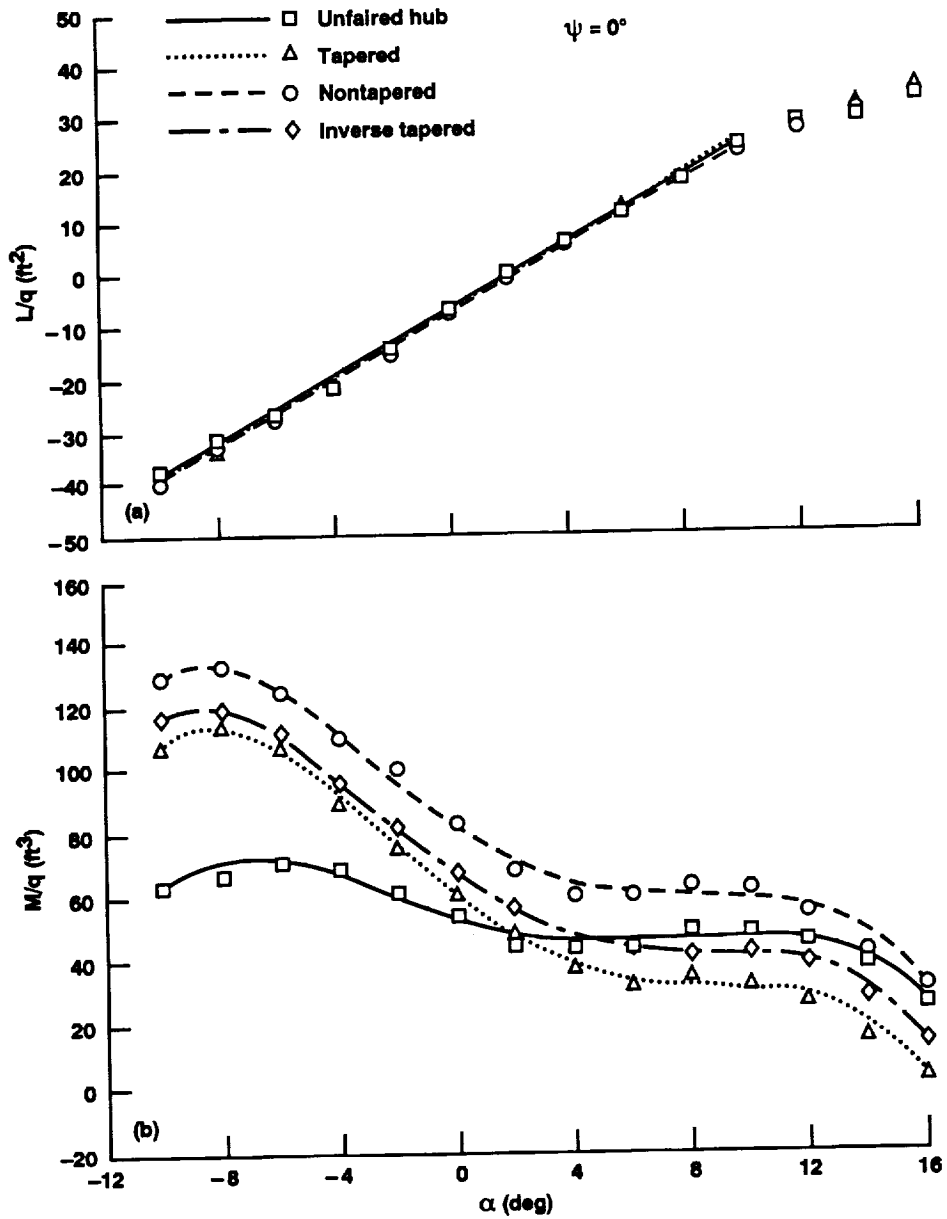


Figure 27. Variation of model lift and pitching moment with α for unfaired hub with pylon fairings at $\psi = 0^\circ$. (a) L/q , (b) M/q .

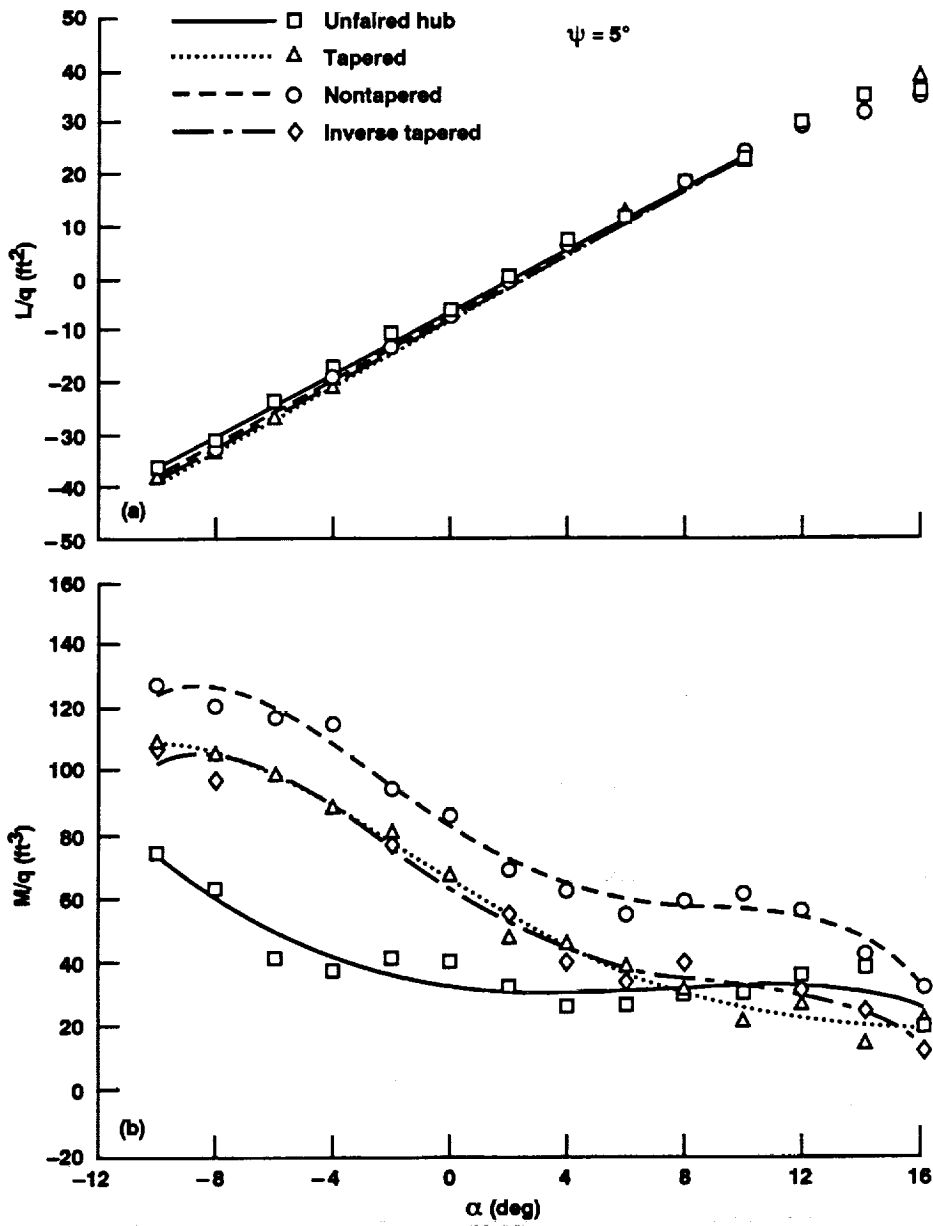


Figure 28. Variation of model lift and pitching moment with α for unfaired hub with pylon fairings at $\psi = 5^\circ$. (a) L/q , (b) M/q .

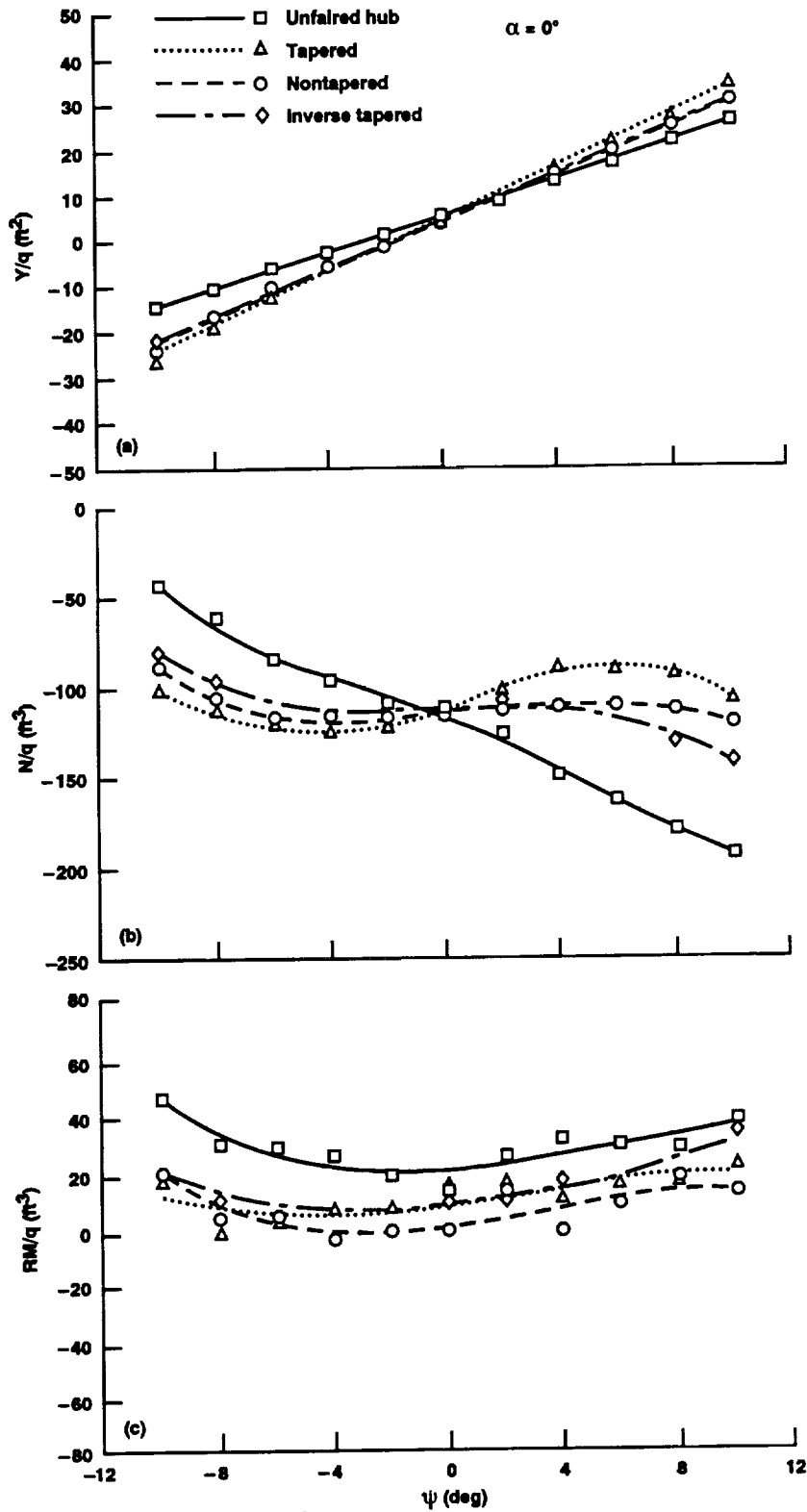


Figure 29. Variation of model side force, yawing moment, and rolling moment for unfaired hub with pylon fairings at $\alpha = 0^\circ$. (a) Y/q , (b) N/q , (c) RM/q .

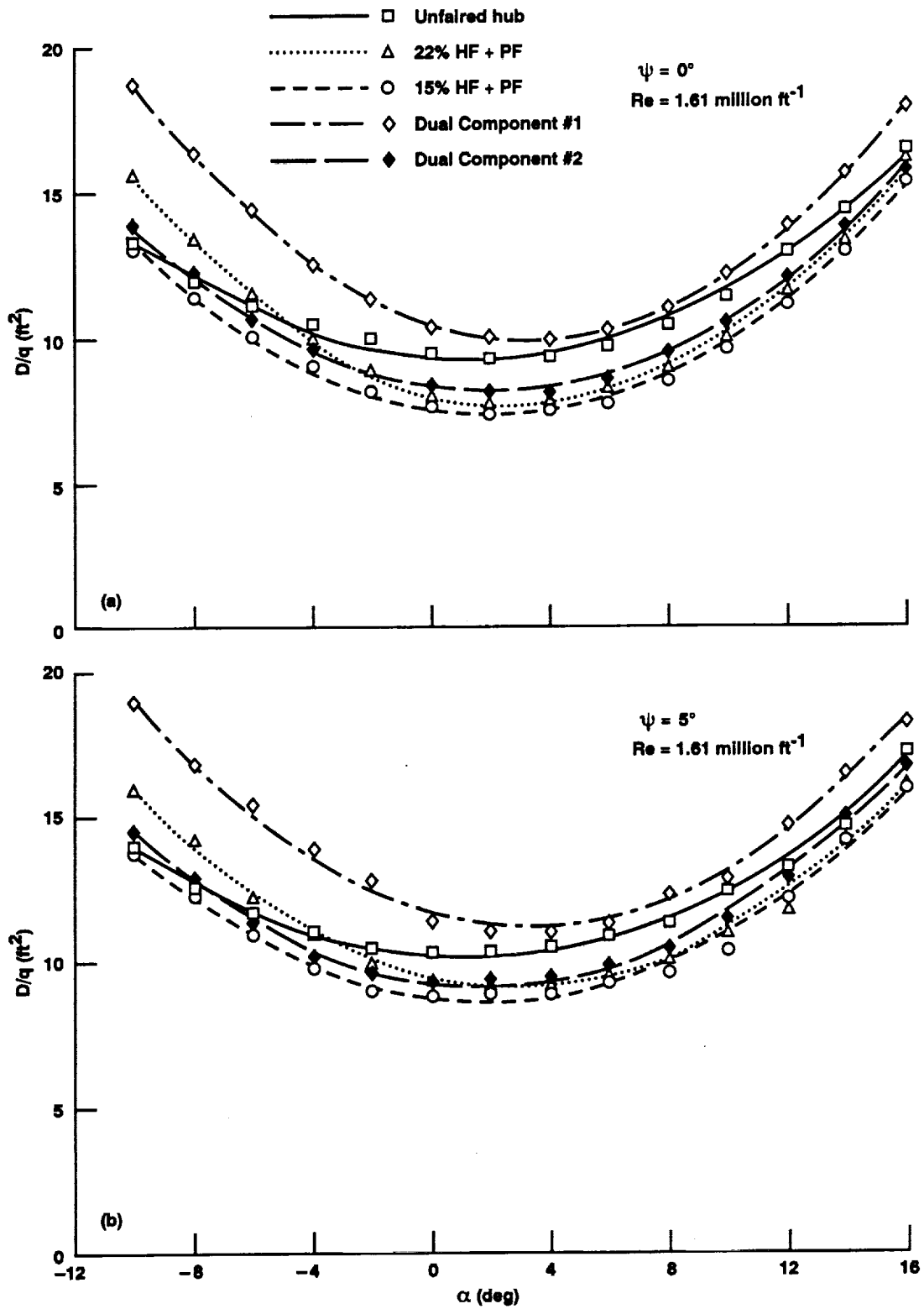


Figure 30. Variation of model drag with α for hub fairings with nontapered pylon fairing. (a) $\psi = 0^\circ$, (b) $\psi = 5^\circ$.

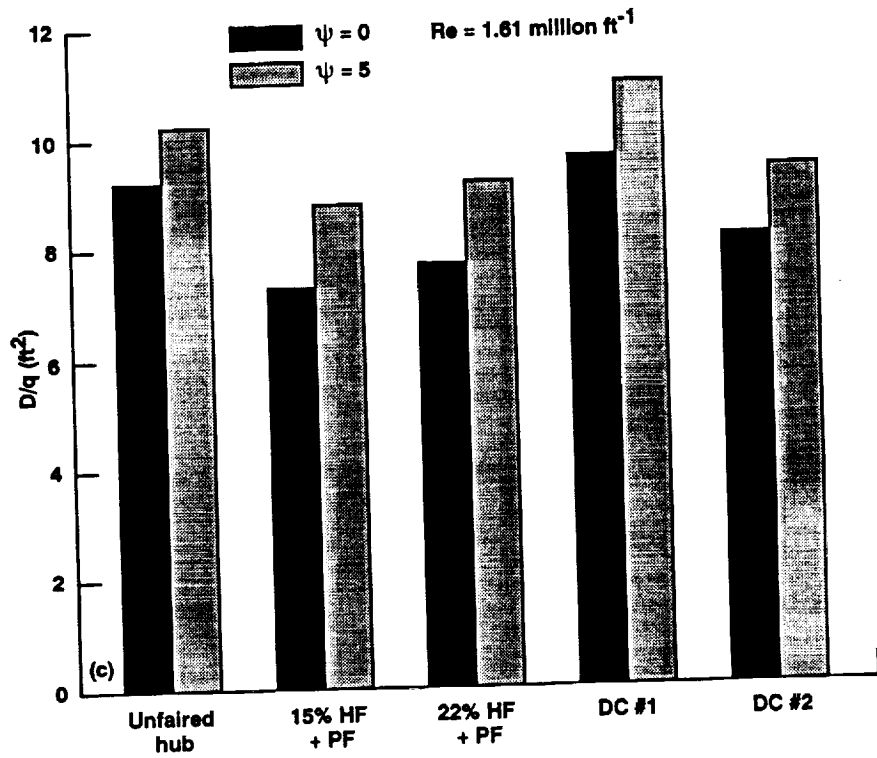


Figure 30. Concluded. (c) minimum drag comparison.

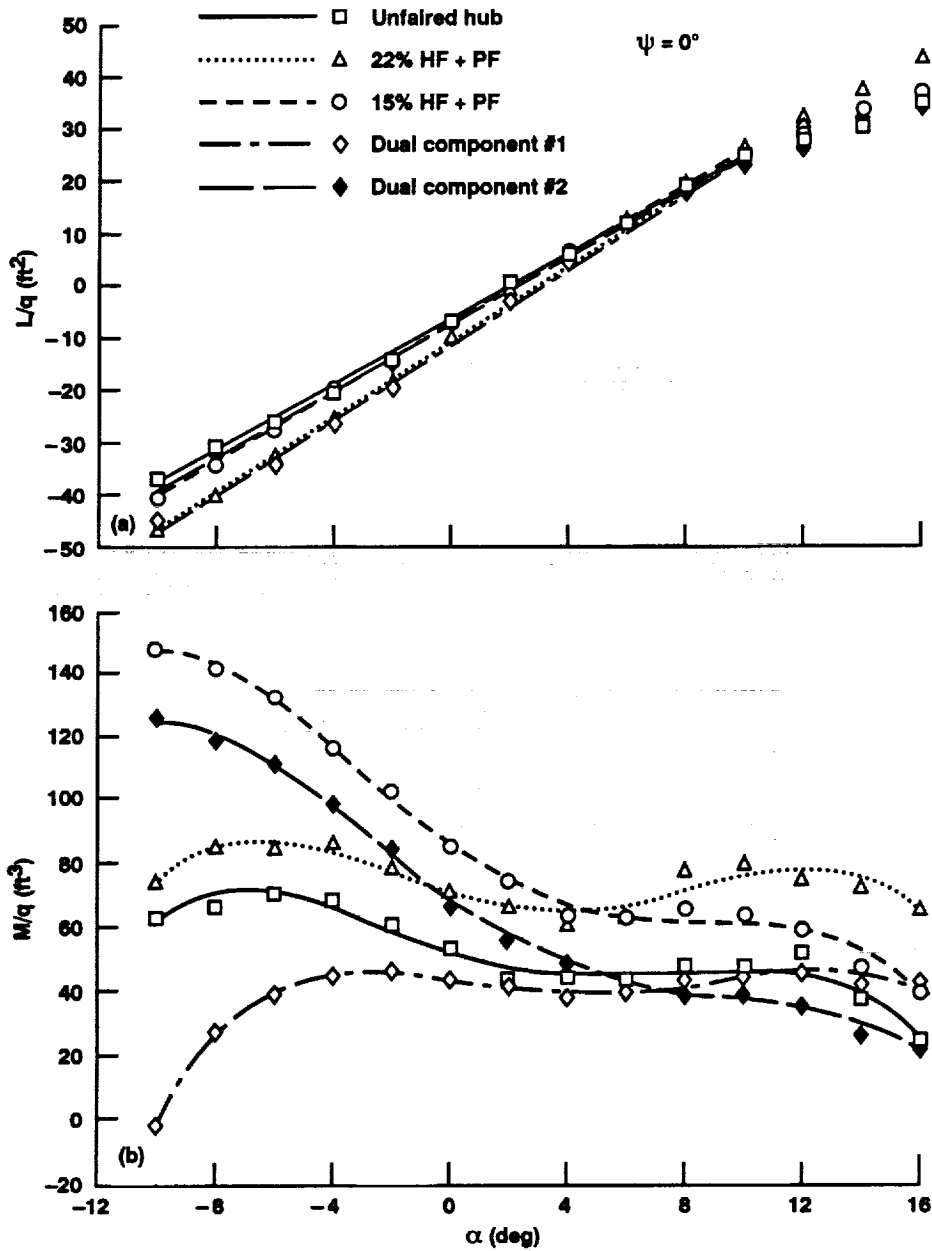


Figure 31. Variation of model lift and pitching moment with α for hub fairings with nontapered pylon fairing at $\psi = 0^\circ$. (a) L/q , (b) M/q .

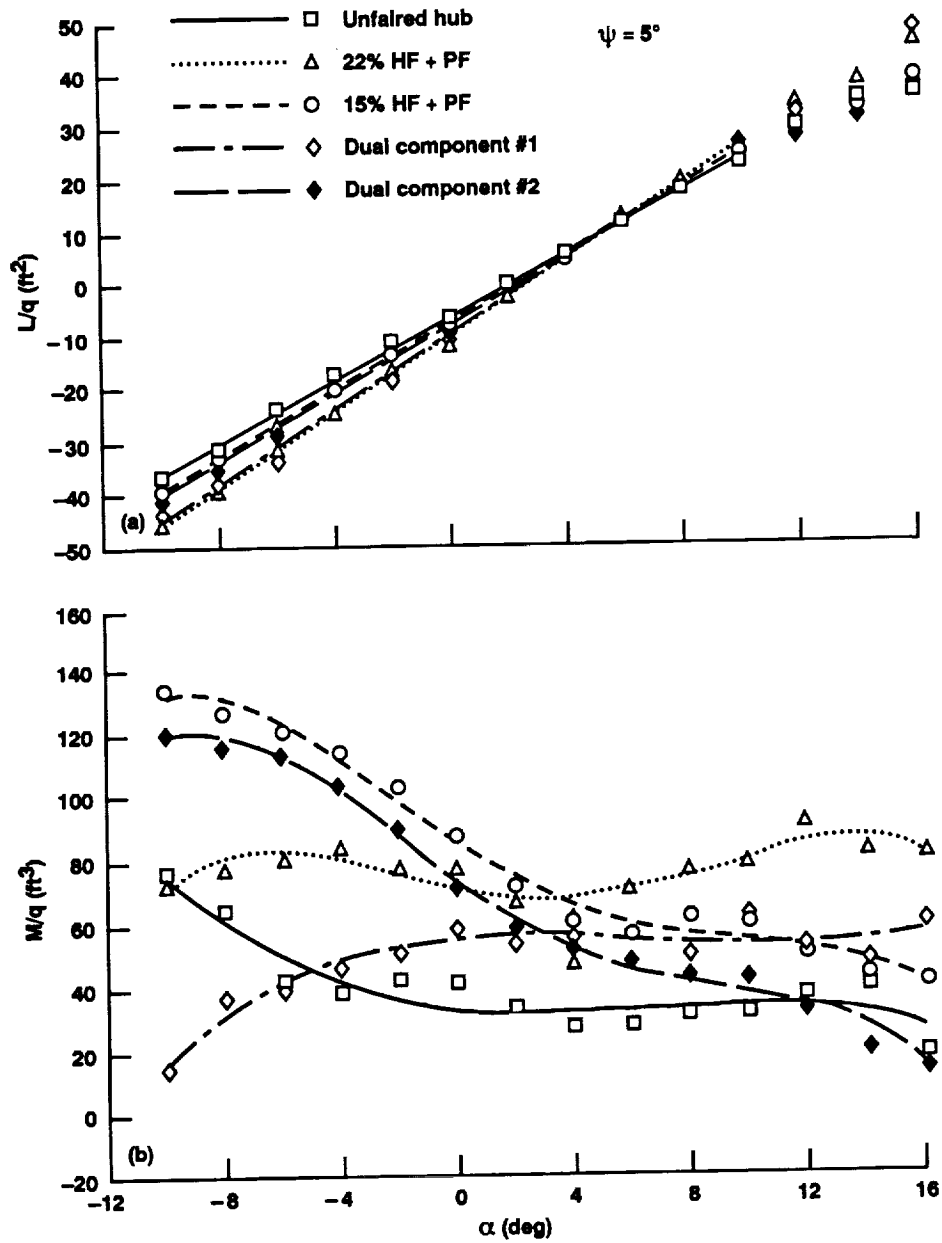


Figure 32. Variation of model lift and pitching moment with α for hub fairings with nontapered pylon fairing at $\psi = 5^\circ$.
 (a) L/q , (b) M/q .

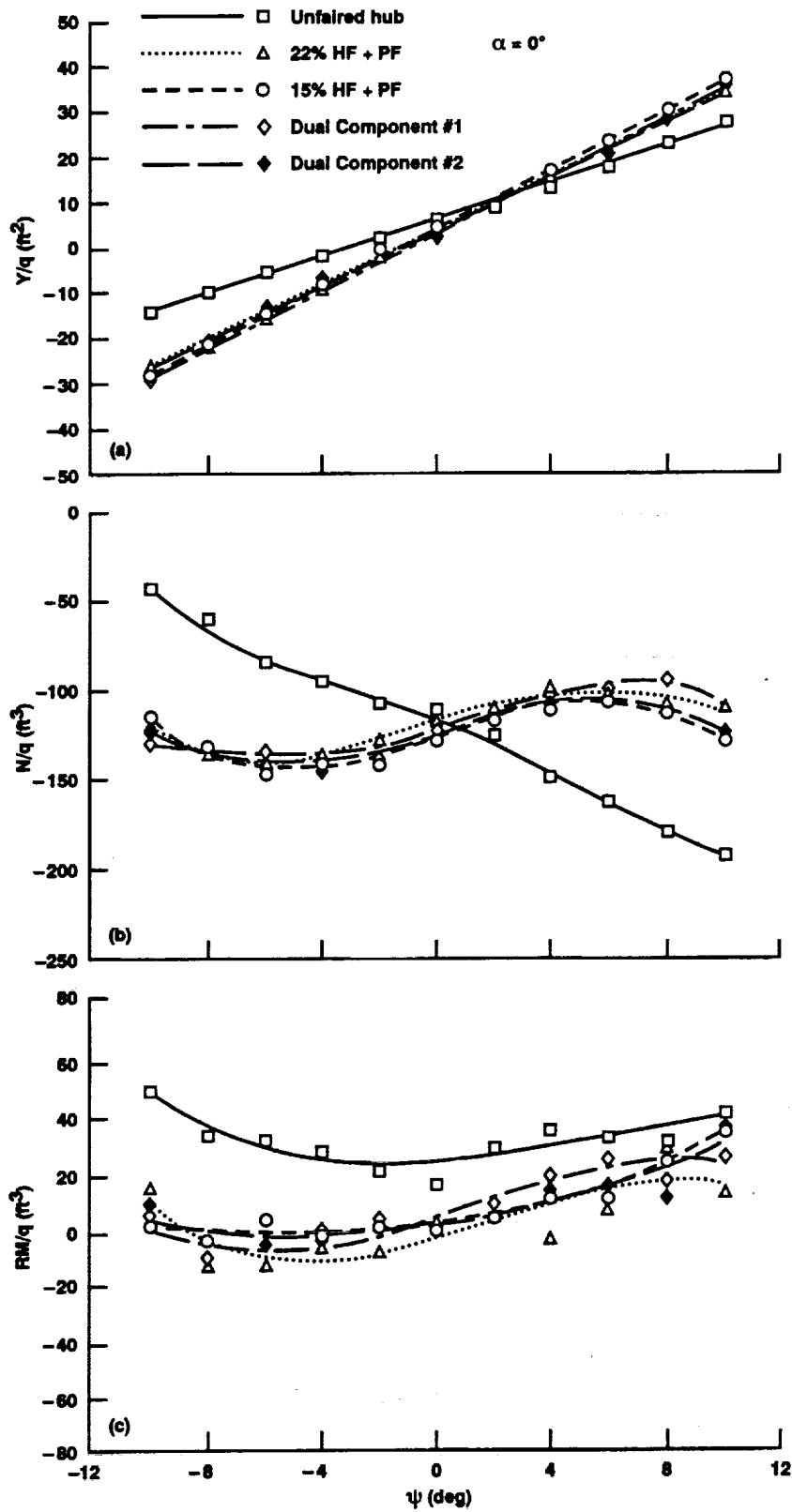


Figure 33. Variation of model side force, yawing moment, and rolling moment for hub fairings with nontapered pylon fairings at $\alpha = 0^\circ$. (a) Y/q , (b) N/q , (c) RM/q .

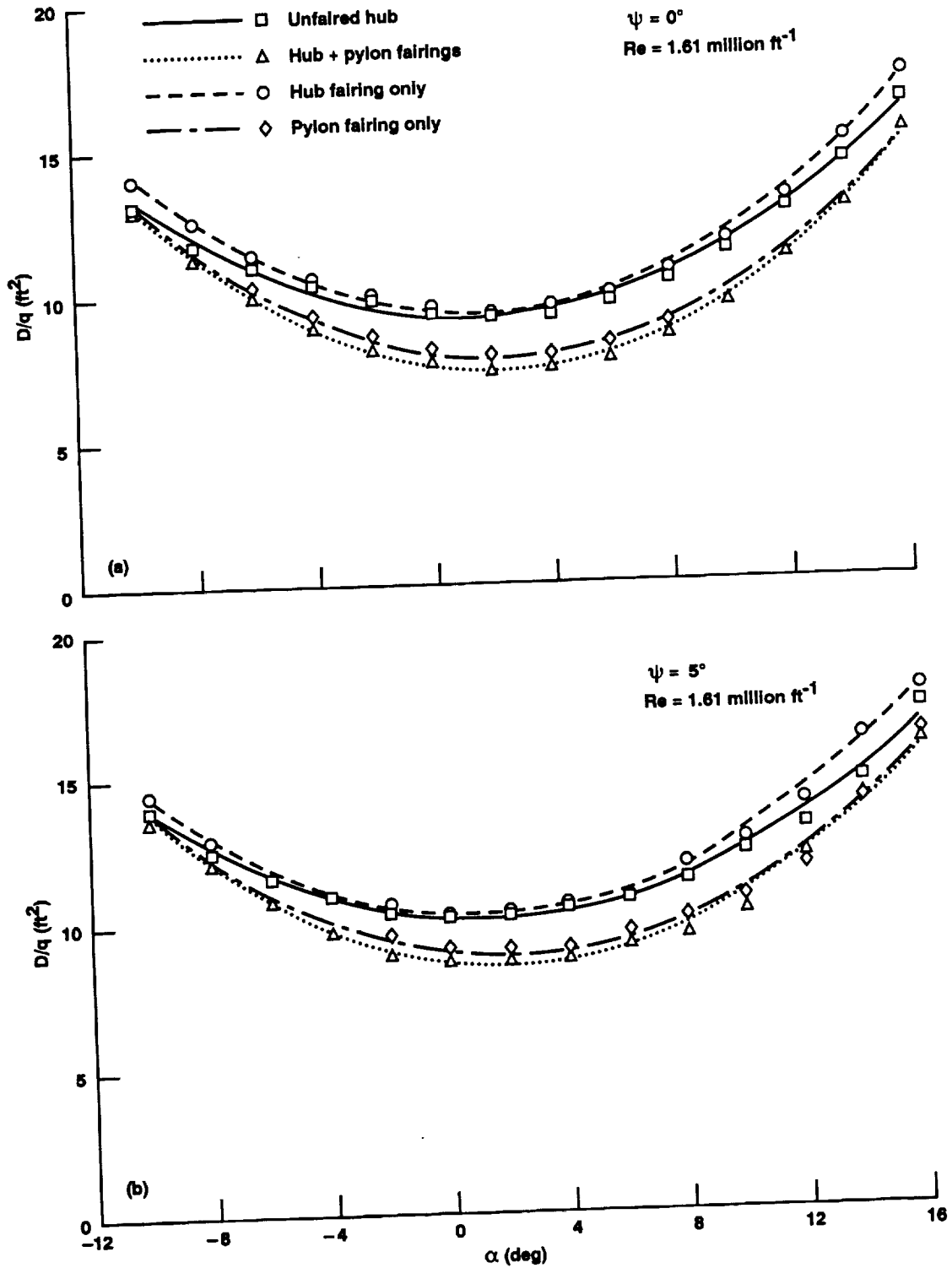


Figure 34. Variation of model drag with α for the 15%/nontapered integrated fairing component buildup sequence. (a) $\psi = 0^\circ$, (b) $\psi = 5^\circ$.

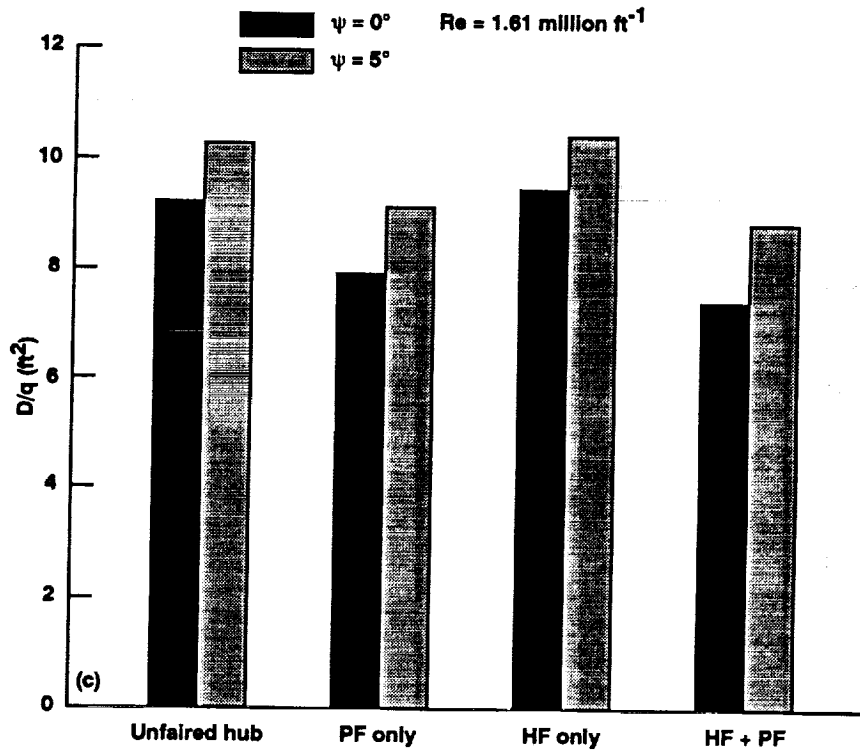


Figure 34. Concluded. (c) minimum drag comparison.

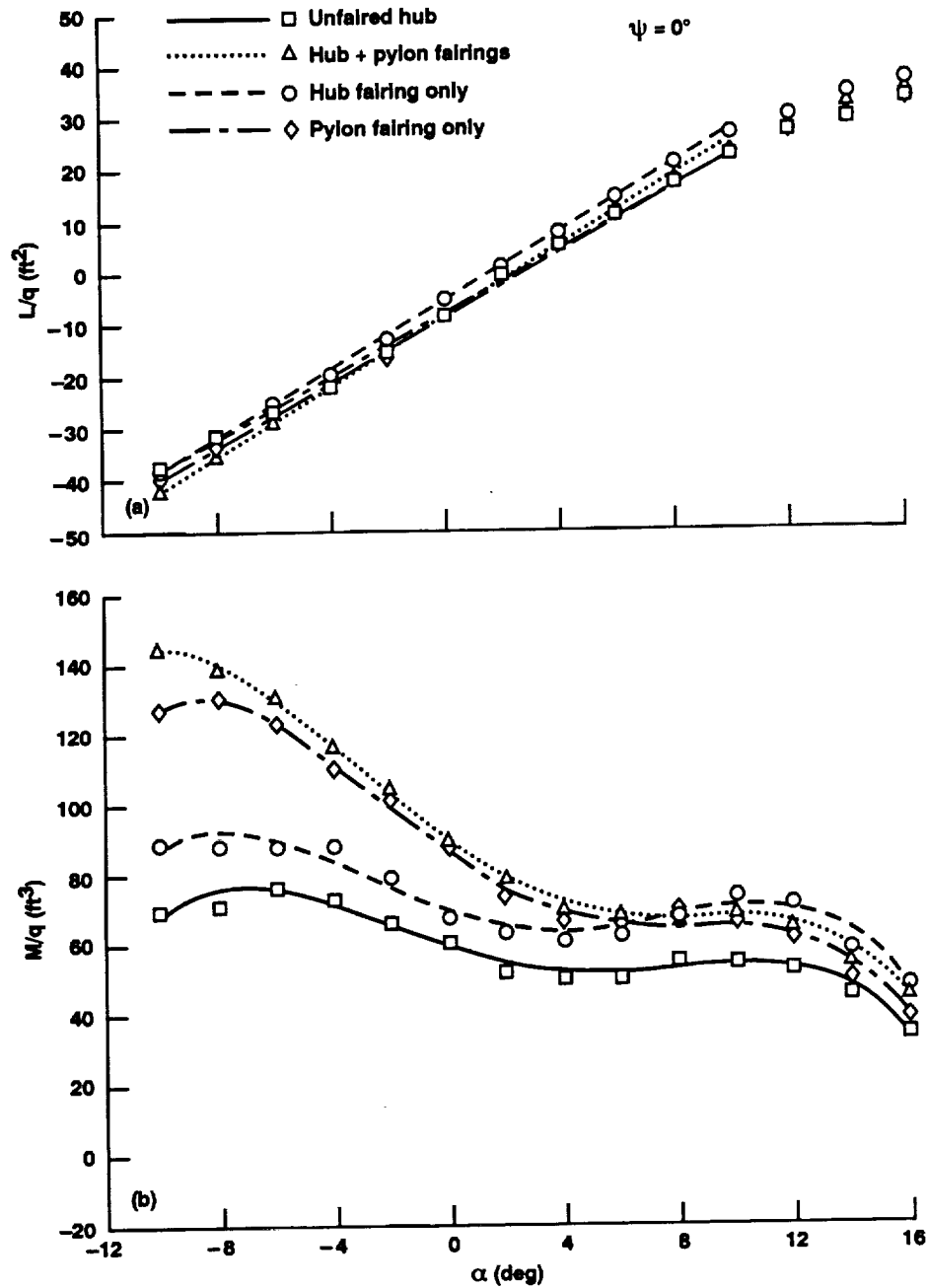


Figure 35. Variation of model lift and pitching moment with α for the 15%/nontapered integrated fairing component buildup sequence at $\psi = 0^\circ$. (a) L/q , (b) M/q .

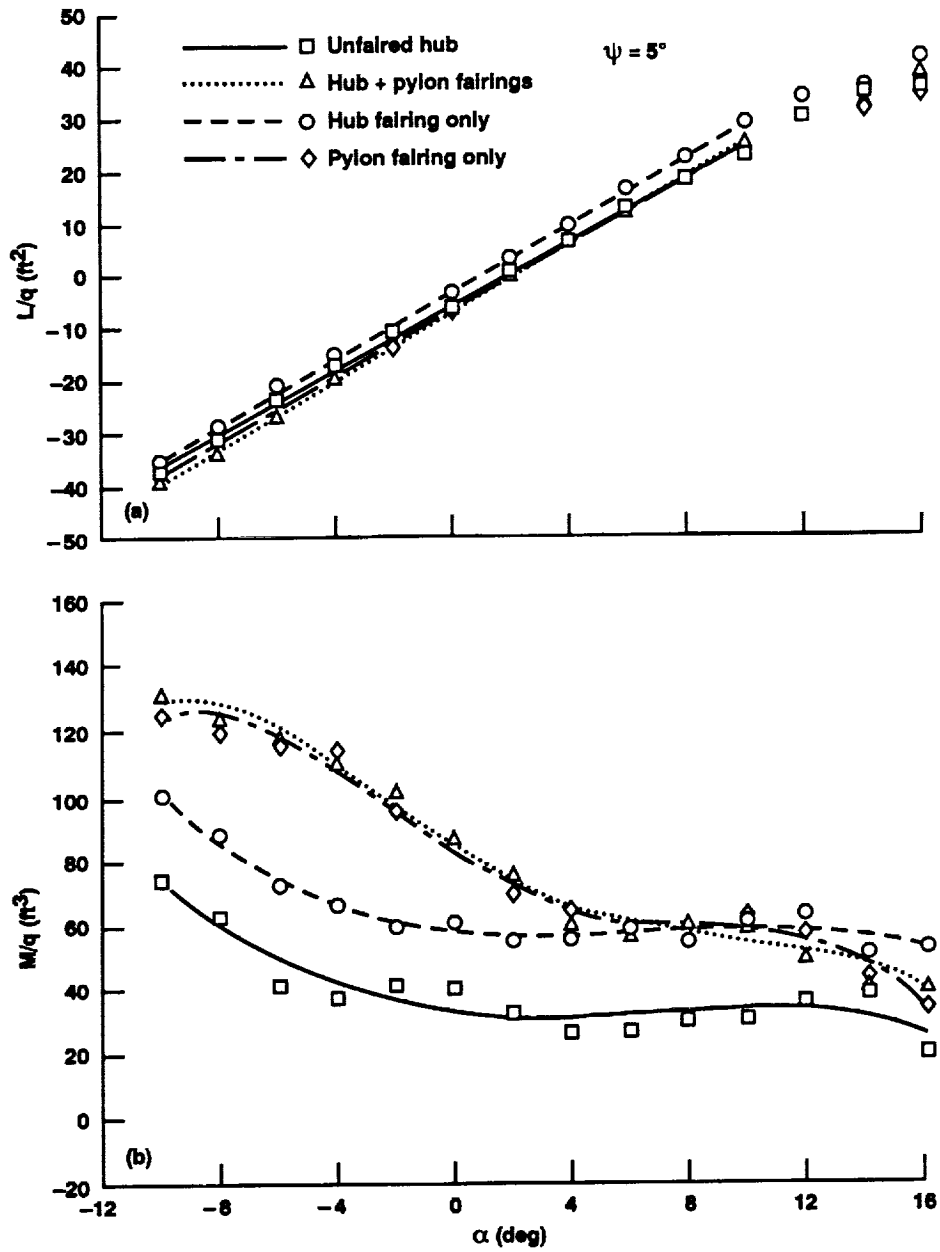


Figure 36. Variation of model lift and pitching moment with α for the 15%/nontapered integrated fairing component buildup sequence at $\psi = 5^\circ$. (a) L/q , (b) M/q .

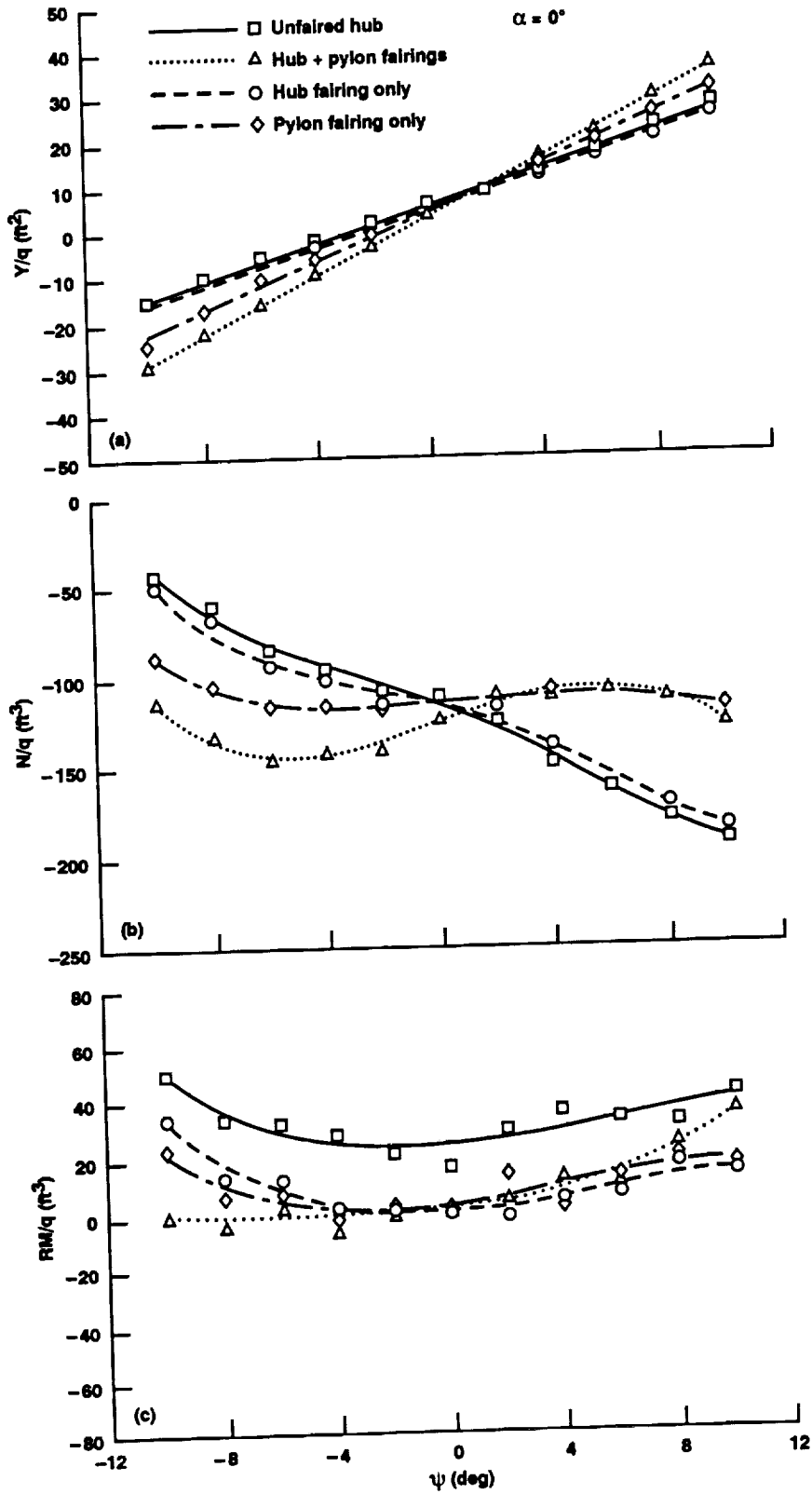


Figure 37. Variation of model side force, yawing moment, and rolling moment for the 15%/nontapered integrated fairing component buildup sequence at $\alpha = 0^\circ$. (a) Y/q , (b) N/q , (c) RM/q .

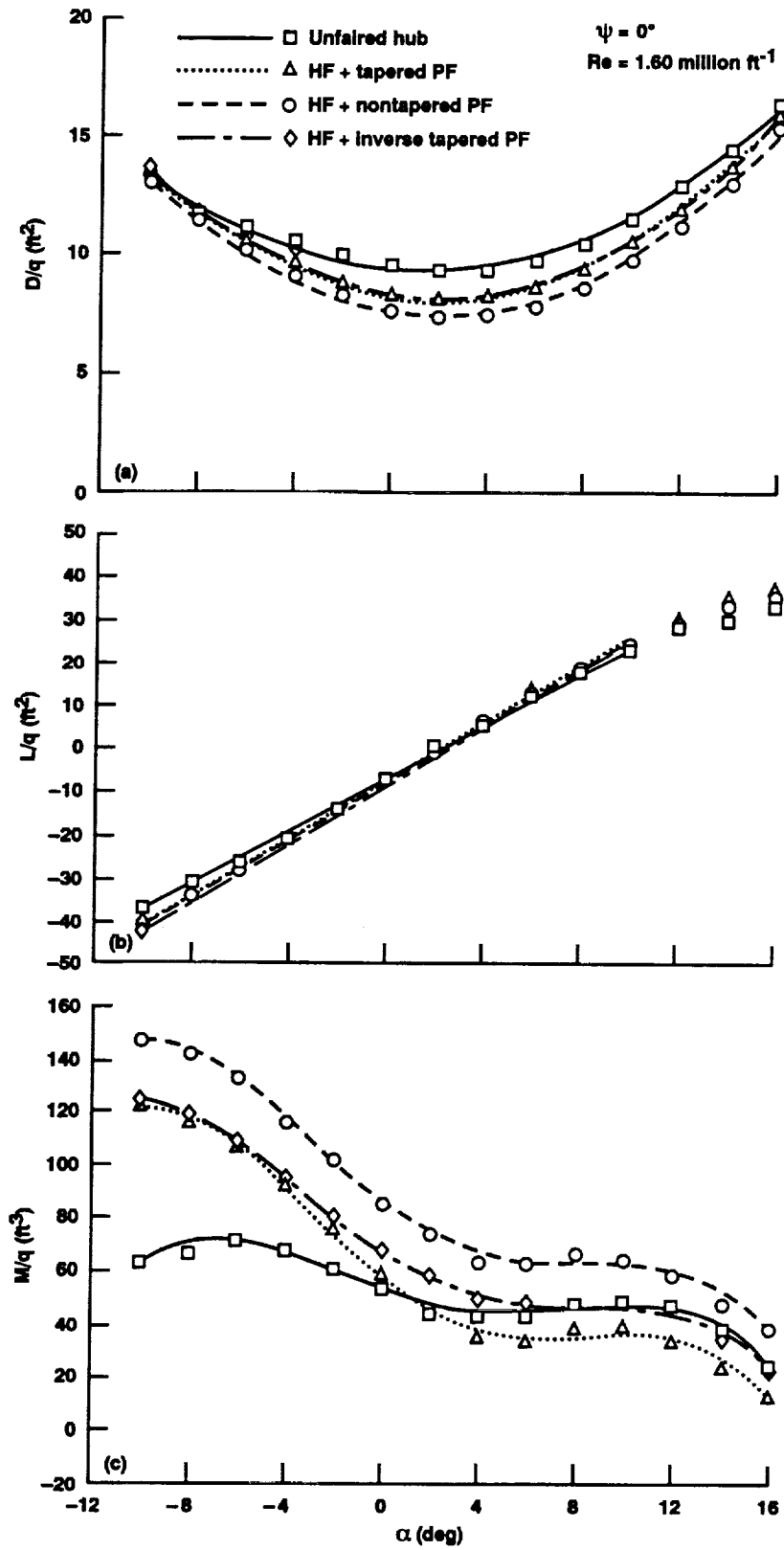


Figure 38. Variation of model drag, lift and pitching moment with α for pylon fairings with 15% hub fairing at $\psi = 0^\circ$. (a) D/q , (b) L/q , (c) M/q .

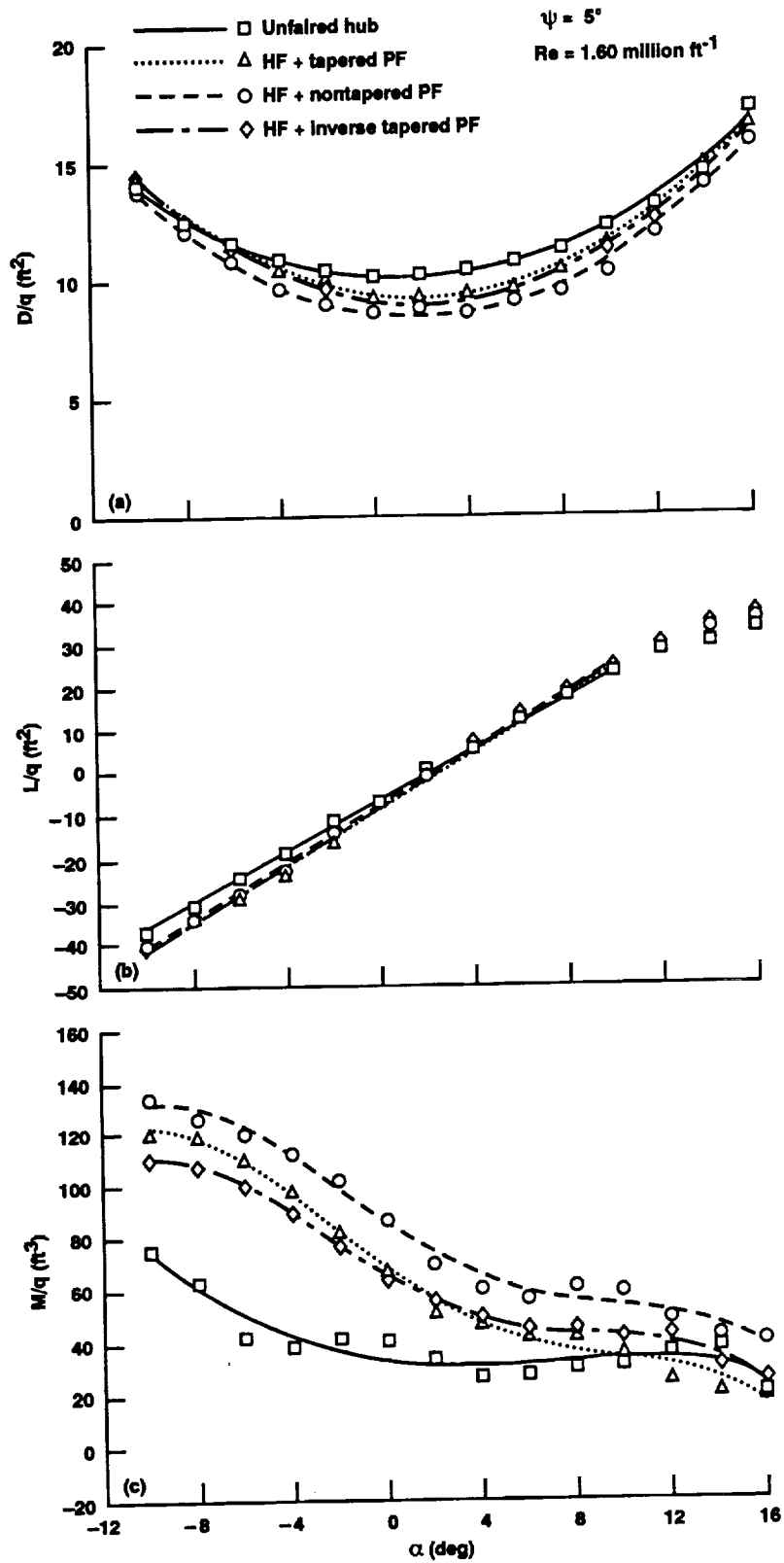


Figure 39. Variation of model drag, lift and pitching moment with α for pylon fairings with 15% hub fairing at $\psi = 5^\circ$. (a) D/q , (b) L/q , (c) M/q .

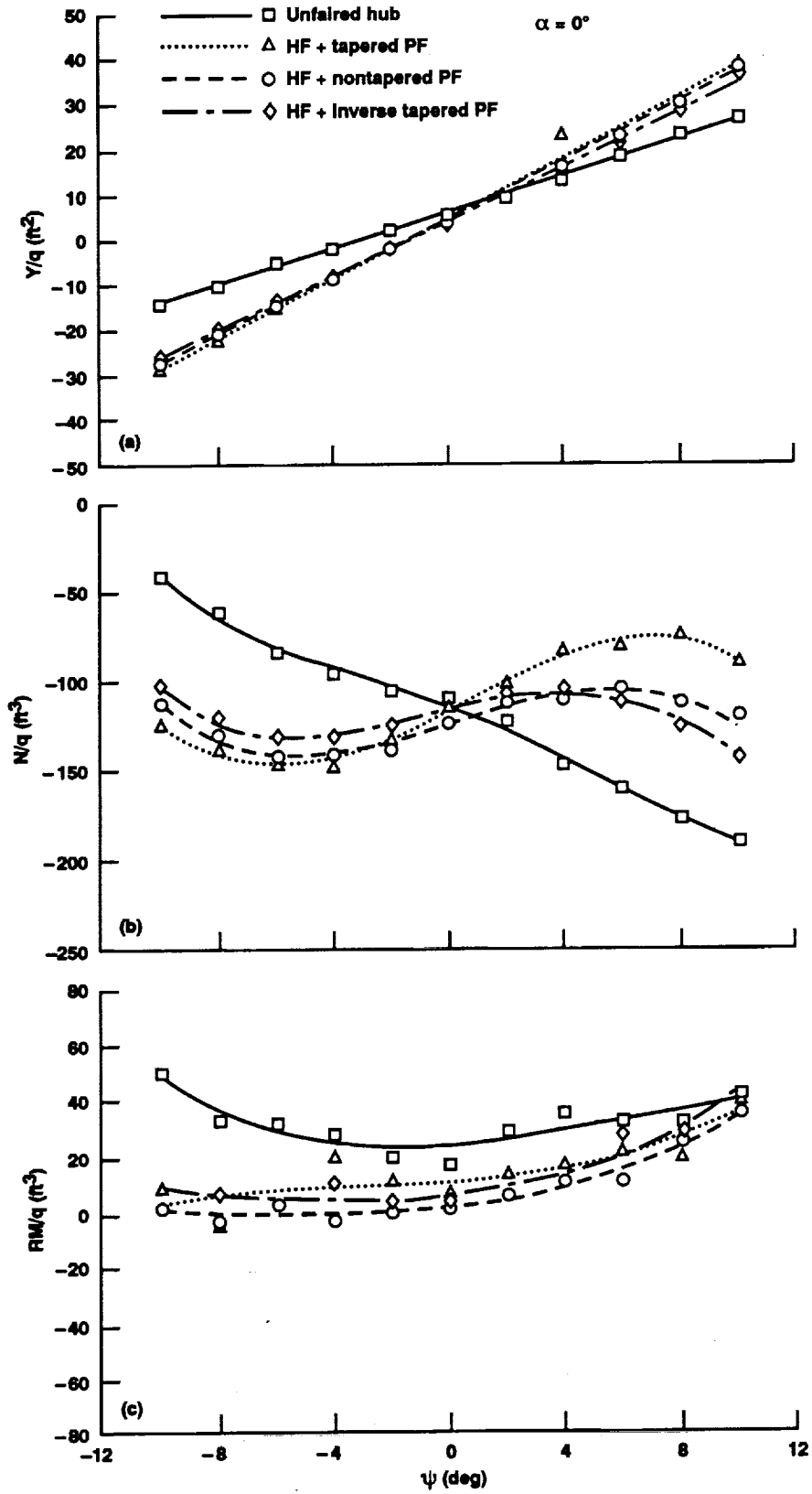


Figure 40. Variation of model side force, yawing moment, and rolling moment for pylon fairings with 15% hub fairing at $\alpha = 0^\circ$. (a) Y/q , (b) N/q , (c) RM/q .

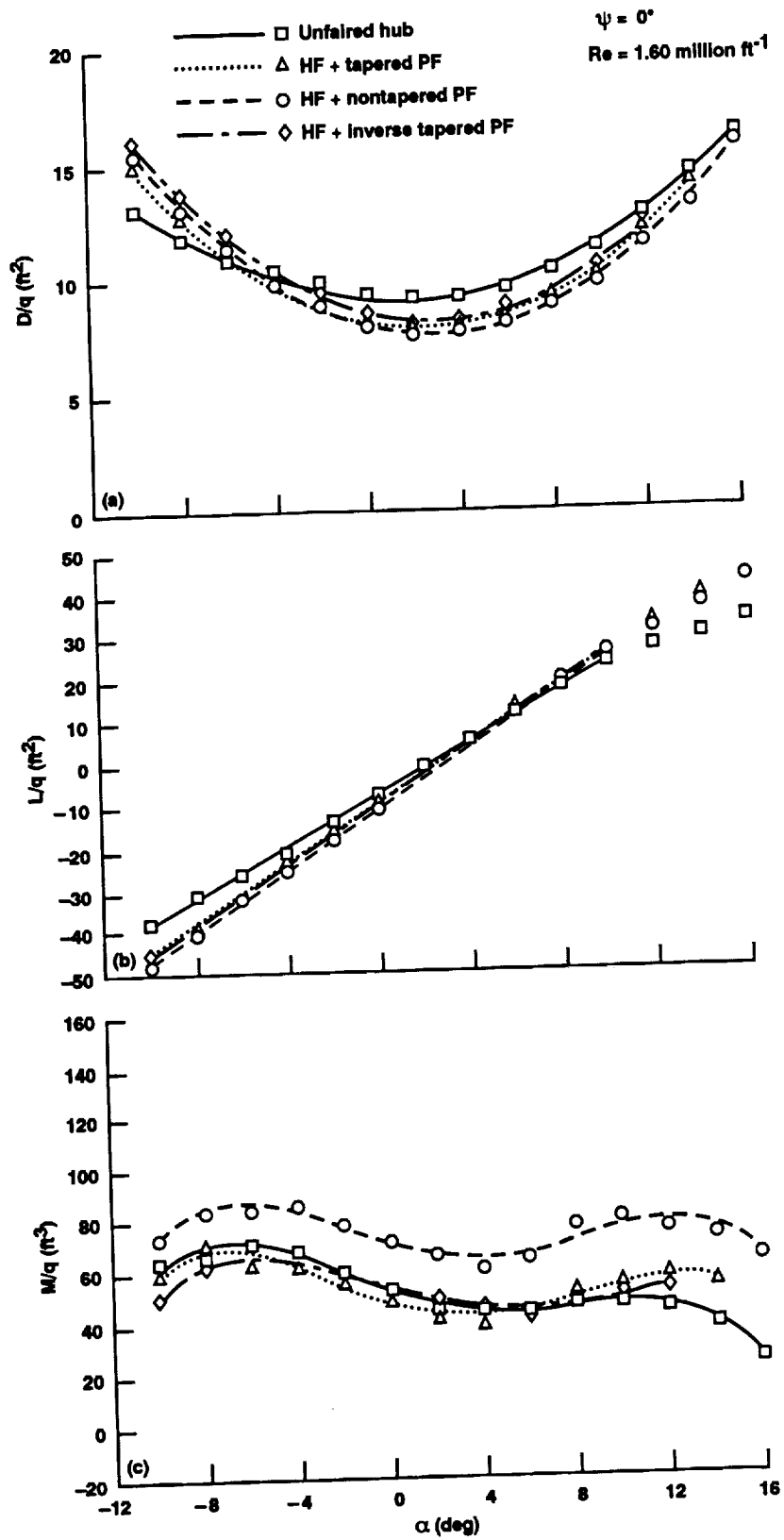


Figure 41. Variation of model drag, lift and pitching moment with α for pylon fairings with 22% hub fairing at $\psi = 0^\circ$.
 (a) D/q , (b) L/q , (c) M/q .

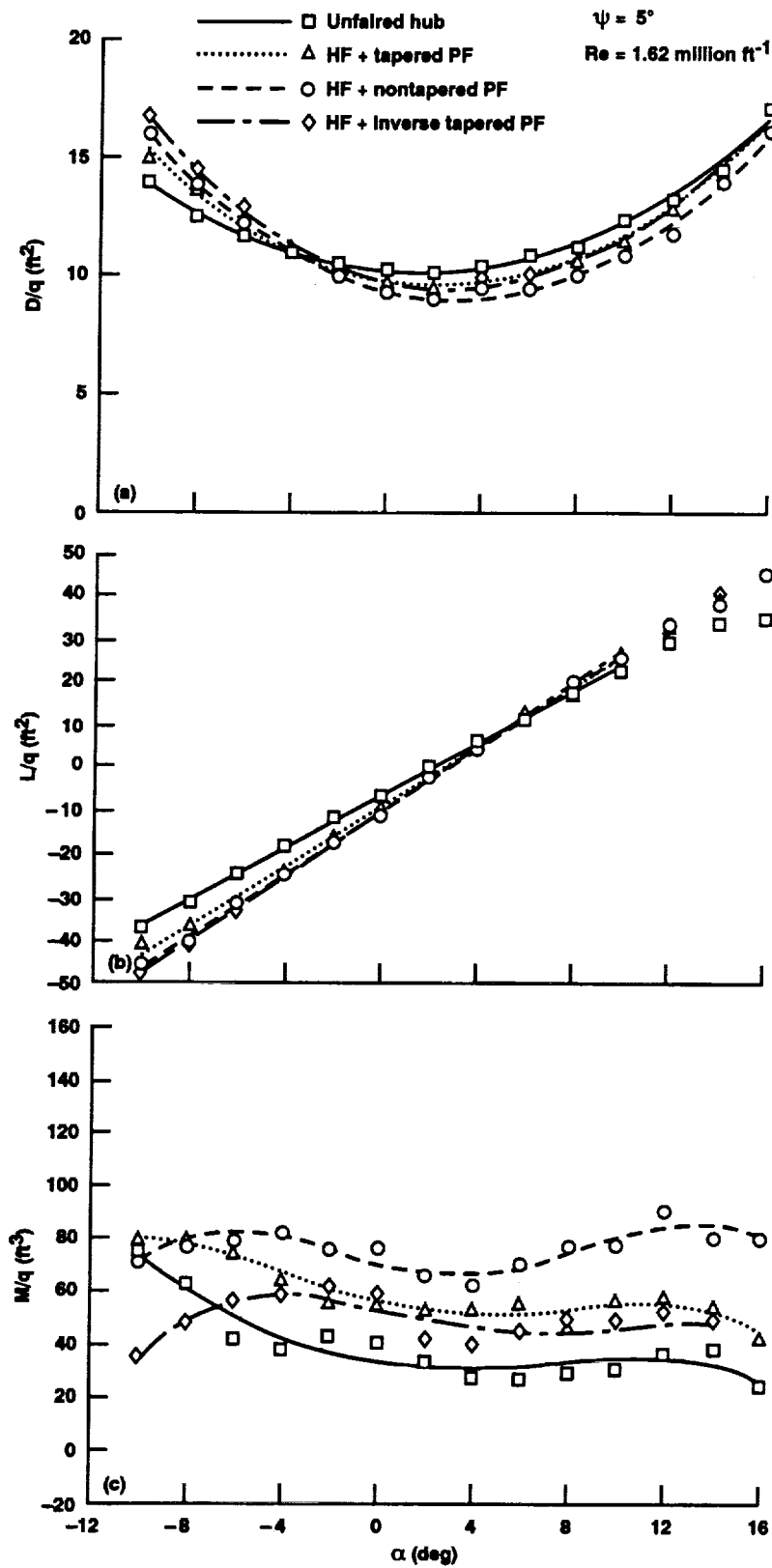


Figure 42. Variation of model drag, lift and pitching moment with α for pylon fairings with 22% hub fairing at $\psi = 5^\circ$. (a) D/q , (b) L/q , (c) M/q .

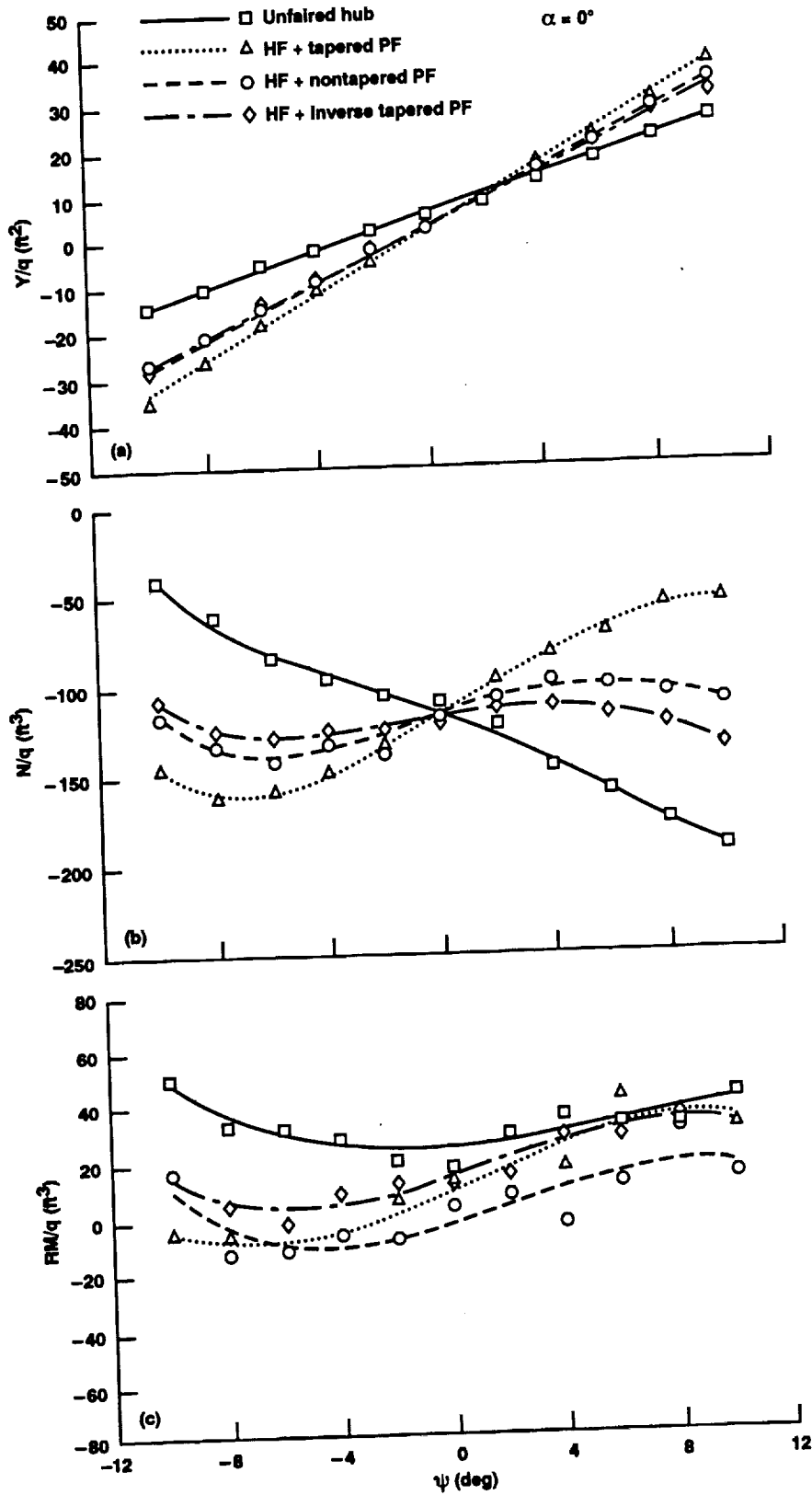


Figure 43. Variation of model side force, yawing moment, and rolling moment for pylon fairings with 22% hub fairing at $\alpha = 0^\circ$. (a) Y/q , (b) N/q , (c) RM/q .

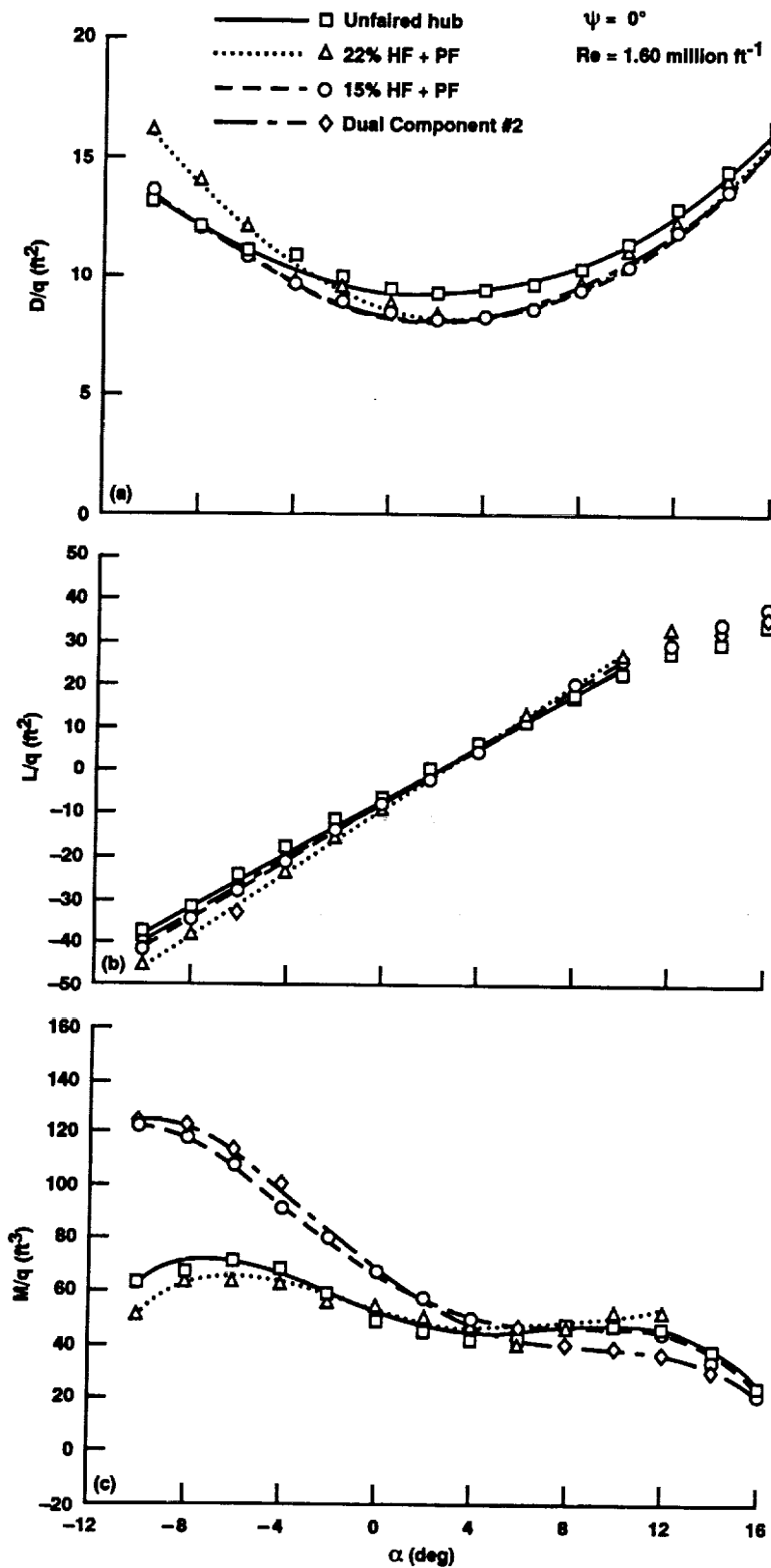


Figure 44. Variation of model drag, lift and pitching moment with α for hub fairings with inverse tapered pylon fairing at $\psi = 0^\circ$. (a) D/q , (b) L/q , (c) M/q .

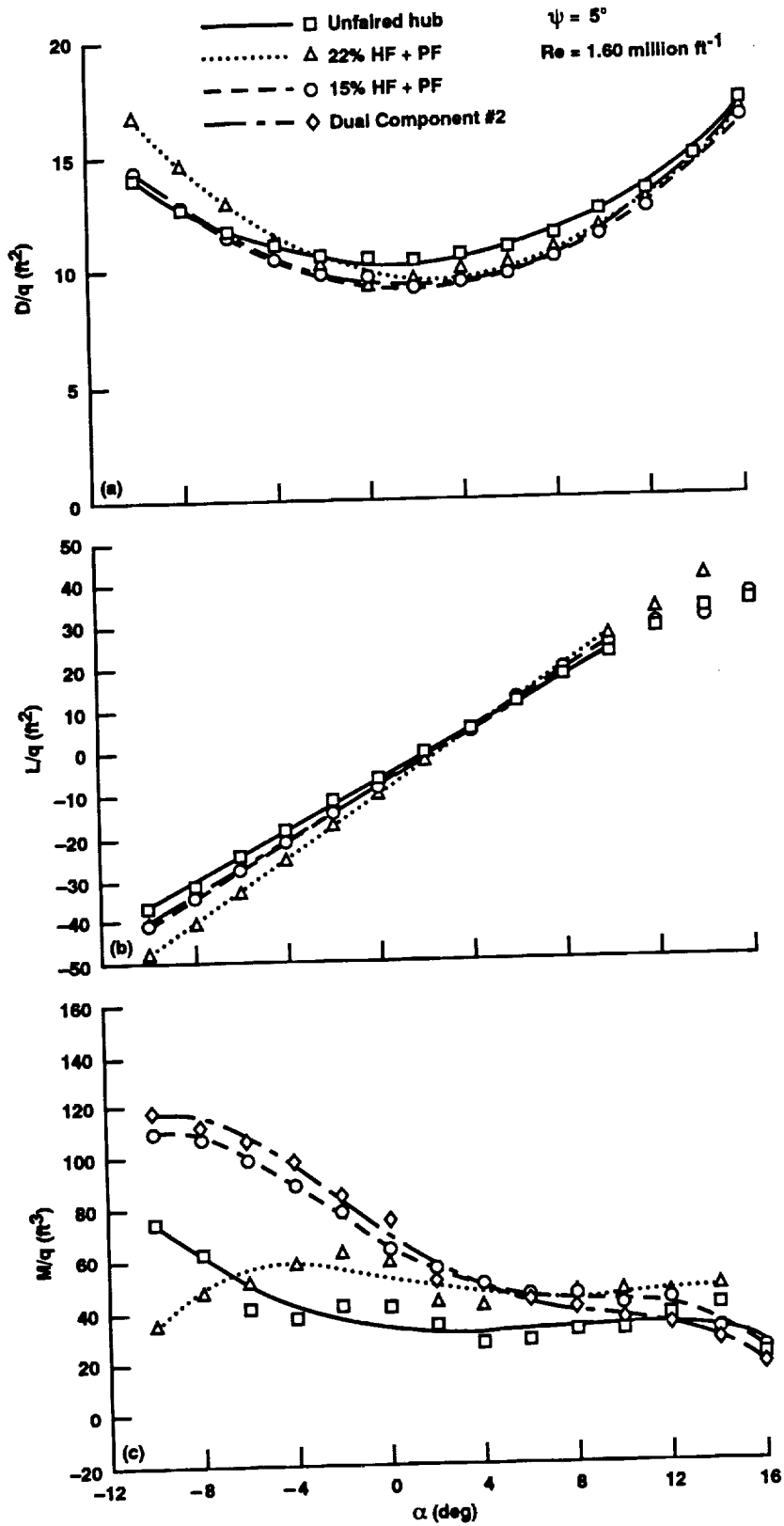


Figure 45. Variation of model drag, lift and pitching moment with α for hub fairings with inverse tapered pylon fairing at $\psi = 5^\circ$. (a) D/q , (b) L/q , (c) M/q .

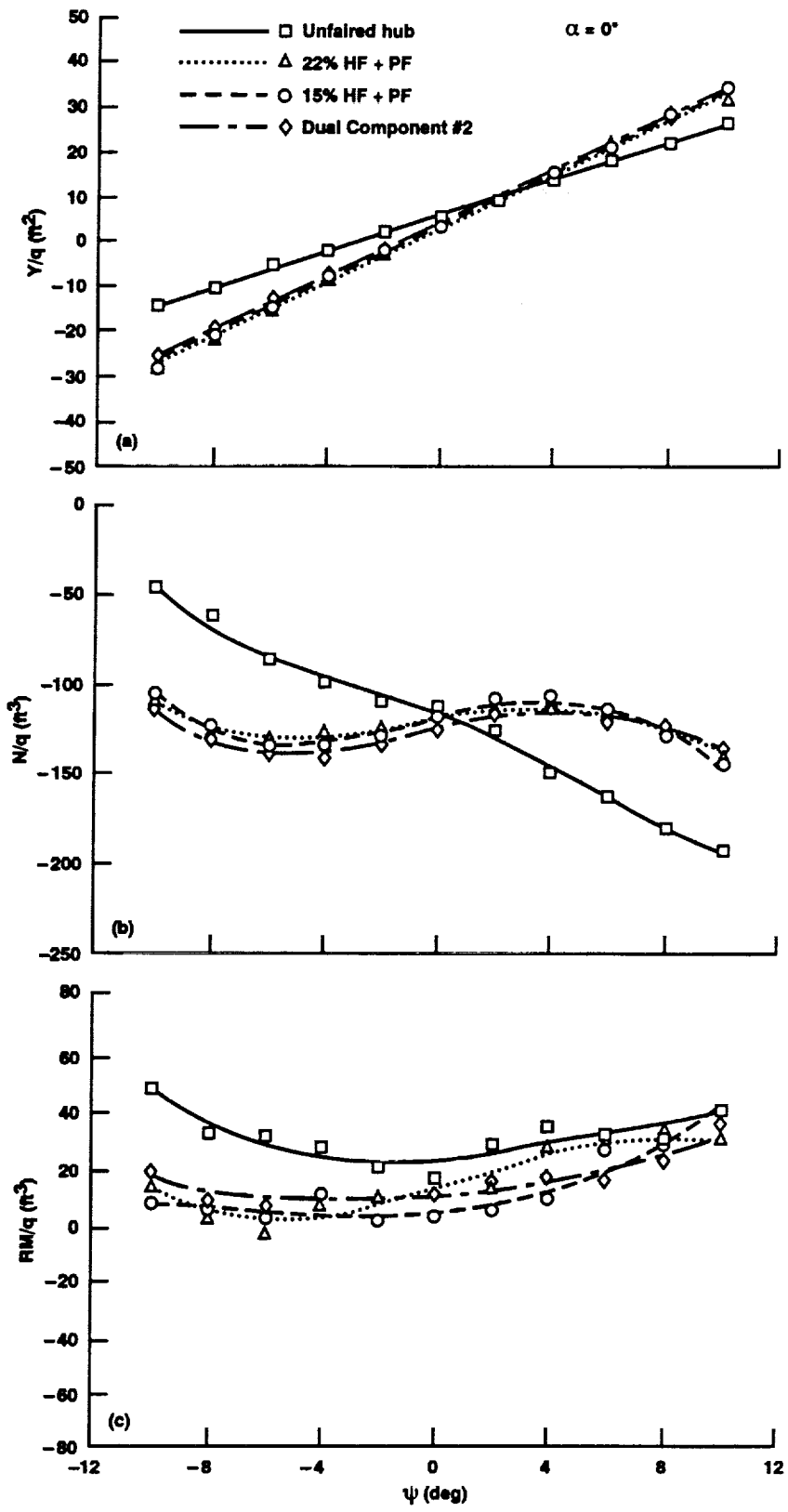


Figure 46. Variation of model side force, yawing moment, and rolling moment for hub fairings with inverse tapered pylon fairing at $\alpha = 0^\circ$. (a) Y/q , (b) N/q , (c) RM/q .

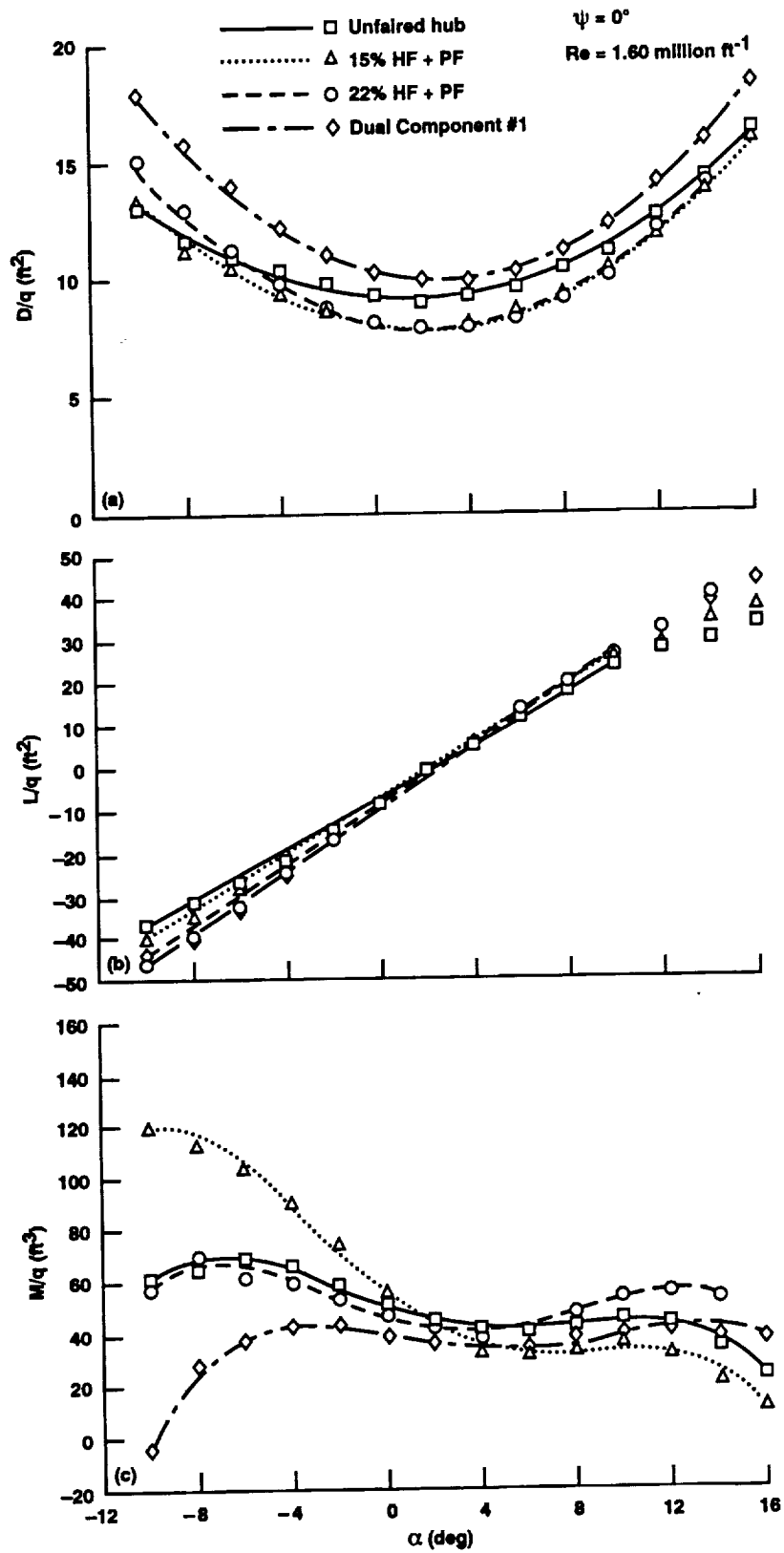


Figure 47. Variation of model drag, lift and pitching moment with α for hub fairings with tapered pylon fairing at $\psi = 0^\circ$.
 (a) D/q , (b) L/q , (c) M/q .

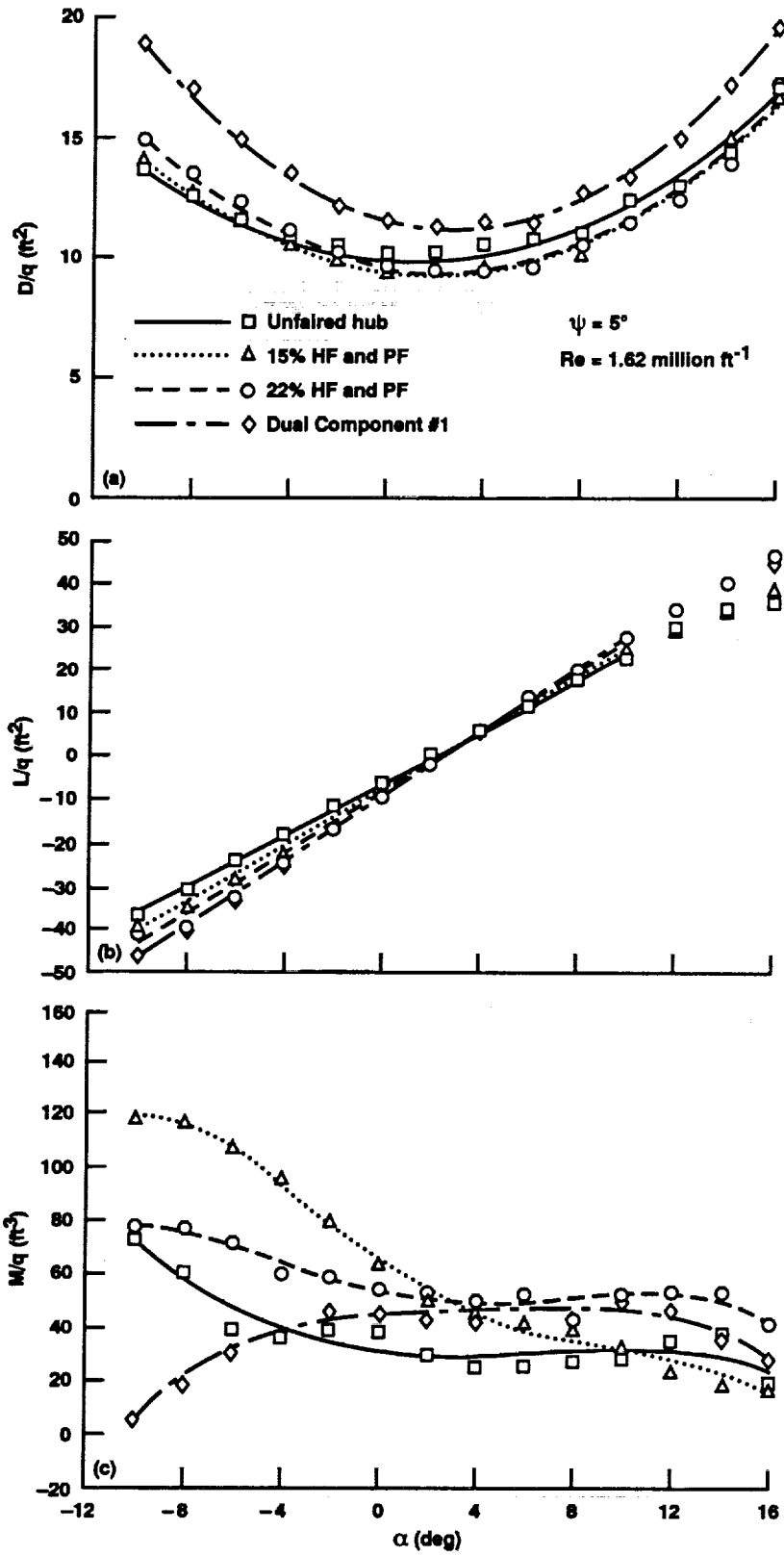


Figure 48. Variation of model drag, lift and pitching moment with α for hub fairings with tapered pylon fairing at $\psi = 5^\circ$. (a) D/q , (b) L/q , (c) M/q .

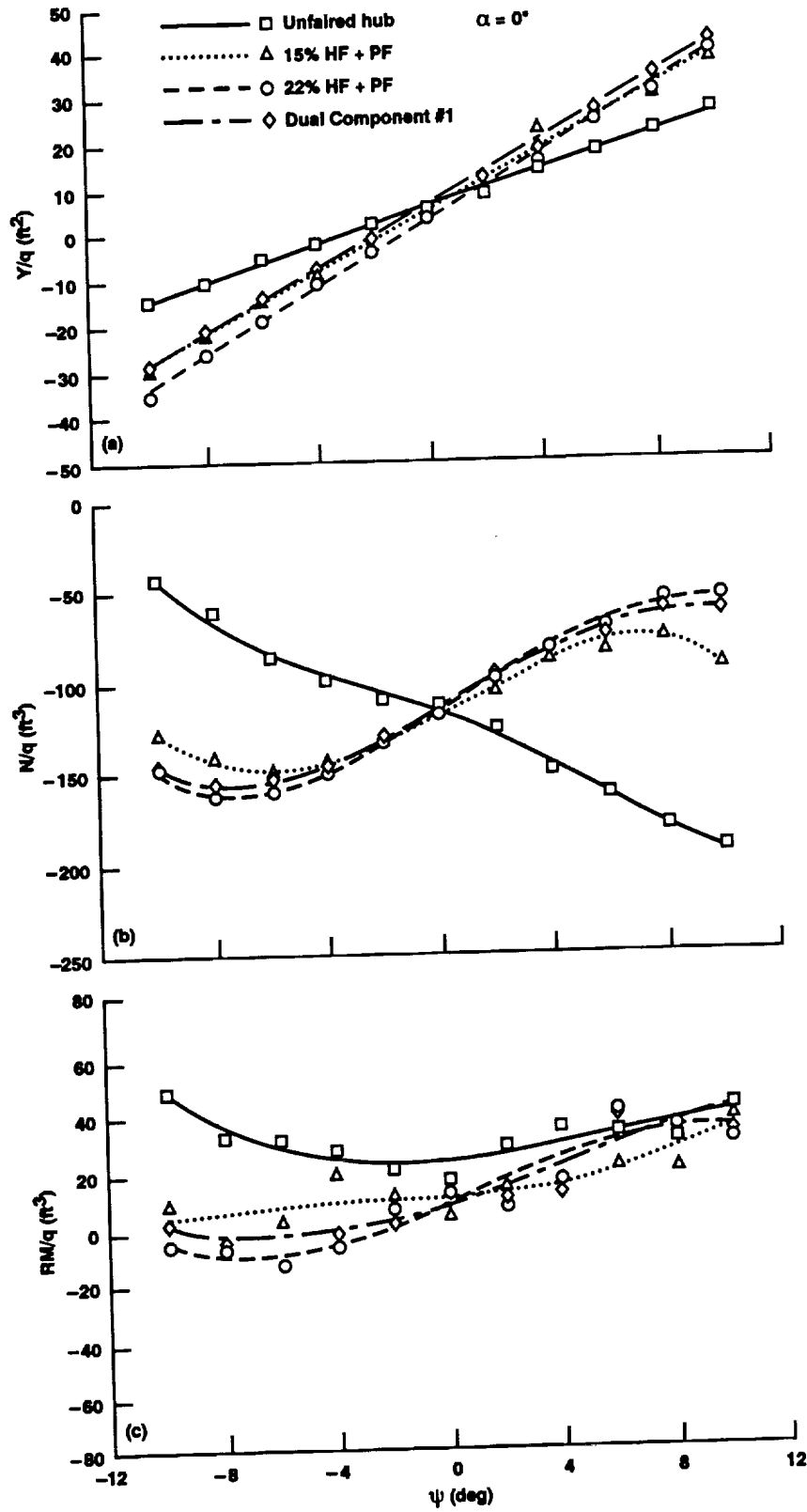


Figure 49. Variation of model side force, yawing moment, and rolling moment for hub fairings with tapered pylon fairing at $\alpha = 0^\circ$. (a) Y/q , (b) N/q , (c) RM/q .

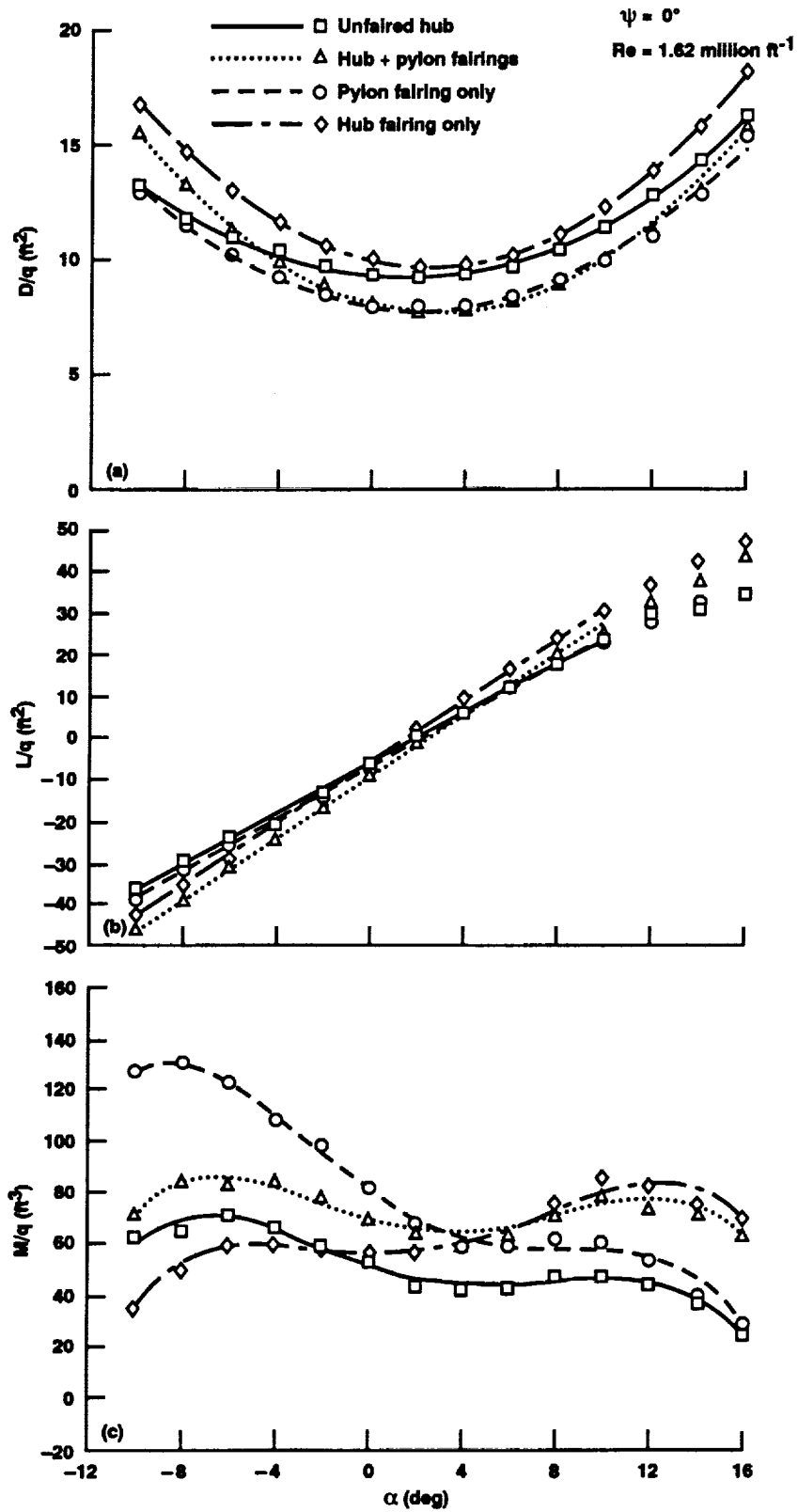


Figure 50. Variation of model drag, lift and pitching moment with α for the 22%/nontapered integrated fairing component buildup sequence at $\psi = 0^\circ$. (a) D/q , (b) L/q , (c) M/q .

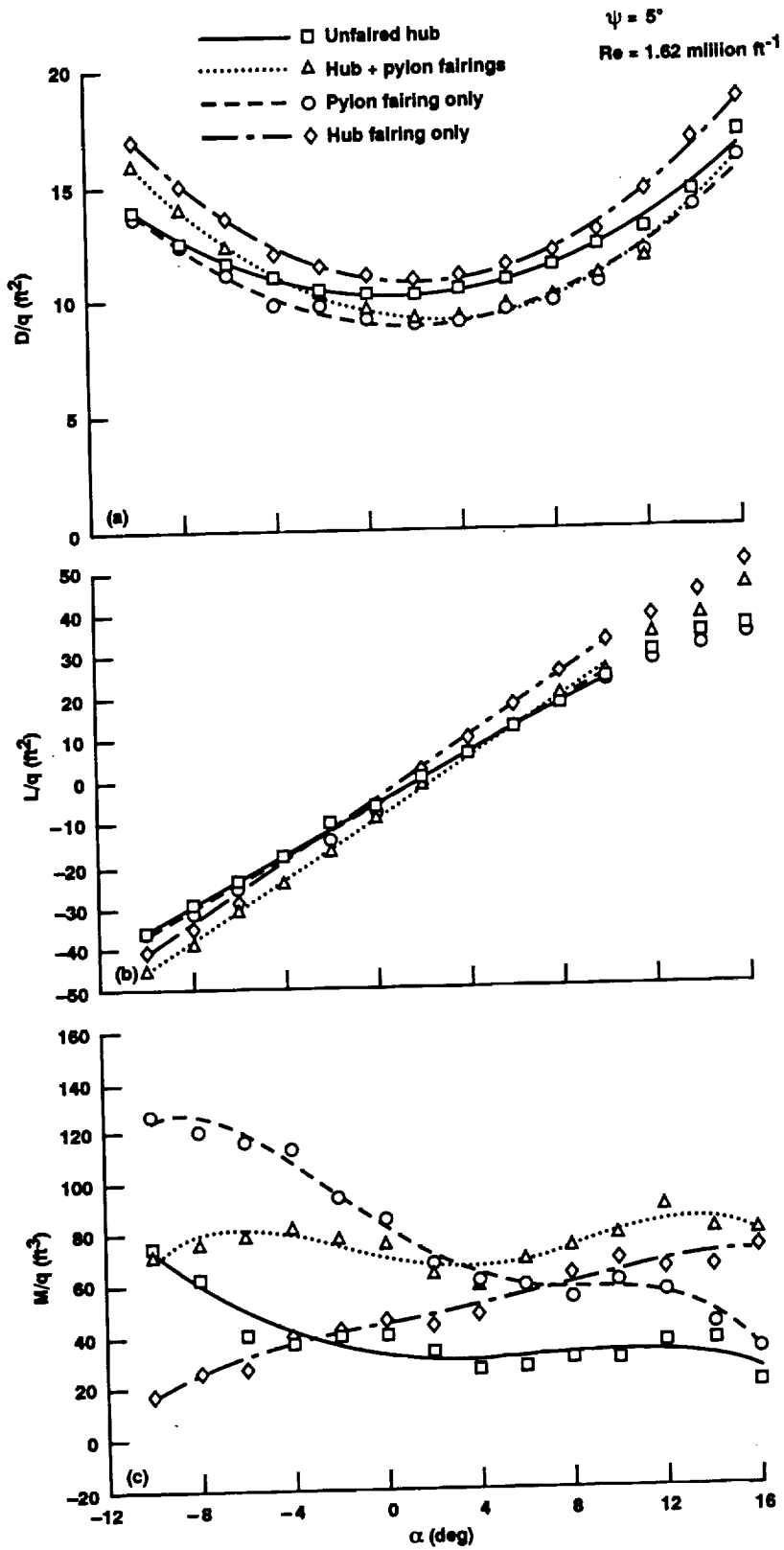


Figure 51. Variation of model drag, lift and pitching moment with α for the 22%/nontapered integrated fairing component buildup sequence at $\psi = 5^\circ$. (a) D/q , (b) L/q , (c) M/q .

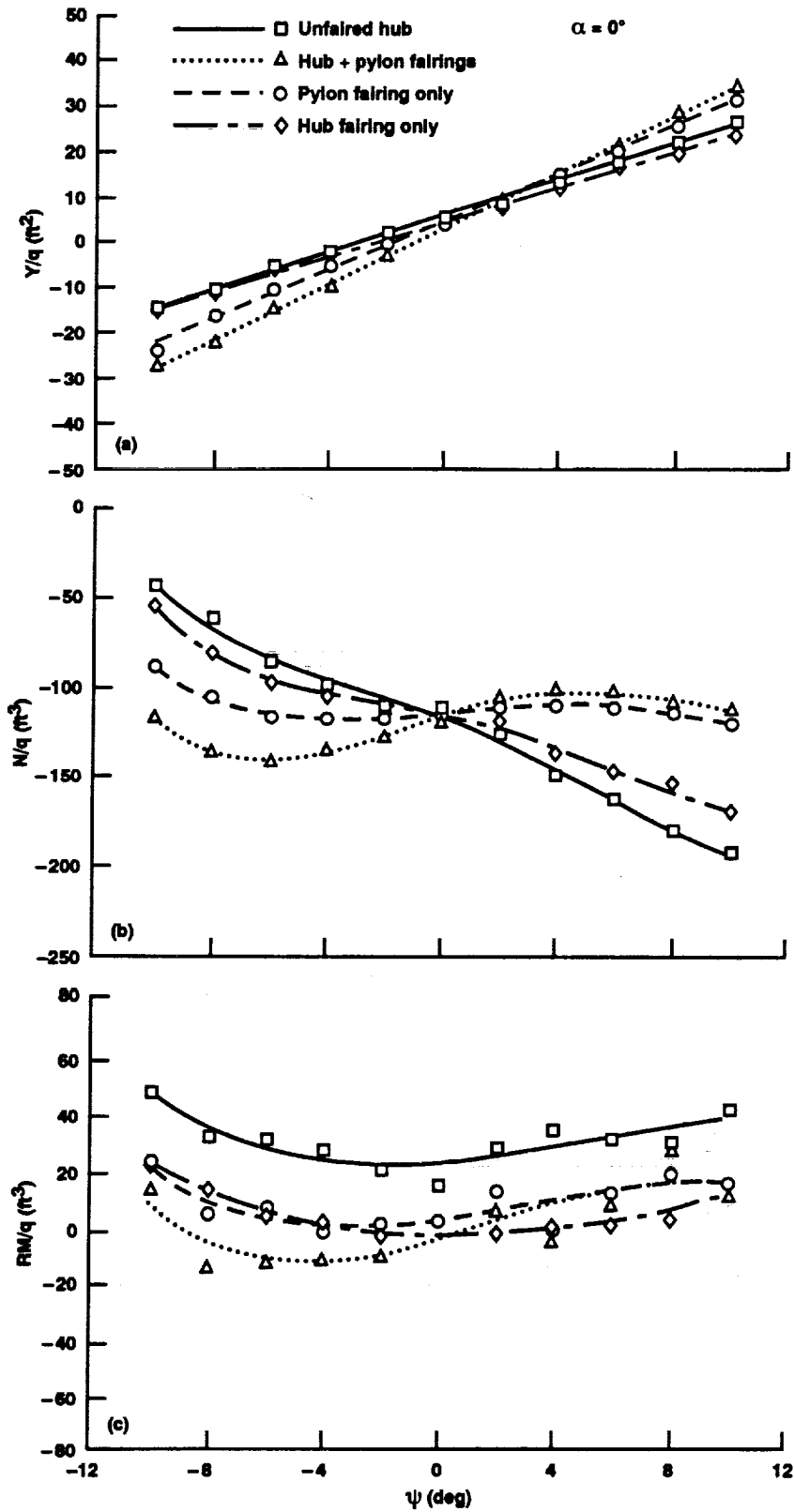


Figure 52. Variation of model side force, yawing moment, and rolling moment for the 22%/nontapered integrated fairing component buildup sequence at $\alpha = 0^\circ$. (a) Y/q , (b) N/q , (c) RM/q .

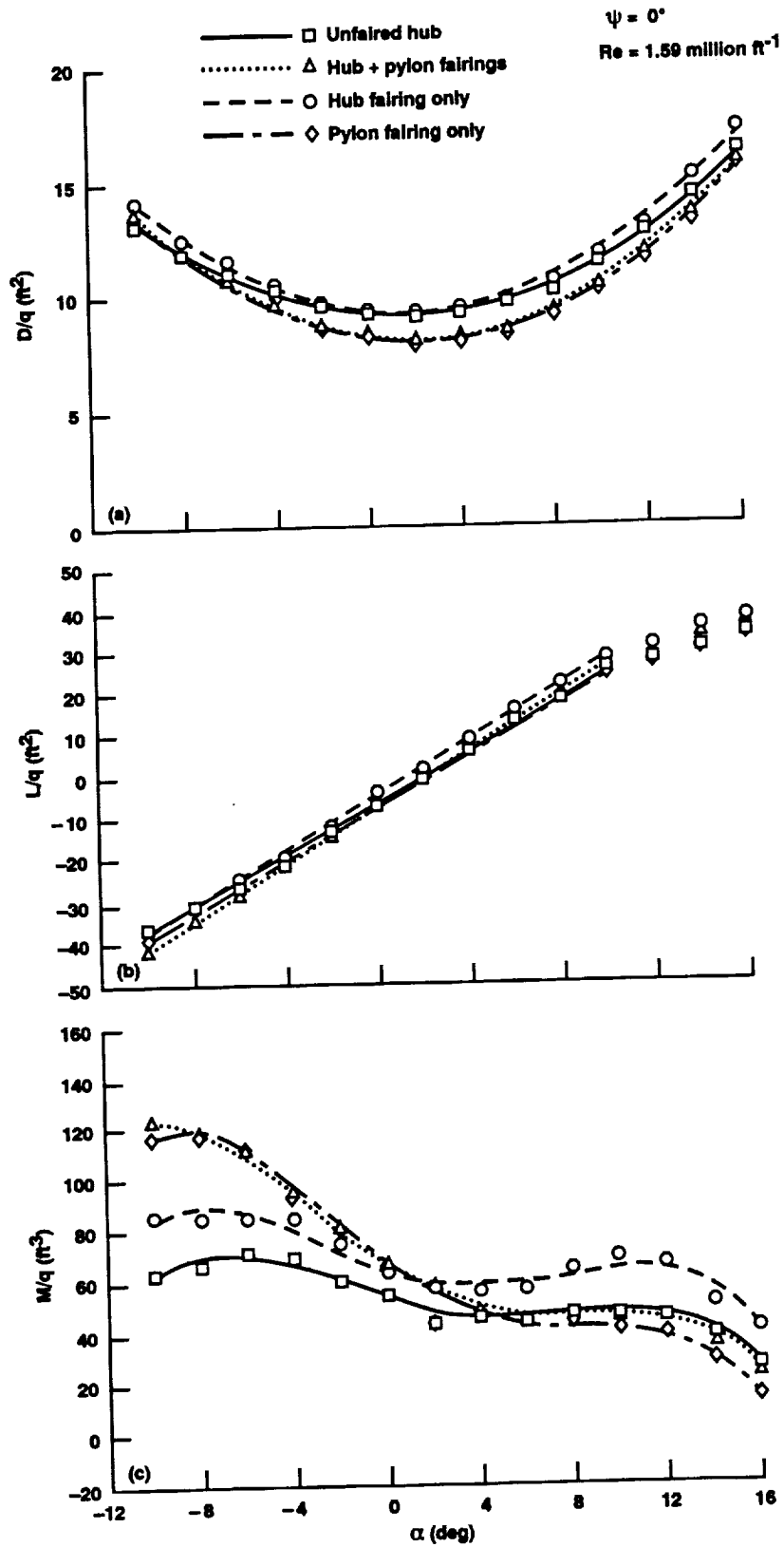


Figure 53. Variation of model drag, lift and pitching moment with α for the 15%/inverse tapered integrated fairing component buildup sequence at $\psi = 0^\circ$. (a) D/q , (b) L/q , (c) M/q .

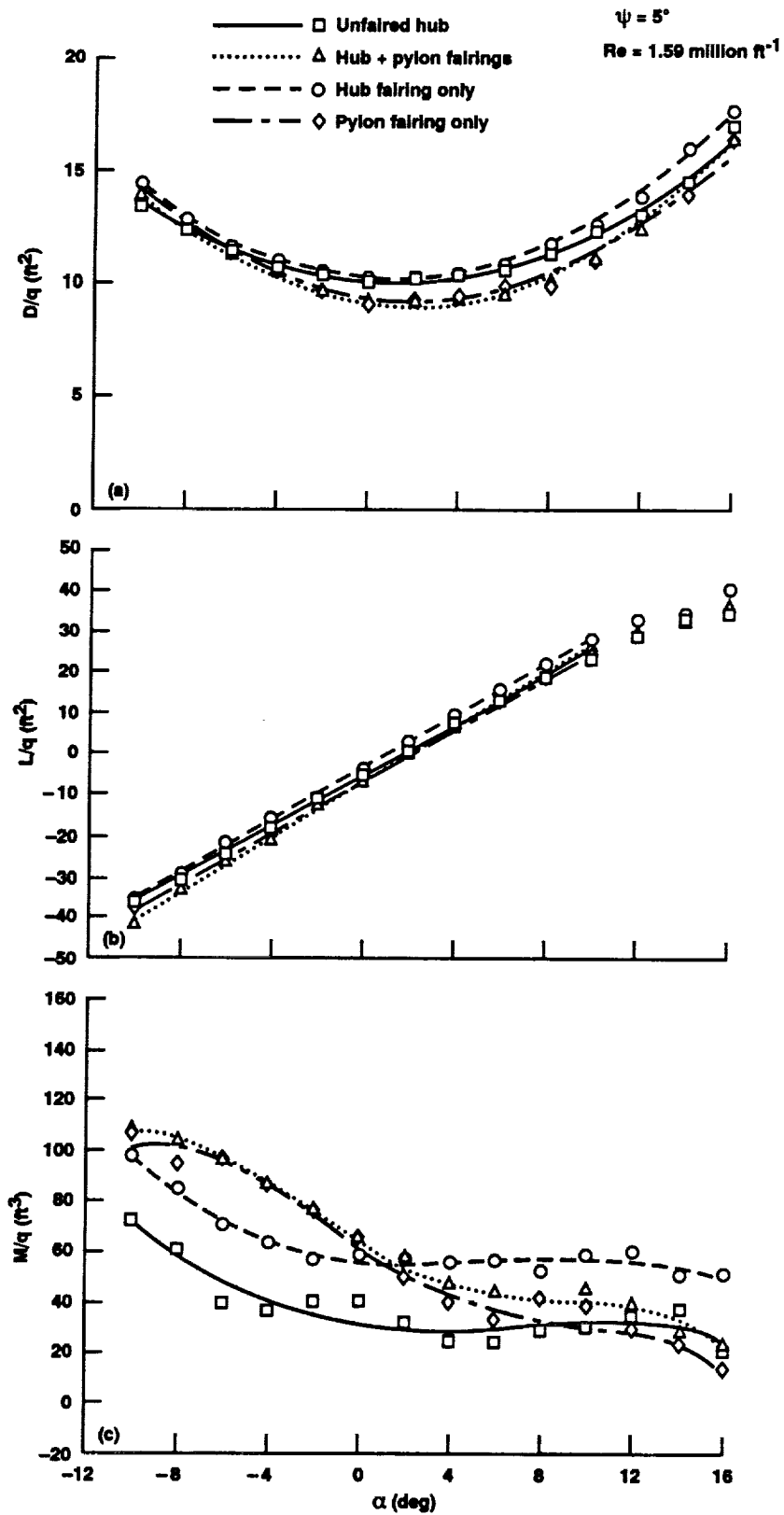


Figure 54. Variation of model drag, lift and pitching moment with α for the 15%/inverse tapered integrated fairing component buildup sequence at $\psi = 5^\circ$. (a) D/q , (b) L/q , (c) M/q .

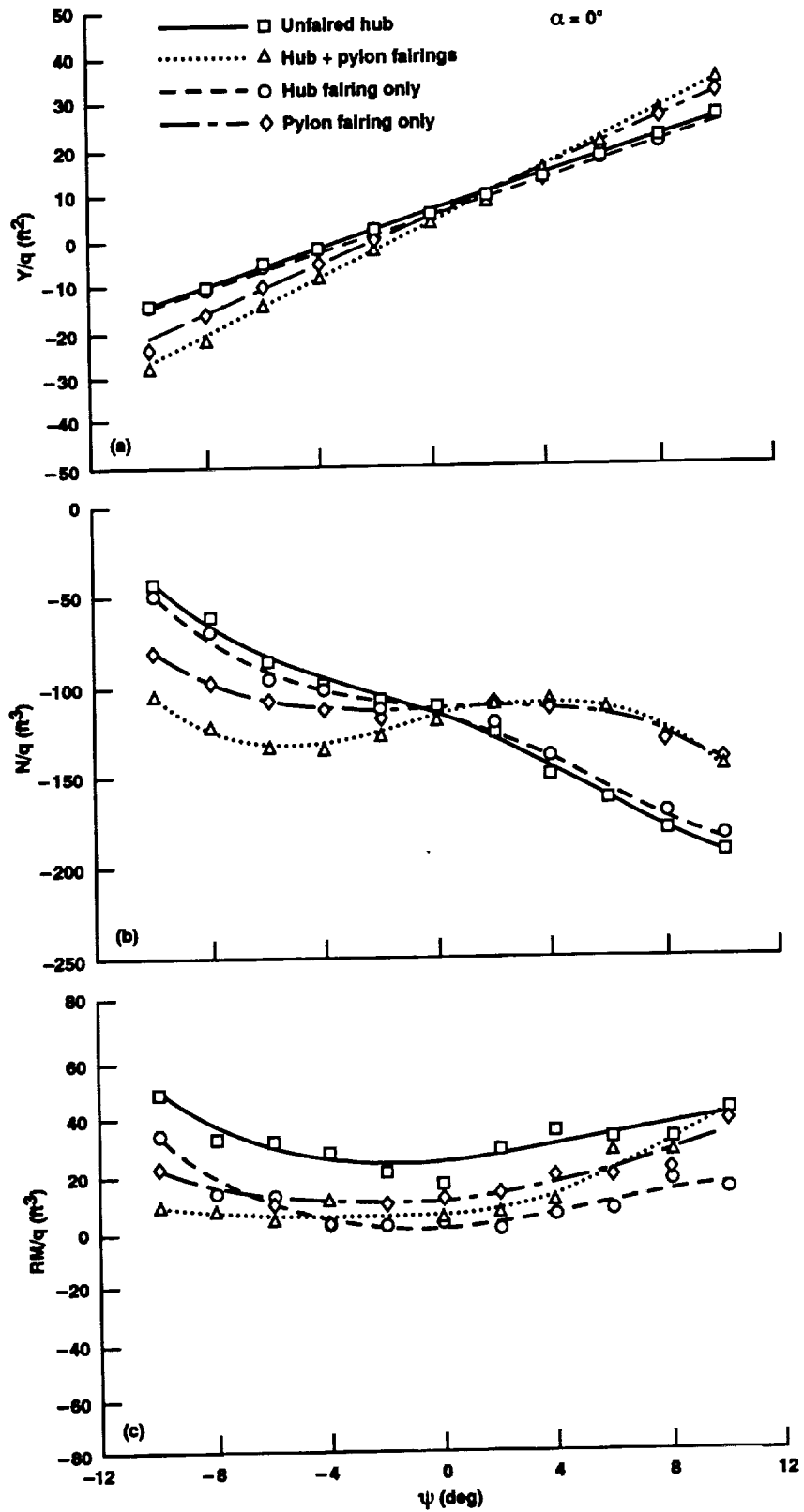


Figure 55. Variation of model side force, yawing moment, and rolling moment for the 15%/inverse tapered integrated fairing component buildup sequence at $\alpha = 0^\circ$. (a) Y/q , (b) N/q , (c) RM/q .

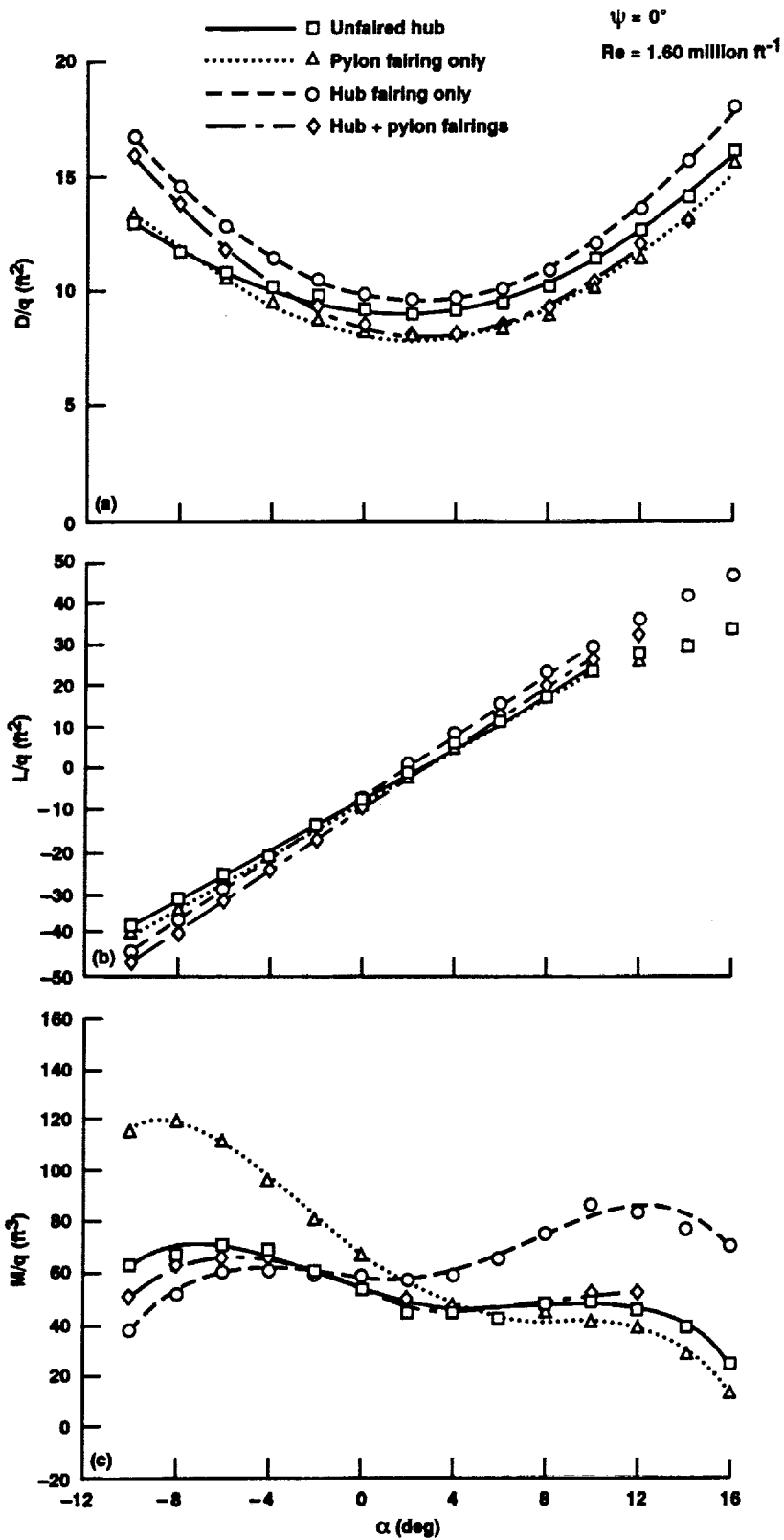


Figure 56. Variation of model drag, lift and pitching moment with α for the 22%/inverse tapered integrated fairing component buildup sequence at $\psi = 0^\circ$. (a) D/q , (b) L/q , (c) M/q .

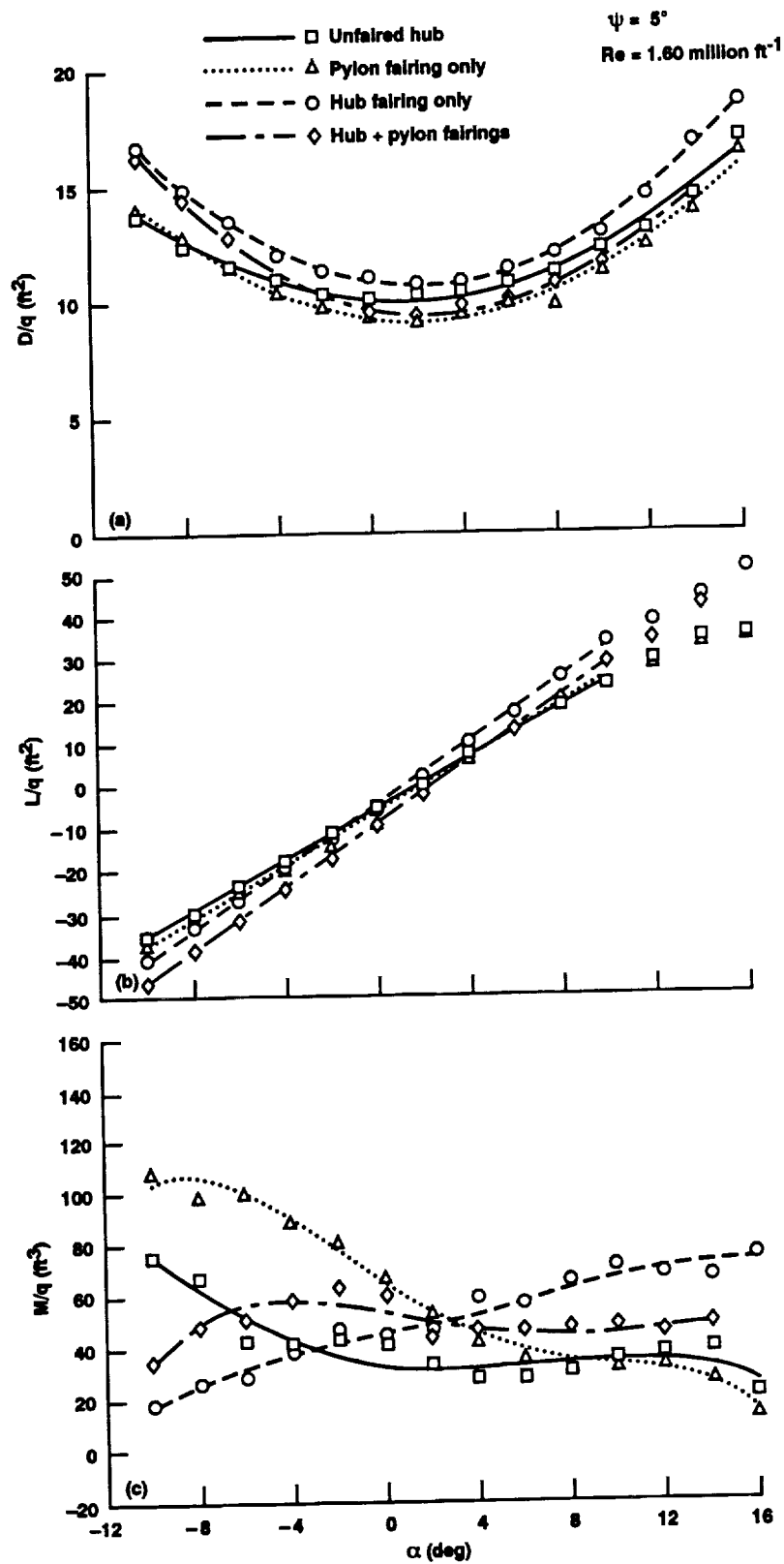


Figure 57. Variation of model drag, lift and pitching moment with α for the 22%/inverse tapered integrated fairing component buildup sequence at $\psi = 5^\circ$. (a) D/q , (b) L/q , (c) M/q .

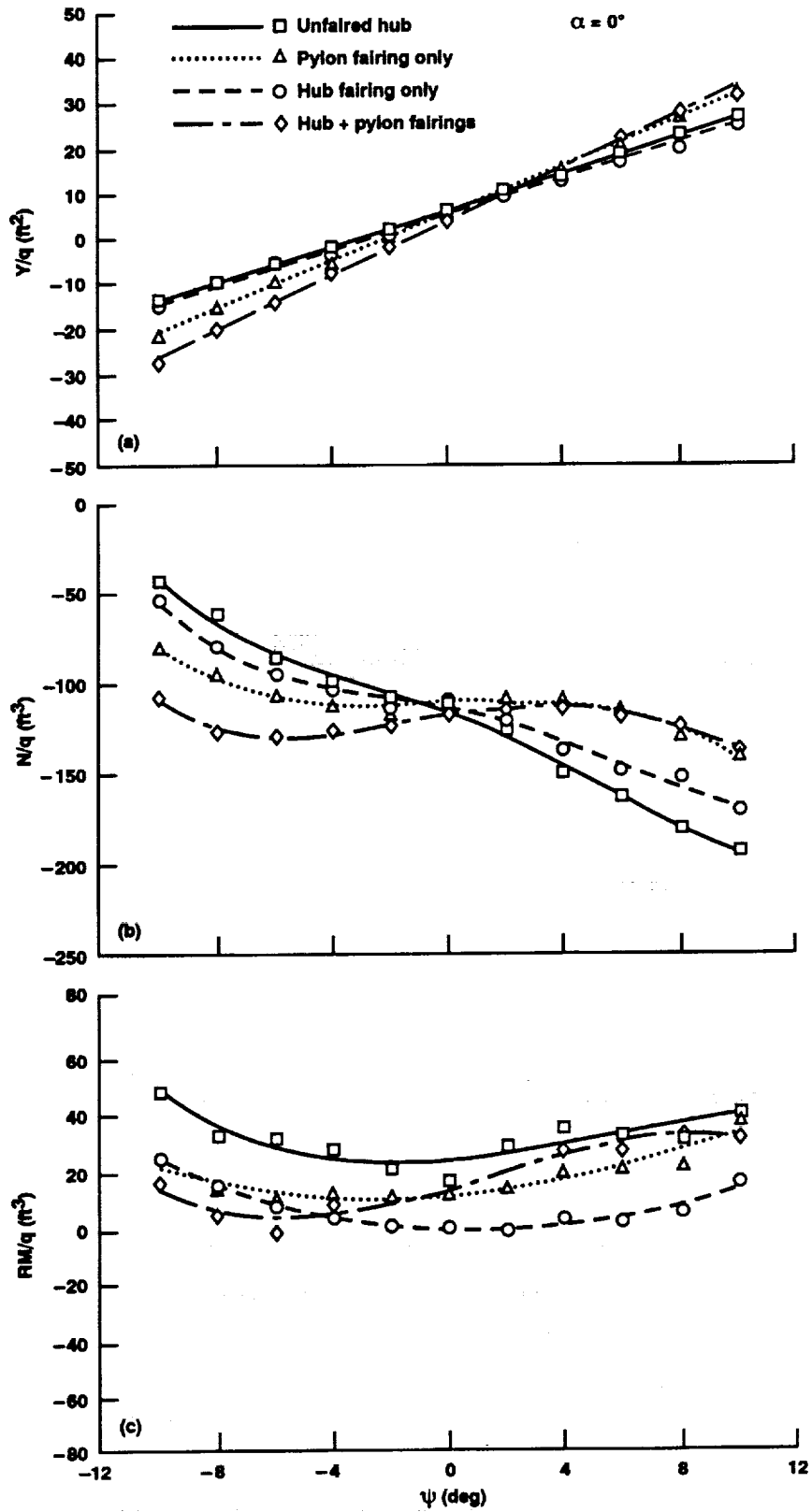


Figure 58. Variation of model side force, yawing moment and rolling moment for the 22%/inverse tapered integrated fairing component buildup sequence at $\alpha = 0^\circ$. (a) Y/q , (b) N/q , (c) RM/q .

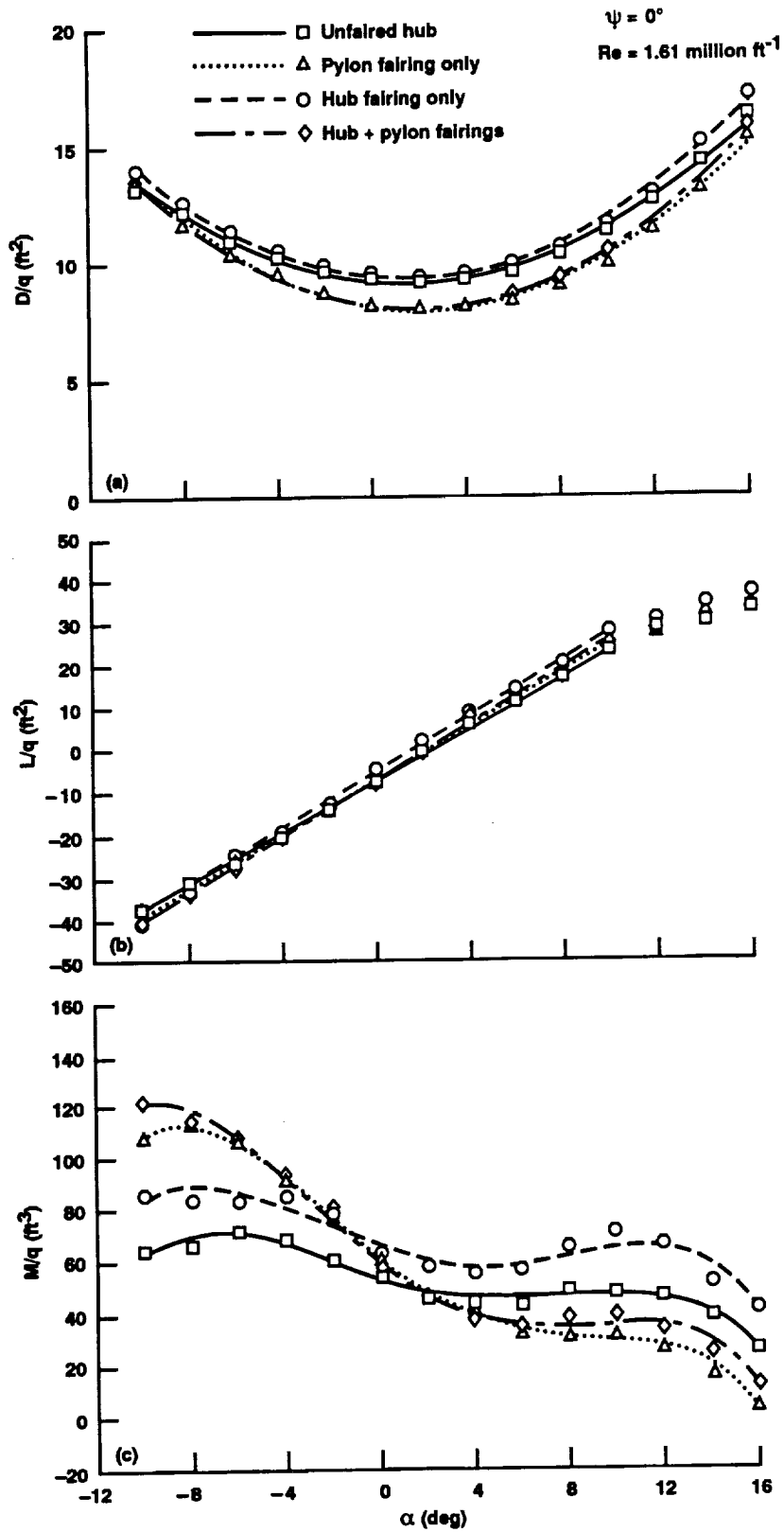


Figure 59. Variation of model drag, lift and pitching moment with α for the 15%/tapered integrated fairing component buildup sequence at $\psi = 0^\circ$. (a) D/q , (b) L/q , (c) M/q .

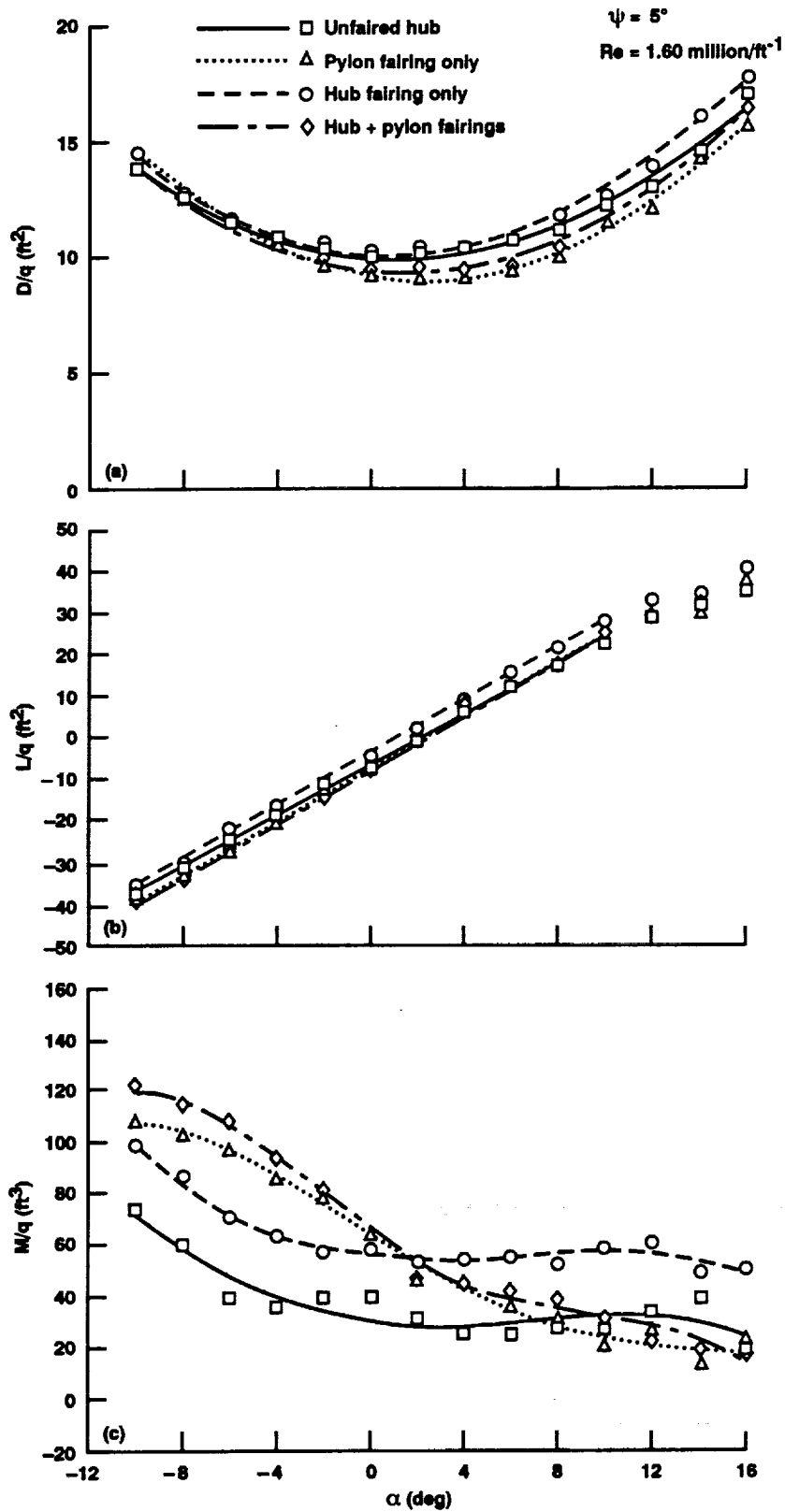


Figure 60. Variation of model drag, lift and pitching moment with α for the 15%/tapered integrated fairing component buildup sequence at $\psi = 5^\circ$. (a) D/q , (b) L/q , (c) M/q .

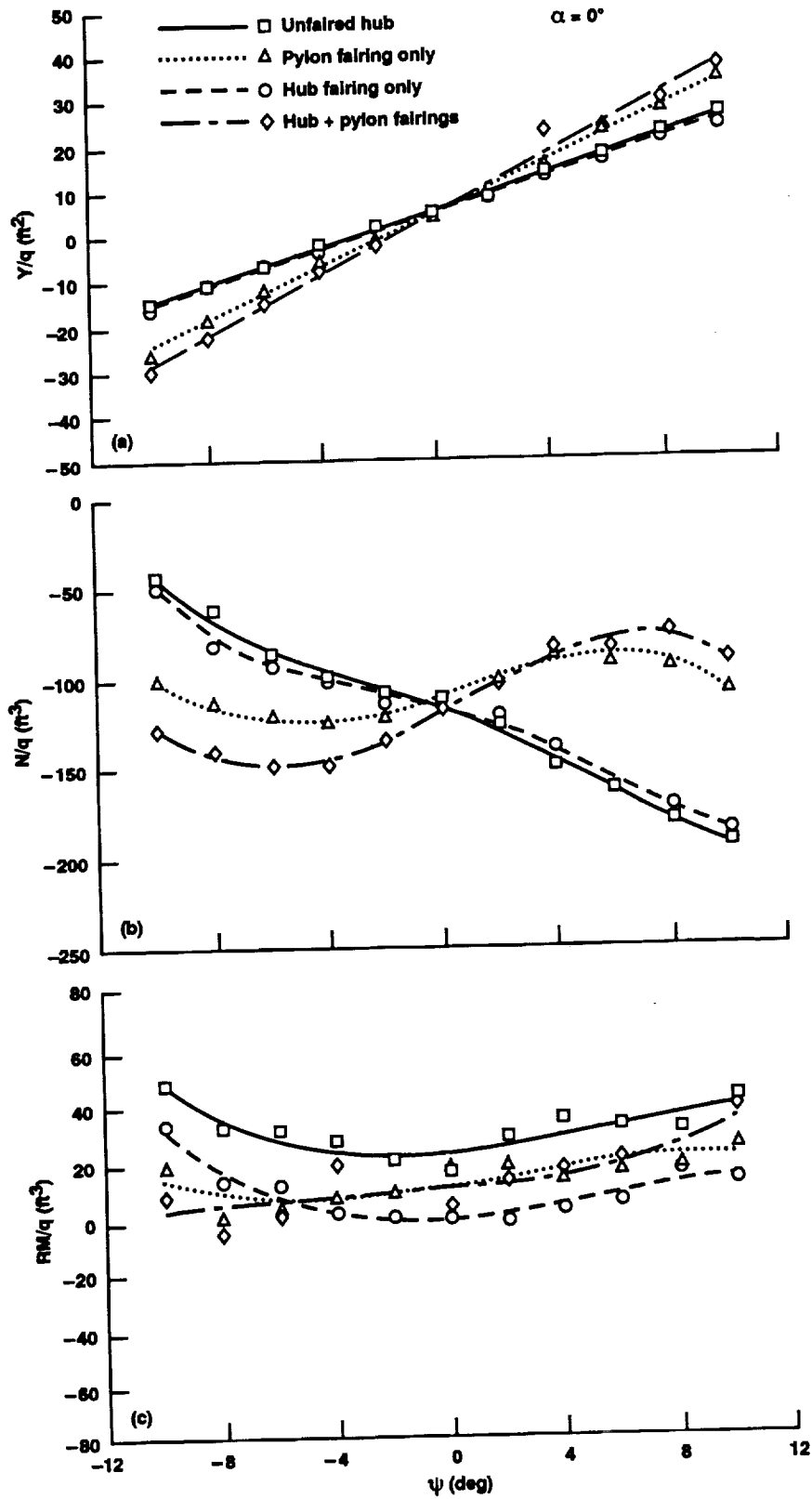


Figure 61. Variation of model side force, yawing moment, and rolling moment for the 15%/tapered integrated fairing component buildup sequence at $\alpha = 0^\circ$. (a) Y/q , (b) N/q , (c) RM/q .

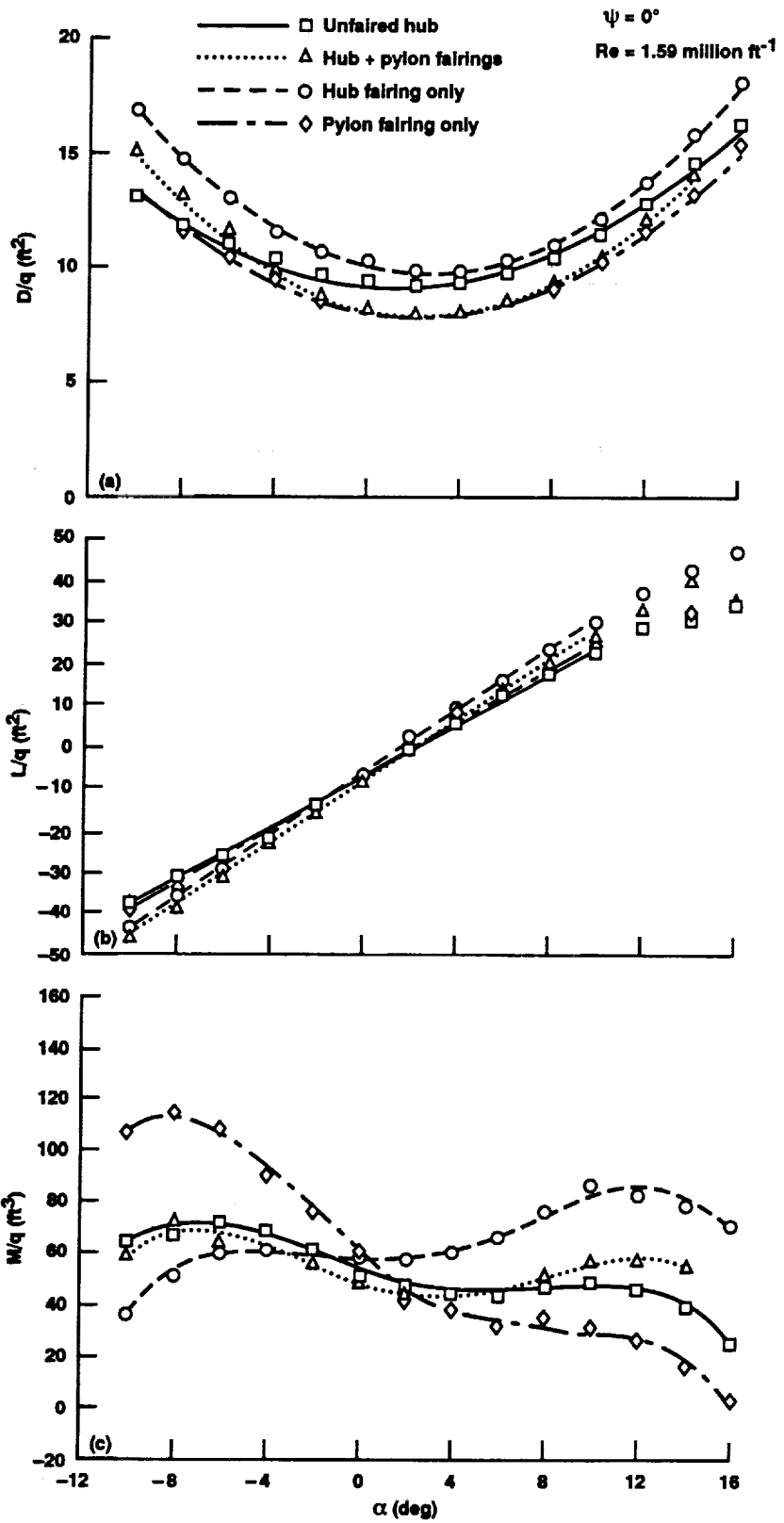


Figure 62. Variation of model drag, lift and pitching moment with α for the 22%/tapered integrated fairing component buildup sequence at $\psi = 0^\circ$. (a) D/q , (b) L/q , (c) M/q .

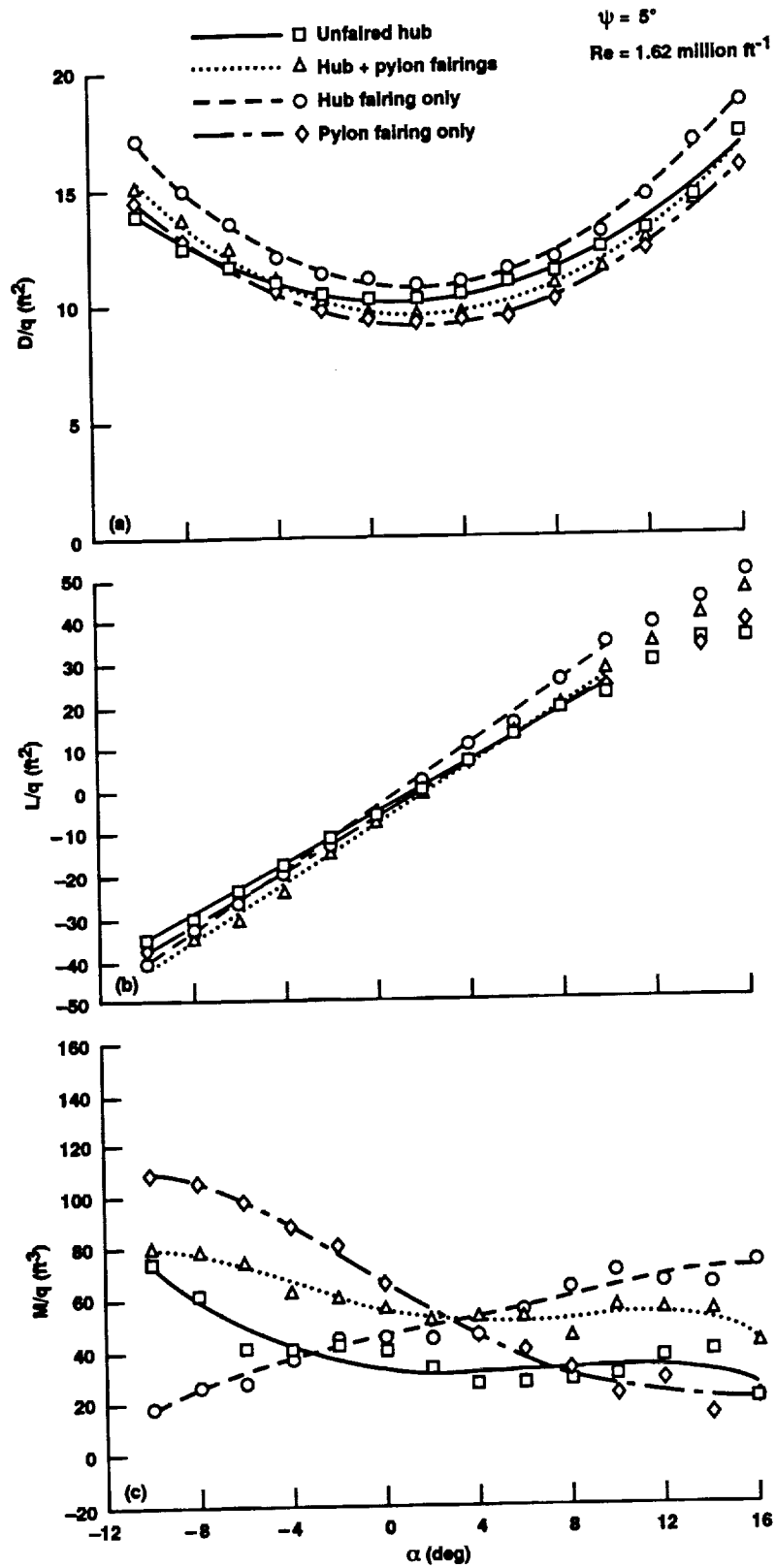


Figure 63. Variation of model drag, lift and pitching moment with α for the 22%/tapered integrated fairing component buildup sequence at $\psi = 5^\circ$. (a) D/q , (b) L/q , (c) M/q .

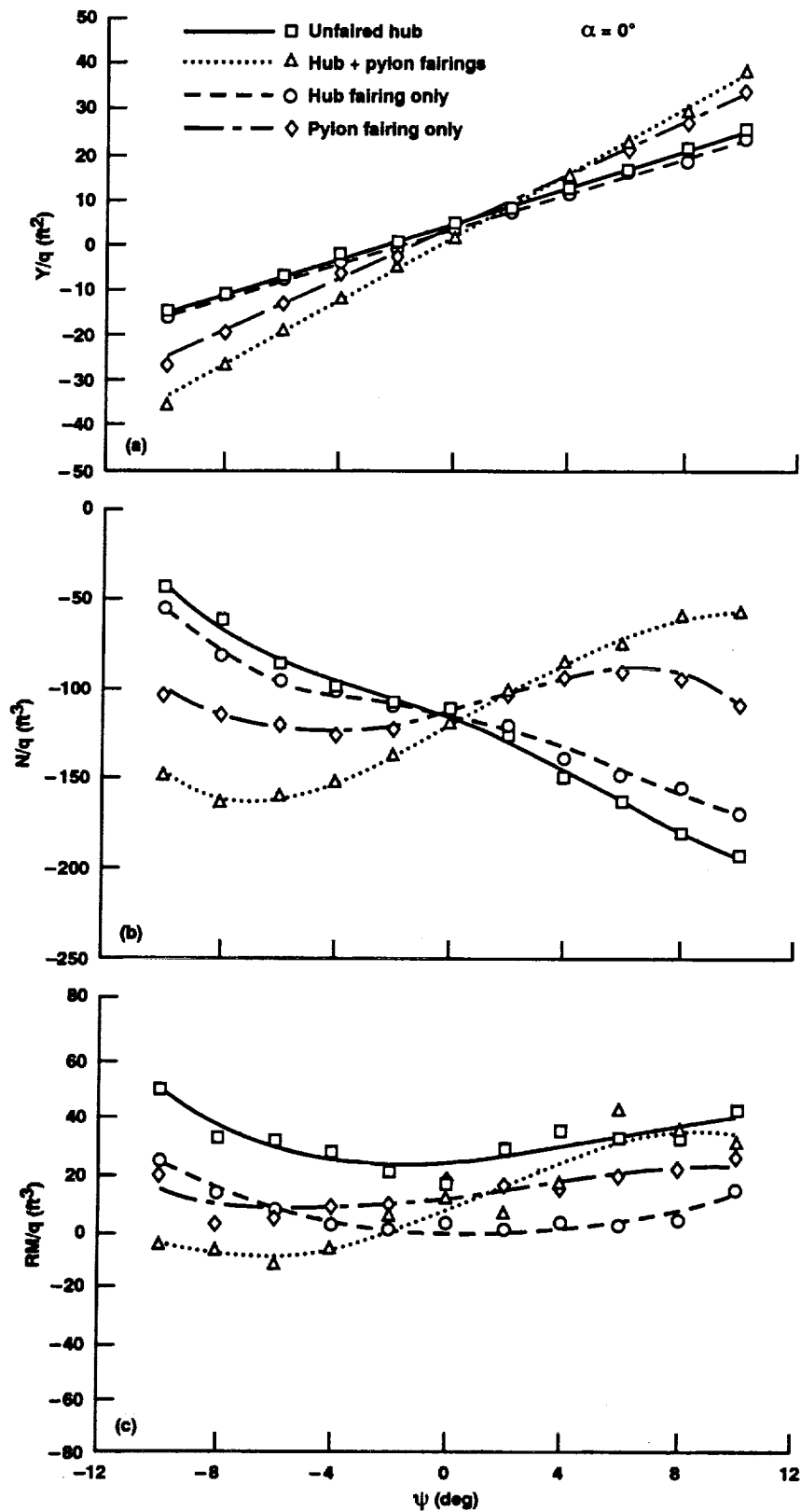


Figure 64. Variation of model side force, yawing moment, and rolling moment for the 22%/tapered integrated fairing component buildup sequence at $\alpha = 0^\circ$. (a) Y/q , (b) N/q , (c) RM/q .

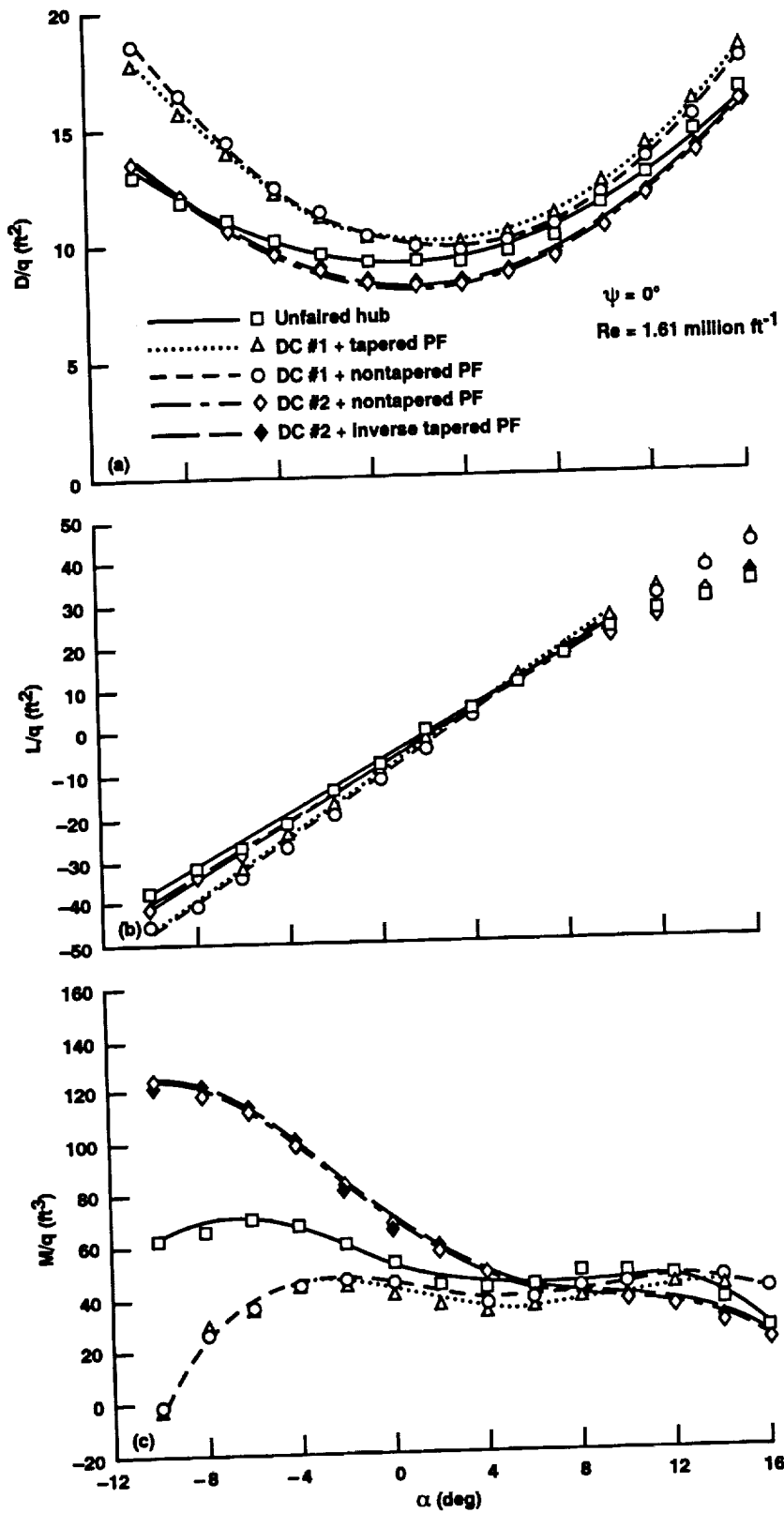


Figure 65. Variation of model drag, lift and pitching moment with α for the dual component configurations at $\psi = 0^\circ$.
 (a) D/q , (b) L/q , (c) M/q .

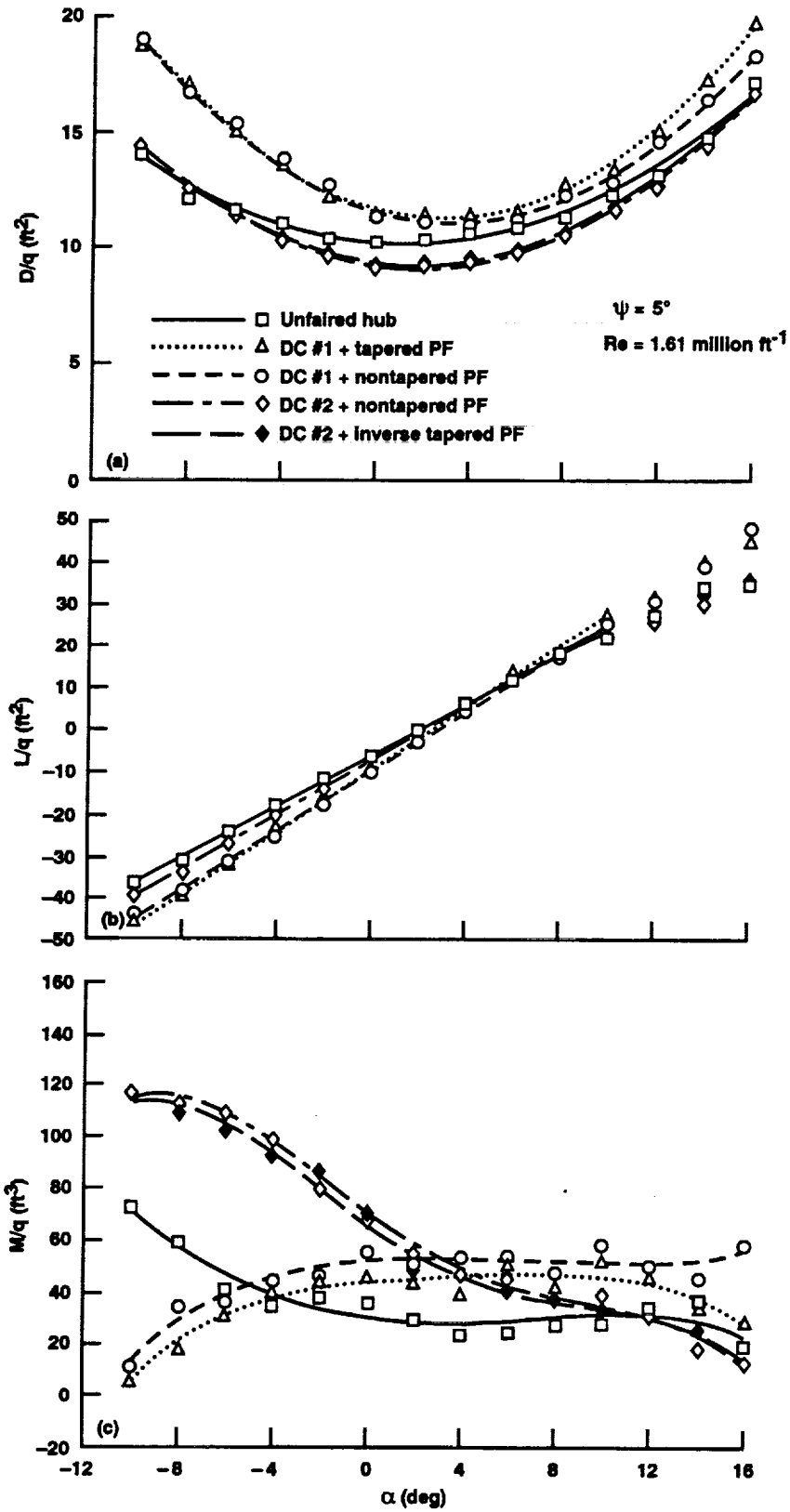


Figure 66. Variation of model drag, lift and pitching moment with α for the dual component configurations at $\psi = 5^\circ$. (a) D/q , (b) L/q , (c) M/q .

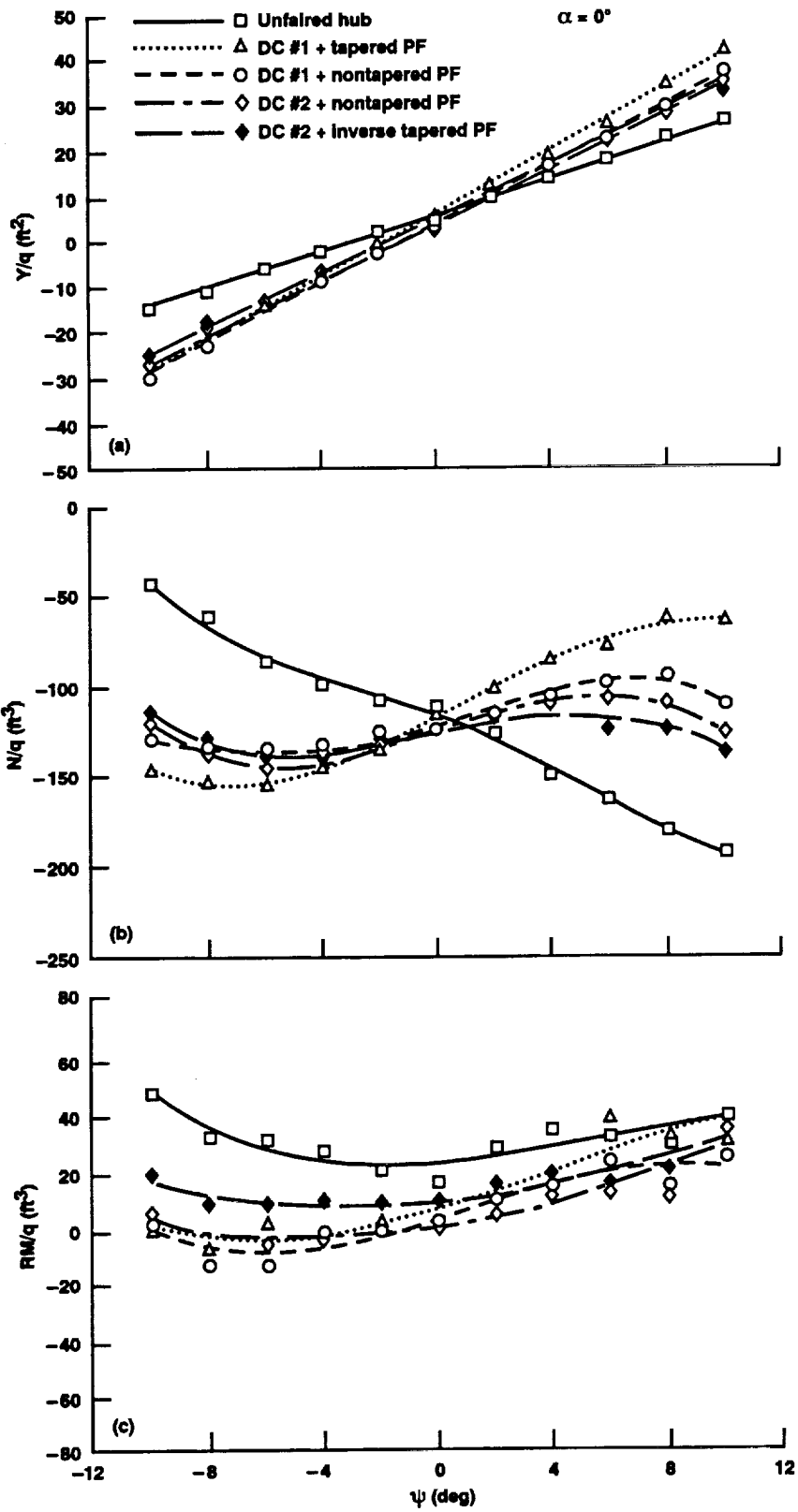


Figure 67. Variation of model side force, yawing moment, and rolling moment for the dual component configurations at $\alpha = 0^\circ$. (a) Y/q , (b) N/q , (c) RM/q .

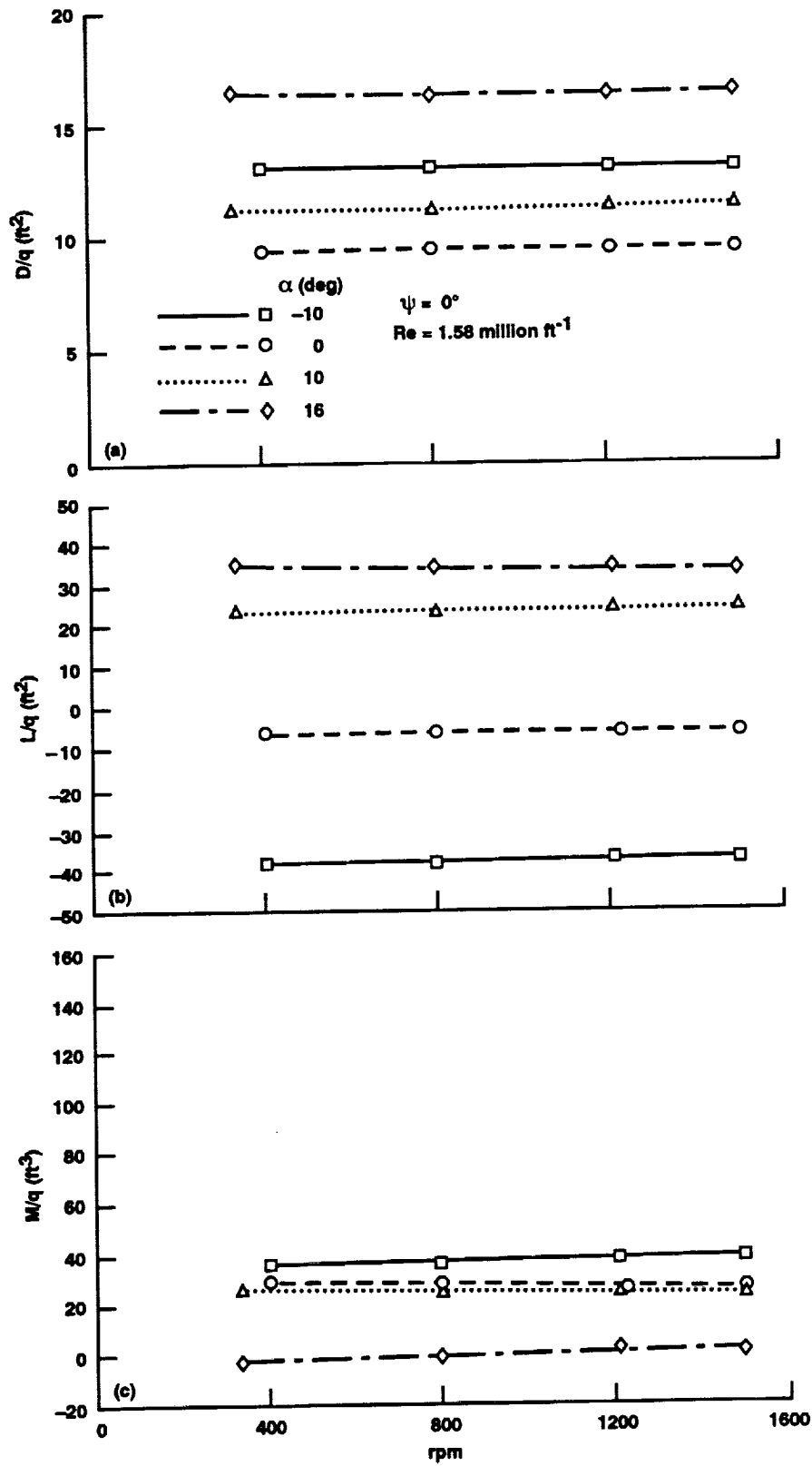


Figure 68. Variation of model drag, lift and pitching moment with RPM for the unfaired hub configuration at $\psi = 0^\circ$. (a) D/q , (b) L/q , (c) M/q .

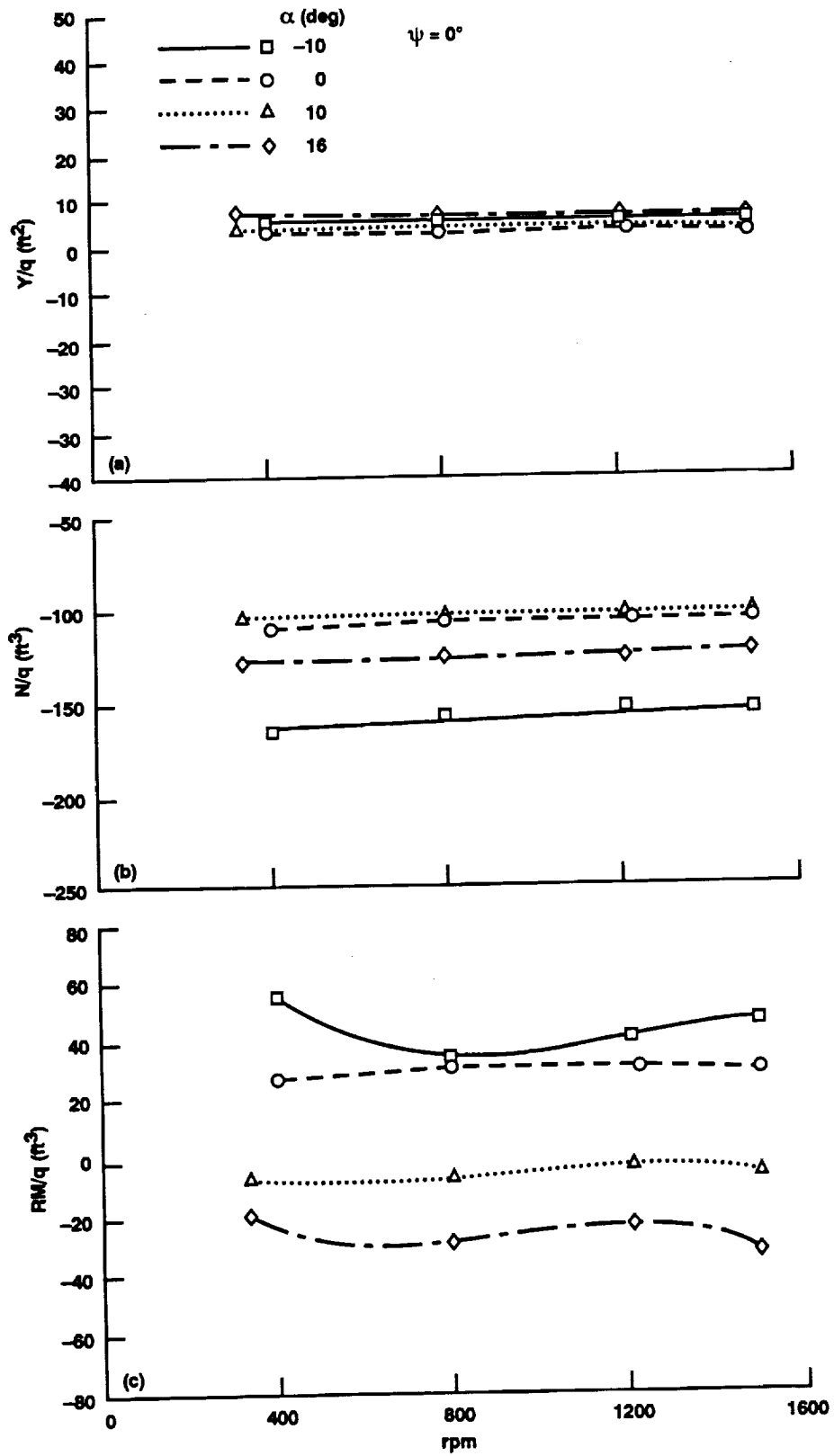


Figure 69. Variation of model side force, yawing moment, and rolling moment with RPM for the unfaired hub configuration at $\psi = 0^\circ$. (a) Y/q , (b) N/q , (c) RM/q .

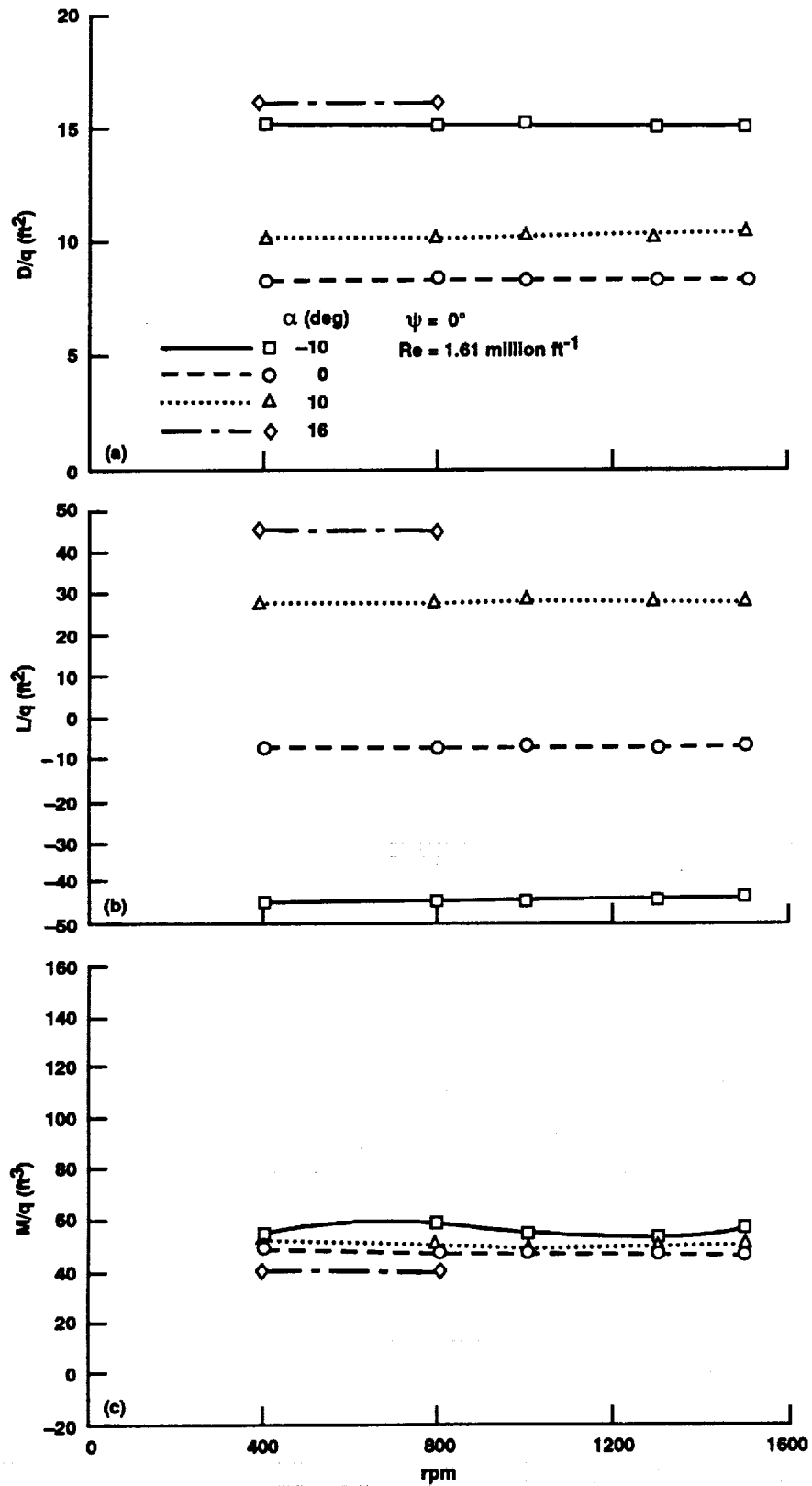


Figure 70. Variation of model drag, lift and pitching moment with RPM for the 22%/tapered integrated fairing configuration at $\psi = 0^\circ$. (a) D/q , (b) L/q , (c) M/q .

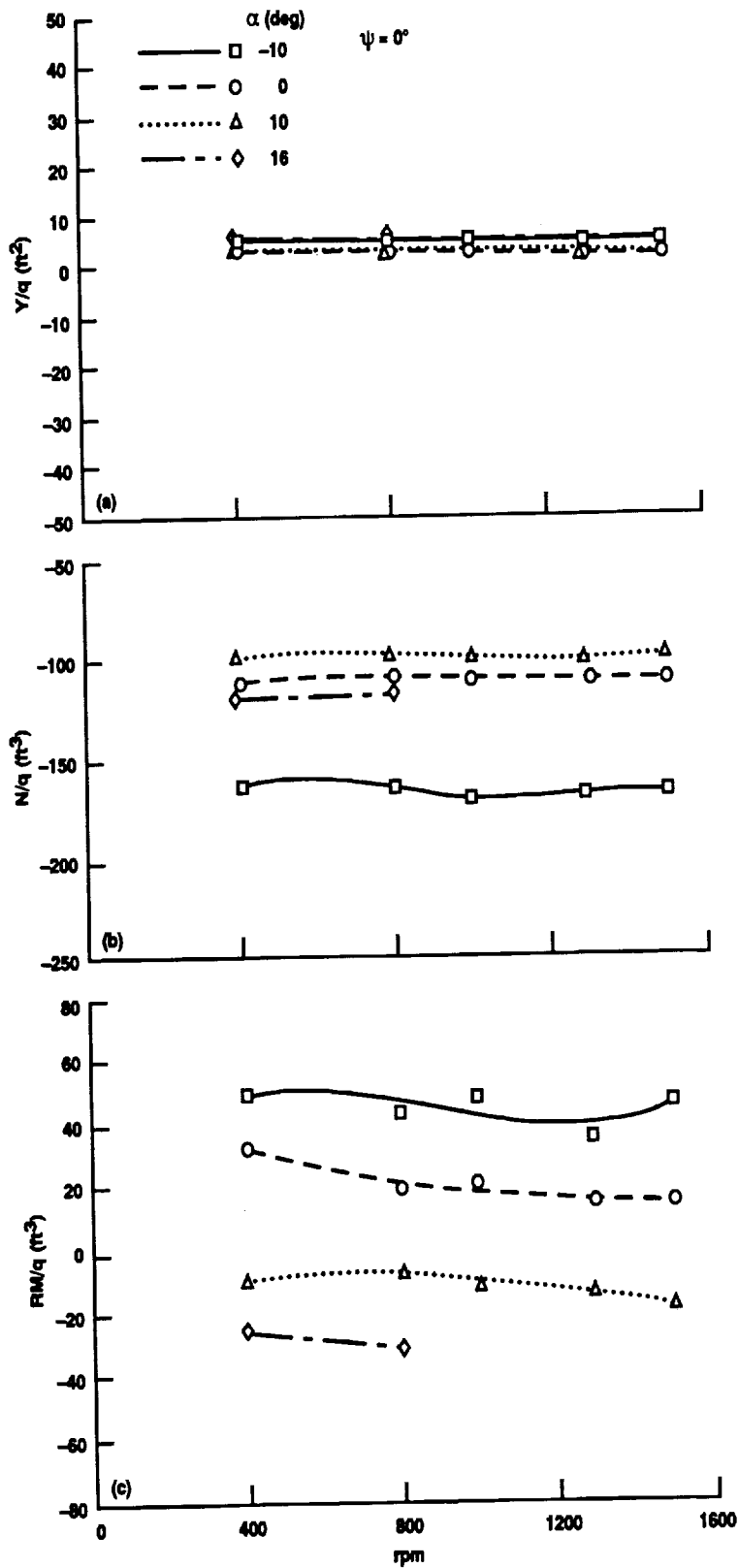


Figure 71. Variation of model side force, yawing moment, and rolling moment with RPM for the 22%/tapered integrated fairing configuration at $\psi = 0^\circ$. (a) Y/q , (b) N/q , (c) RM/q .

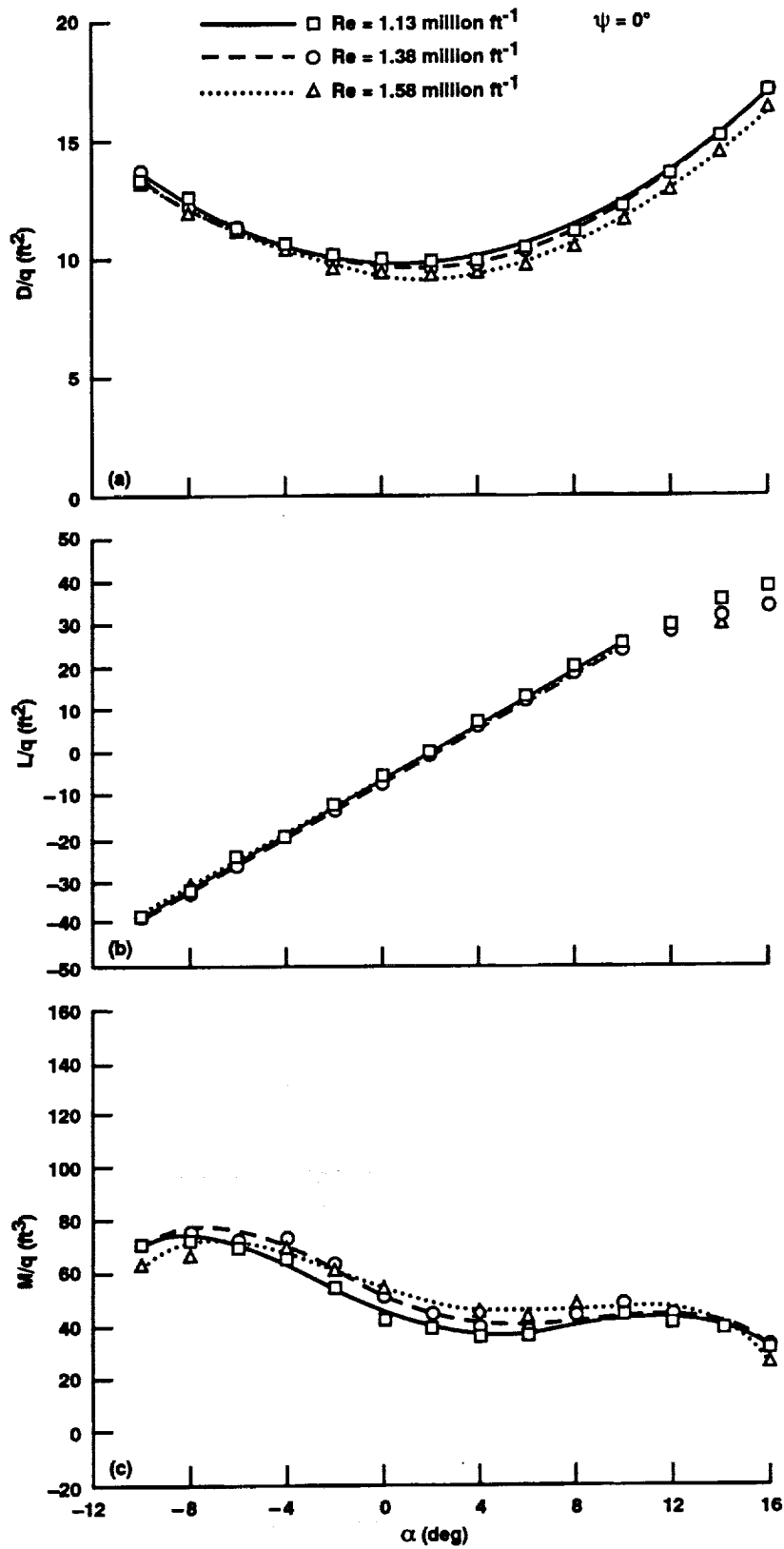


Figure 72. Variation of model drag, lift and pitching moment with α for the unfaired hub configuration for three Reynolds numbers at $\psi = 0^\circ$. (a) D/q , (b) L/q , (c) M/q .

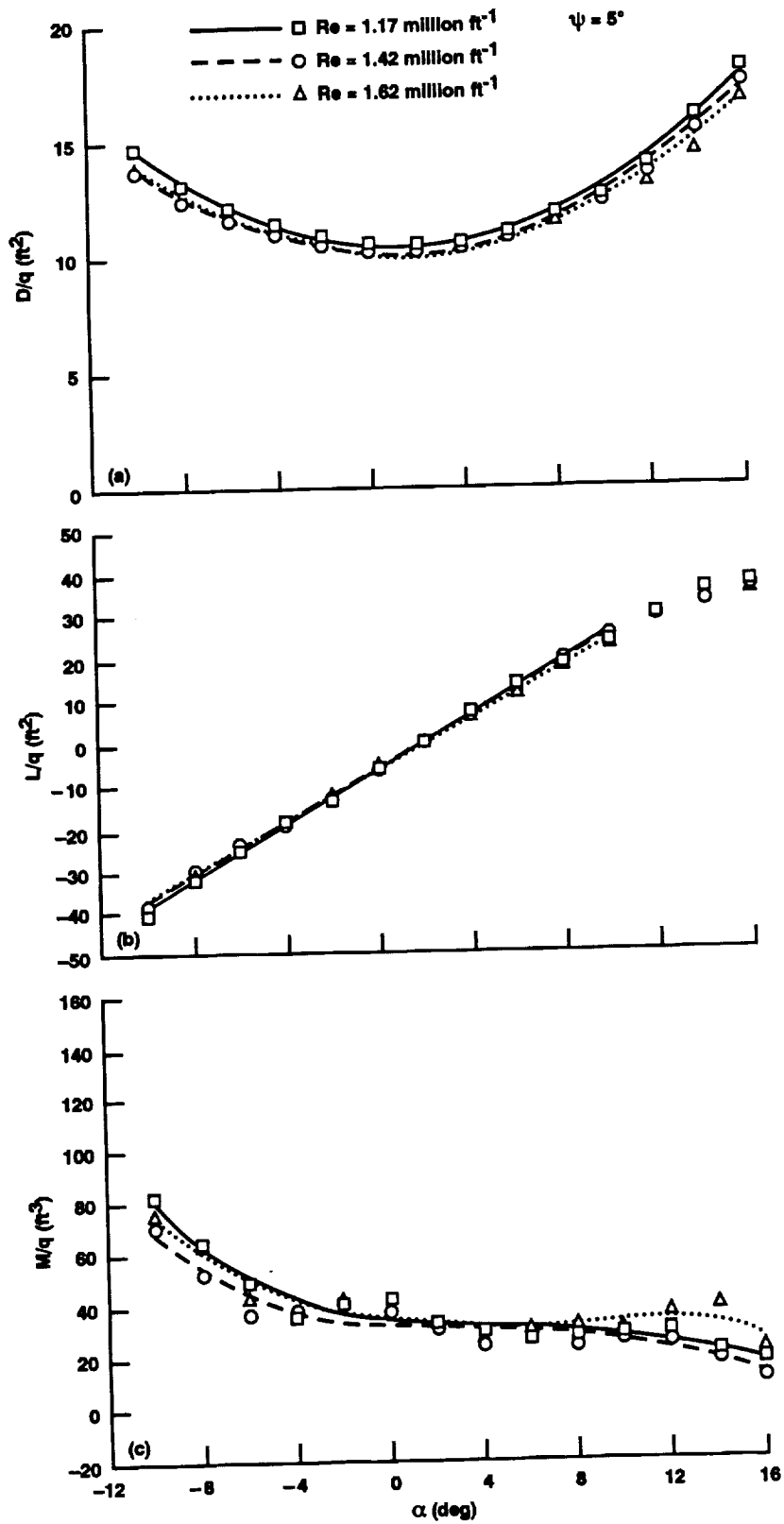


Figure 73. Variation of model drag, lift and pitching moment with α for the unfaired hub configuration for three Reynolds numbers at $\psi = 5^\circ$. (a) D/q , (b) L/q , (c) M/q .

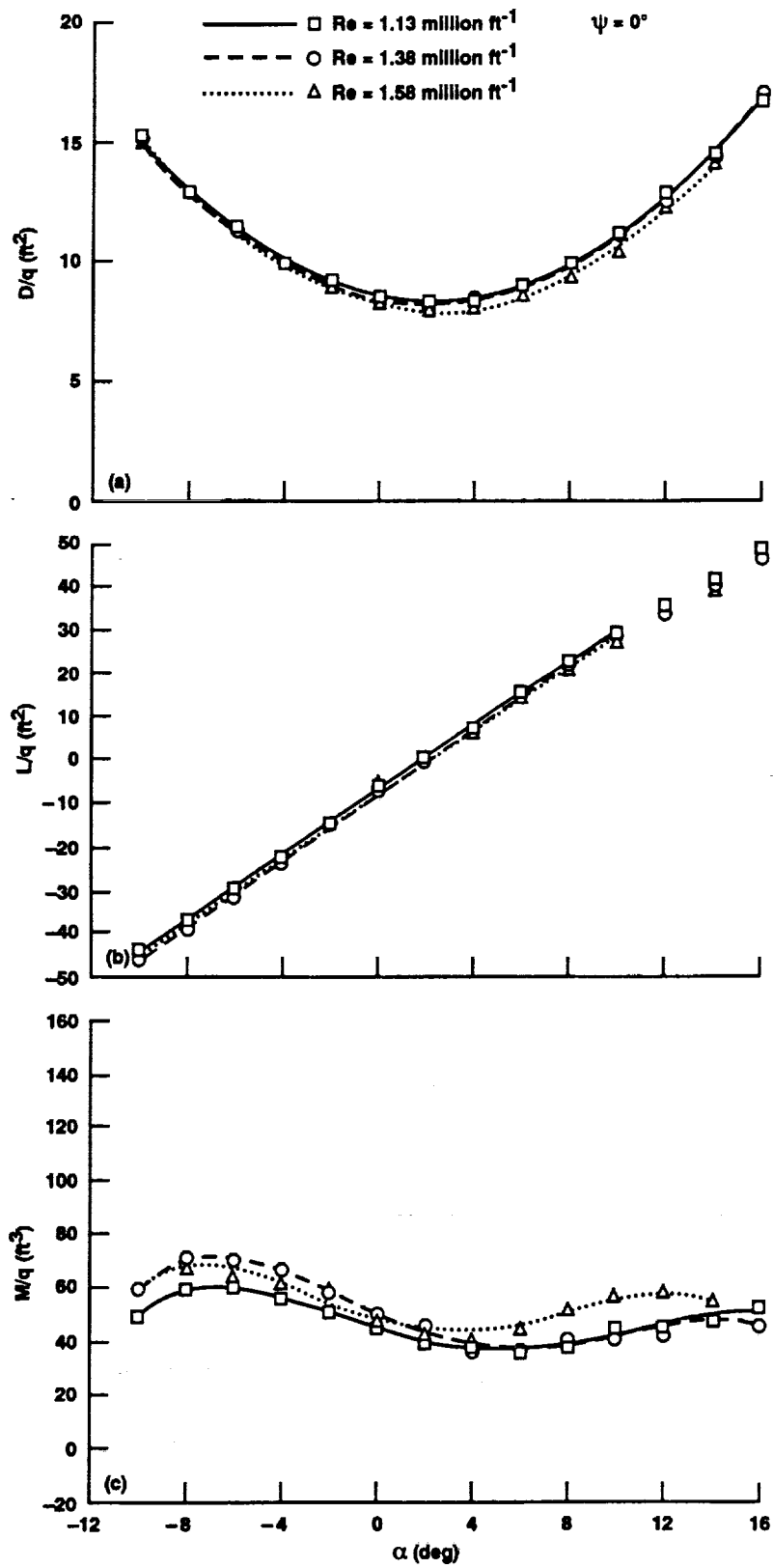


Figure 74. Variation of model drag, lift and pitching moment with α for the 22%/tapered integrated configuration for three Reynolds numbers at $\psi = 0^\circ$. (a) D/q , (b) L/q , (c) M/q .

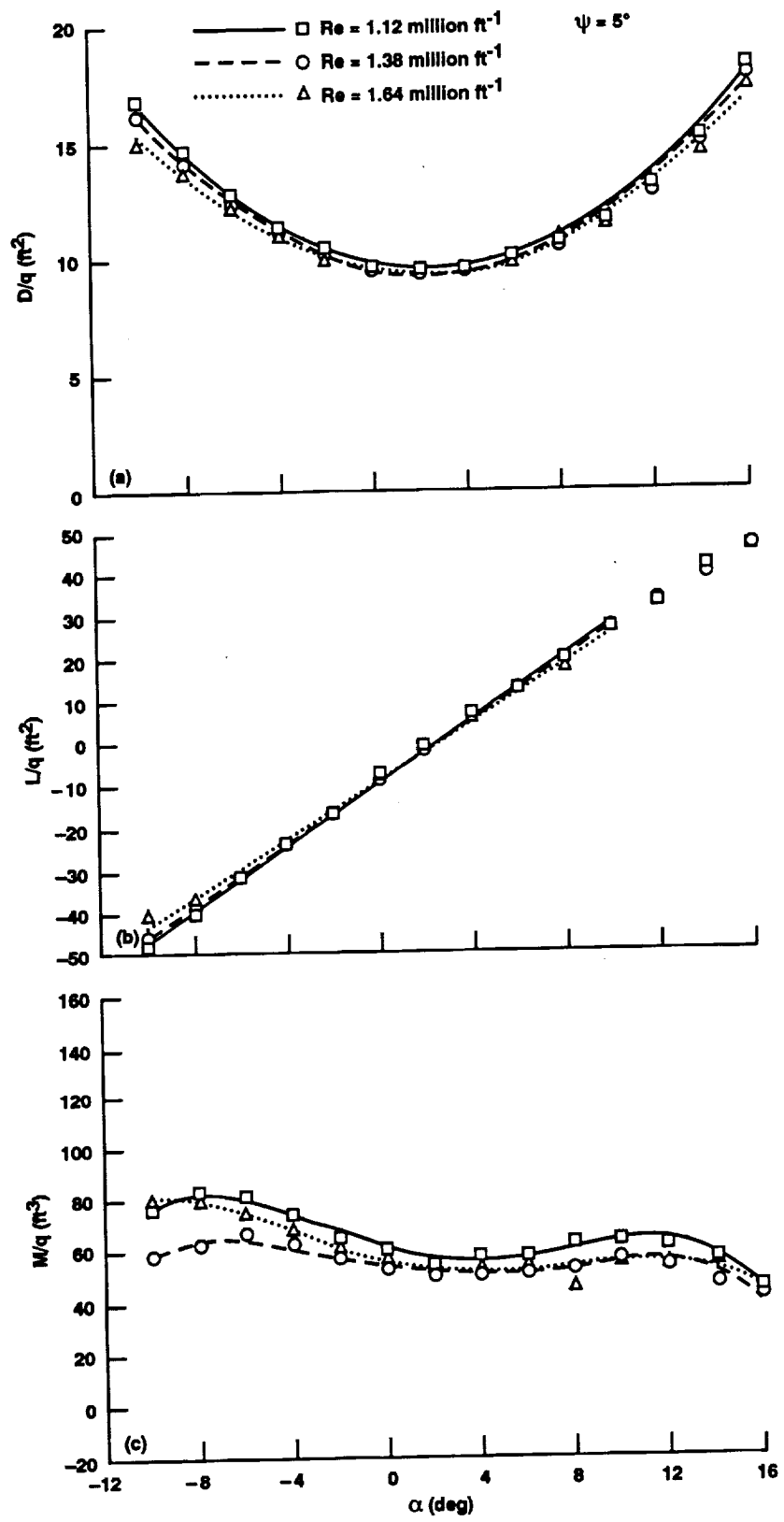


Figure 75. Variation of model drag, lift and pitching moment with α for the 22%/tapered integrated configuration for three Reynolds numbers at $\psi = 5^\circ$. (a) D/q , (b) L/q , (c) M/q .

REPORT DOCUMENTATION PAGE

Form Approved
OMB No. 0704-0188

Public reporting burden for this collection of information is estimated to average 1 hour per response, including the time for reviewing instructions, searching existing data sources, gathering and maintaining the data needed, and completing and reviewing the collection of information. Send comments regarding this burden estimate or any other aspect of this collection of information, including suggestions for reducing this burden, to Washington Headquarters Services, Directorate for Information Operations and Reports, 1215 Jefferson Davis Highway, Suite 1204, Arlington, VA 22202-4302, and to the Office of Management and Budget, Paperwork Reduction Project (0704-0188), Washington, DC 20503.

1. AGENCY USE ONLY (Leave blank)	2. REPORT DATE September 1993	3. REPORT TYPE AND DATES COVERED Technical Memorandum	
4. TITLE AND SUBTITLE Experimental Investigation of Advanced Hub and Pylon Fairing Configurations to Reduce Helicopter Drag		5. FUNDING NUMBERS 505-59-36	
6. AUTHOR(S) D. M. Martin,* R. W. Mort,** L. A. Young, and P. K. Squires**			
7. PERFORMING ORGANIZATION NAME(S) AND ADDRESS(ES) Ames Research Center Moffett Field, CA 94035-1000		8. PERFORMING ORGANIZATION REPORT NUMBER A-93079	
9. SPONSORING/MONITORING AGENCY NAME(S) AND ADDRESS(ES) National Aeronautics and Space Administration Washington, DC 20546-0001		10. SPONSORING/MONITORING AGENCY REPORT NUMBER NASA TM-4540	
11. SUPPLEMENTARY NOTES Point of Contact: D. M. Martin, c/o Ames Research Center, MS T042, Moffett Field, CA 94035-1000, (415) 604-4566 *Sterling Software, Palo Alto, California **Bell Helicopter Textron, Inc., Fort Worth, Texas			
12a. DISTRIBUTION/AVAILABILITY STATEMENT Unclassified — Unlimited Subject Category 05		12b. DISTRIBUTION CODE	
13. ABSTRACT (Maximum 200 words) New hub and pylon fairing designs were tested on a one-fifth scale Bell Helicopter Textron Model 222 helicopter with a bearingless main rotor hub. The blades were not installed for this test. The fairings were designed by NASA and Bell Helicopter Textron under a joint program and tested in the Ames Research Center 7- by 10-Foot Wind Tunnel. All six aircraft forces and moments were measured using the tunnel scales system. Previous research has identified the integrated hub and pylon fairing approach as the most efficient in reducing helicopter drag. Three hub fairings and three pylon fairings were tested (in various combinations) resulting in a total of 16 different configurations, including the baseline helicopter model without fairings. The geometry of the new fairings is described in detail. Test results are presented in the form of plots of the six model forces and moments. The data show that model drag can be reduced by as much as 20% by combining a small hub fairing (that has a circular arc upper surface and a flat lower surface) integrated with a nontapered pylon fairing. To minimize drag, the gap between the lower surface of the hub and upper surface of the pylon fairing must be kept to a minimum. Results show that the aerodynamic effects of the fairings on static longitudinal and directional stability can also be important.			
14. SUBJECT TERMS Helicopter drag reduction, Hub and pylon fairings, Fairing effects on static stability		15. NUMBER OF PAGES 94	
		16. PRICE CODE A05	
17. SECURITY CLASSIFICATION OF REPORT Unclassified	18. SECURITY CLASSIFICATION OF THIS PAGE Unclassified	19. SECURITY CLASSIFICATION OF ABSTRACT	20. LIMITATION OF ABSTRACT